EFFECT OF 3D SIMULATED WELDING INDUCED HAZ, RESIDUAL STRESS AND DISTORTION FIELDS ON ULTIMATE STRENGTH OF ALUMINUM STIFFENED PLATES

by

Seyyed Vahid Farajkhah

Submitted in partial fulfilment of the requirements
for the degree of Doctor of Philosophy

at

Dalhousie University
Halifax, Nova Scotia
March 2016

I dedicate this dissertation to my parents, Azam and Reza
who taught me the meaning of unconditional love,
And to my brother, Kian.

Table of Contents

List of Tables

List of Figures

Abstract

A finite element study was conducted to investigate the friction stir welding (FSW) and metal inert gas welding (MIG) induced residual stresses, distortions and heat affected zone (HAZ) and their effects on the behaviour and strength of aluminum ship hull structures. A three-dimensional, two-step thermo-mechanical finite element model was developed to predict the residual stress and distortion fields as well as the heat affected zone for both welding methods. Following the verification of the model, the load vs. shortening curves of stiffened plates of varying geometries were obtained incorporating the welding induced imperfections from both welding methods. The load vs. shortening curves were then used to obtain the moment vs. curvature relationship for a modelled aluminum hull girder. The effect of stiffened plate geometry, and fabrication methods and associated welding induced imperfections on the behaviour, ultimate strength, and failure mode of stiffened plates as well as of the hull girder were presented and discussed.

For the welding induced imperfection study of two aluminum alloy 6061-T6 plates being welded together, results indicated that in comparison with the MIG welding, the FSW process resulted in up to 40% and 60% less tensile residual stresses and HAZ extent and negligible distortions. Increasing the clamping area in FSW process resulted in a decrease in the maximum tensile residual stress by 40%. For the load vs. shortening response study of tee-bar stiffened aluminum plates of various geometries, the result revealed that the presence of the residual stress and HAZ can reduce the ultimate strength of aluminum stiffened plates under the compressive loading by as much as 16.5% and 10%, respectively. The comparison of extruded stiffened plates welded by either FSW or MIG showed that the ultimate strength of the stiffened plates as affected by two welding methods was dependent on the plate slenderness. The higher magnitude of residual stress was shown to be beneficial for the ultimate strength of plates with high plate slenderness. For an ultimate strength study of a modelled hull girder, results showed that the model with extruded elements welded by FSW can have as much as 28% higher ultimate moment capacity than that with non-extruded elements welded by MIG welding. Within the models joined by MIG, the butt welding model resulted in 17% higher moment capacity than the fillet welding model.

List of symbols used

a	Length of plate and stiffened plate
A_E	Cross section area of beam
A_i	Area of the i^{th} element
A_s	Area of the stiffener
$A_{shoulder}$	Area at the interface of the tool shoulder and the workpiece
B	Stefan-Boltzmann constant
b	Width of the model
b_e	Effective width of the plate
b_e'	Tangent effective width of the plate
$b_{x,y,z}$	Body force component
C	Hull girder curvature vector
c	Radius of flux distribution
Cx	X component of hull girder curvature vector
Cy	Component of hull girder curvature vector
E	Young's modulus

f_f	Fractions of the heat front ellipsoid
f_r	Fractions of the heat in rear ellipsoid
g_f	Power density in the front ellipsoid
g_r	Power density in the rear ellipsoid
I	Welding current
I_{ce}'	Equivalent moment of inertia
k_n	Thermal conductivity normal to the surface (W/mC)
$k_{x,y,z}$	Thermal conductivity corresponding to the principal axes x, y, and z.
l	Length of the plate
M_u	Ultimate longitudinal bending strength of the hull girder
N_i	Polynomial interpolation function
P	Normal force
Q	Energy input rate
q	Lateral load
q(x, y, z, t)	Prescribed flux (W/m^2)
Q_b	Heat loss from the bottom surfaces

Q_f	Heat flux due to the tool shoulder and pin
q_s	Heat loss due to convection and radiation
q^t	Rate of heat flow in Cartesian system
$q_{x,y,z}$	Applied surface loads
r	Radius of shoulder
r_{ce}'	Radius of Gyration,
r_e^t	External nodal load
R_{pin}	Radius of the tool pin
$R_{shoulder}$	Radius of the tool shoulder
t	Thickness of the plate
T_0	Ambient temperature for convection and/or radiation (C)
$T_i(t)$	Nodal values of temperature at the time t
U	Strain energy
V	Welding voltage
w_0	Initial deflection at middle of the beam
x_{gi}	Coordinate of the centroid element i from x axis

x_i	Distance of the centroid of the i^{th} element from the x base line
y_{gi}	Coordinate of the centroid element i from y axis
y_i	Distance of the centroid of the i^{th} element from the y base line
α	Heat transfer coefficient for convection (W/ m^2C)
$\alpha_{shoulder}$	Shoulder cone angle
β_0	Plate slenderness
β_b	Convection coefficient between workpiece surface and the backing plate
ε	Emissivity
ε_0	Yield strain
ε_i	Strain at center of the i^{th} element
η	Heat source efficiency
θ	Angle between the neutral axis and X axis
λ	Column slenderness
μ	Coefficient of friction
σ_0	Yield stress
$\sigma_{0.2}$	Proof stress

σ_a	Average stress at failure
$\sigma_{Average}$	Average compressive stress
σ_{buckle}	Buckling strain
σ_E	Euler buckling stress,
σ_e	Instantaneous edge stress
$\sigma_{Elastic}$	Elastic buckling stress
σ_u	Ultimate strength of stiffened plate
σ_Y	Yield stress of the aluminum
$\tau_{contact}$	Shear stress in the surface of the contact
υ	Elastic Poisson's
φ	Deviation of the element from perfectly plastic behaviour
$\Phi(\varepsilon_i)$	Non-dimensional strength of the i^{th} element at a strain of ε_i
$\Phi_{ab}(\varepsilon)$	Average stress of a column
Φ_{jo}	Stress for every strain
ω	Angular velocity
Ω	Problem domain

Acknowledgements

Sincere thanks to my supervisor, Dr. Yi Liu, who provided valuable guidance throughout the course of this research. This thesis would not have been possible without her guidance and kind advice.

I wish to extend my appreciation to my committee members, Dr. Neil Pegg and Dr. Dmitry Garagash for their helpful technical comments on my thesis.

I would also like to thank Dr. Liam Gannon for sharing his expertise and for his technical input in this work.

The financial support of the Natural Sciences and Engineering Council of Canada (NSERC) is gratefully acknowledged.

Chapter 1 - **Introduction**

1.1 Background

Aluminum has been used to build marine vessels since the middle of the 20th century with an increasing application in high-speed vessels in the last 20 years (Muckle, 1963). Collette (2005) estimated that there are 1700 high-speed ferries all around the world and most of them are of aluminum construction. The most important characteristic of aluminum alloys is their high strength-to-weight ratio in comparison to steel and other metals. The lighter weight of aluminum helps to reduce the power requirement and increase the achievable speed and the cargo capacity of vessels. In addition to the advantage of lighter weight, aluminum has an excellent corrosion resistance and therefore it requires low maintenance. Meanwhile aluminum high speed vessels can suffer from fatigue cracking problems as well as poor structural performance in the case of fire.

Ship hull girders are typically made up from steel or aluminum stiffened panels designed to resist axial compressive loads (Aalberg et al., 2001). Analytical and experimental research showed that initial imperfections due to welding such as distortions, residual stresses, and strength reduction in heat affected zones have substantial effects on the ultimate strength of aluminum stiffened panels, hence consideration of these factors is important in the design process. Determination of the exact values of residual stress in stiffened panels requires costly experiments. For this reason an idealized residual stress distribution is often assumed in design process of hull girder stiffened panels. While some research has been conducted in studying the effect of welding induced residual stress and

distortion on the steel stiffened panels, the literature survey yields limited technical information on the effect of these factors on the ultimate strength of aluminum stiffened plates.

Due to a lack of research conducted in the welding induced residual stress and distortion in aluminum stiffened panels, most of the existing design guidelines for aluminum plates and stiffened panels, to a large extent, are based on the research results on steel structures. Considering the fact that the behaviour and the material properties of aluminum alloys are different from steel, such approaches can be questionable. There are several material parameters that make the behaviour of aluminum structures different from steel structures. The ultimate stress of aluminum alloy is about 60% of steel and the elastic modulus of aluminum alloys is about 1/3 of steel. Hence aluminum structures are more susceptible to elastic buckling in comparison to a steel structure with same geometry. Hence, any strength method developed for steel that does not explicitly consider elastic modulus of the material, such as b/t ratios for plating, is not appropriate for aluminum. Also aluminum has a wide variety of alloys with different tempers that can have a wide range of stress vs. strain behaviour. Among the different series of aluminum alloys, 5xxx and 6xxx series are extensively used in marine structures and ship building industry. Series 5xxx gain their strength via strain hardening whereas 6xxx series are mostly strengthened via heat treatment. Both 5xxx and 6xxx series alloys can be extruded into complex shapes. Another factor that affects the behaviour of aluminum alloys is the effect of material softening in the heat affected zone (HAZ) due to welding. Unlike steel structures that the material yield stress does not change significantly in HAZ, the yield strength of aluminum alloys can be reduced by 30% to 50% in the heat affected zone and this can have a great

effect on the ultimate strength of aluminum stiffened panels. The magnitude and distribution of welding induced residual stresses, distortions, and the heat affected zone strength reduction depended on various factors such as geometry, material properties and welding procedure. Although the welding induced residual stresses, distortions and HAZ can be measured experimentally using x-ray diffraction, neutron diffraction and method of sectioning, these methods are time consuming and expensive and the accuracy of the results is subjected to the precision of the devices (Gannon, 2011). In light of this, the finite element modeling has been used as an effective alternative for predicting the welding induced residual stress, distortion and HAZ.

There are methods by IACS (2009) and Gordo and Guedos Soares (1993) which can be used to determine the ultimate strength taking into account the welding induced residual stresses for steel stiffened plates (Gannon, 2011). However, whether they can be directly applied for aluminum stiffened plates remains a question due to the presence of HAZ. The current marine classification society rules, the DNV Rules for Classification of High Speed, Light Craft and Naval Surface Craft (2013) and the ABS Guide for Building and Classing High Speed Naval Craft (2007) apply an overall strength reduction to the yield stresses in the structure to account for HAZ and thus ignore the effect of HAZ on the buckling mode of the structure. While this makes design simpler, the penalty is presumably a heavier and more conservative structure. The Ship Structure Committee (2011) suggested that the strength penalty for modeling the stiffened panel as all-HAZ material in place of a combined base/HAZ material model ranged from 10% to 30%. It recommended that modeling aluminum stiffened panels should explicitly consider the HAZ extent, location,

and strength in place of applying a uniform reduction factor to the strength of the HAZ material.

1.2 Friction stir welding

Friction stir welding (FSW) is a recently emerged solid-state joining technology invented by The Welding Institute (Thomas et al., 1991). It is primarily used on aluminium, and most often on extruded aluminum. The process is illustrated in Figure 1.1. Typically in FSW process the workpiece is clamped to a back-plate to prevent the lateral movement during the welding process, and a cylindrical tool with a pin rotating with a speed of several hundred rpm is slowly plunged into the conjunction of the two workpieces that are to be jointed together. As the tool is plunged into the workpiece the heat is generated by the friction between the surfaces of the rotational welding tool including the shoulder and pin, and the workpieces, which cause the weld material to soften at a temperature less than the melting point of the material. As the FSW progresses along the contact line of workpieces, the plasticized material is stirred by the tool and forces to flow to the side and back of the tool. The stirred material forges to the other materials in the vicinity resulting in a solid phase joint between the two workpieces. Typically the pin may have a diameter about one third of the tool shoulder and its length may be slightly less than the workpiece thickness.

One of the key factors in FSW is the heat generated during the process. The generated heat must be high enough to make the materials around the pin soften for stirring action but low enough so that the material does not reach the melting temperature. As melting of the material does not happen during this process, the FSW yields fine microstructure with absence of cracking and solidification defects (Zhu and Chao, 2004),

and inherently produces a weld with less welding induced imperfections and hence results in a high quality joint with potentially better structural and fatigue performance.

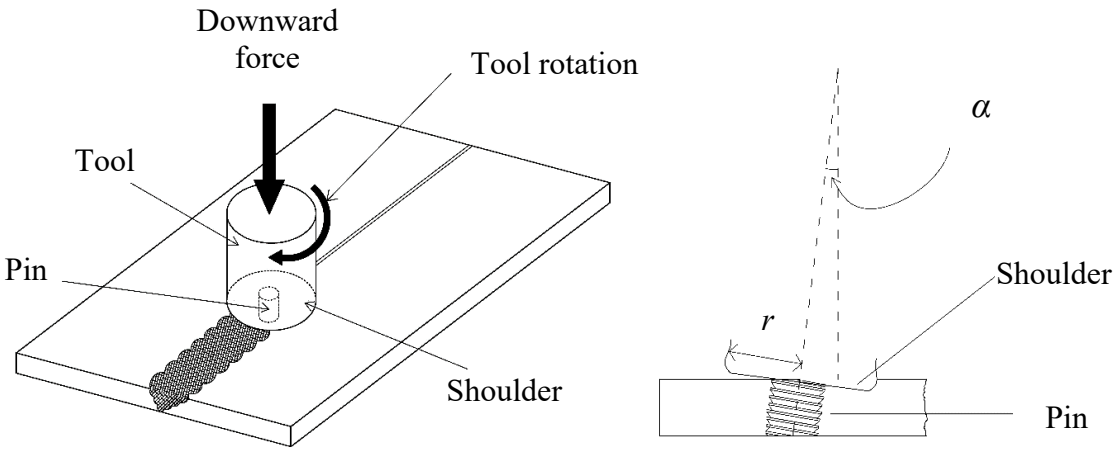

Figure 1.1 FSW process

1.3 Context of this study

This study is a part of an ongoing research in the Department of Civil and Resource Engineering of Dalhousie University on the effects of welding on the behaviour of ship structures. Gannon (2011) studied the effects of longitudinal MIG welding on steel stiffened plates typical to ship structures. His research included:

- Effect of MIG welding sequence on residual stress and distortion in flat-bar stiffened plates.
- Effect of 3D MIG welding-induced residual stress and distortion fields on strength and behaviour of flat-bar, angle-bar and tee-bar stiffened plates.

- Shakedown of MIG welding-induced residual stress and effect on stiffened plate strength and behaviour
- Effect of MIG welding-induced residual stress and distortion on hull girder ultimate strength

This study extends the aforementioned research with the focuses on investigations of the specific effect of welding induced imperfections on the ultimate strength of aluminum hull girders.

1.4 Objectives and Scope

The main objective of this research is to accurately characterize the effects of FSW and MIG welding induced residual stresses and distortions, and heat affected zone on the behaviour and strength of aluminum stiffened panels, and to determine effect of using different welding and fabrication methods on the ultimate strength and performance of ship hull girders.

A detailed description of methodology is as follows:

1. Finite element modeling of welding:
    a. Extending the previous work on thermo-elastic-plastic finite element model simulation of MIG welding on steel stiffened plates (Gannon, 2011) to aluminum stiffened plates incorporating the unique material characteristics of aluminum.

b. Develop a finite element model to simulate the friction stir welding process.

c. Use the created finite element models to generate residual stresses, distortions, and yield strength reduction of HAZ in aluminum stiffened plates typical to naval and commercial ships.

2. Verification of the models

   The models for both MIG and FSW welding are to be verified using experimental results in aluminum plates.

3. Parametric study

   a. Investigate the effects of MIG welding and FSW on the development of the heat affected zone, residual stress and distortion fields in aluminum plates.

   b. Generate load-shortening curves for aluminum stiffened plates with various stiffener and plate geometry to investigate the effect of MIG welding on the behaviour and strength of aluminum stiffened plates.

   c. Study the effect of clamping area and welding speed on the FSW induced residual stresses.

   d. Finite element study on the ultimate strength of extruded aluminum stiffened plates joined by either friction stir welding or metal inert gas welding.

   e. Investigate the effect of fabrication methods on the ultimate strength of aluminum hull girder.

The dissertation is organized following the "paper format" specified in the thesis guidelines provided by the Faculty of Graduate Studies. Chapter one presents an introduction and background of the research topic; Chapter 2 provides a general literature review relevant to the subject; Chapter 3 describes the finite element modeling technique. Chapters 4 to 8 are presented in the form of five journal papers with each dedicated to one subject listed under the section "Parametric study". Chapter 9 provides a summary and key conclusions stemmed from this research.

Chapter 2 - **Literature review**

2.1 Hull girder general behaviour

The main forces that a ship must be able to resist are those due to longitudinal bending imposed by hogging and sagging. When the amidship is located on the crest of the wave it bends in a way that the hull is concave downward, this is called as hogging, and when the amidship is in the trough of the wave the ship will sag so that the hull is bent concave upward which is called sagging. The Stillwater bending moments and shear forces on the hull girder in longitudinal direction under each of hogging and sagging conditions can be estimated from buoyancy and mass distribution curves. Usually the maximum bending moment occurs in the middle section of the ship and the maximum shear forces are located in a distance equal to a quarter of ship length from the ends of the hull (Tupper, 2004).

The ultimate longitudinal bending strength of a ship hull can be characterized using moment vs. curvature relationship for hull girders. One such curve is shown in Figure 2.1 for a typical ship hull. The point, at which the slope of the moment-curvature curve, dM/dC, becomes zero or changes sign, defines the ultimate longitudinal bending strength, M_u, of the hull. In general, M_u is different in hogging and sagging (Rutherford and Caldwell, 1990).

Line 1 in Figure 2.1 represents the case of hull bending failure through ductile material yielding, and point A corresponds to the initiation of yielding in the outermost fibre at initial yield moment. Line 2 represents a fast fracture of the hull. This might be a

result of insufficient ductility in the hull structure materials. Nowadays this type of fracture is not likely as the modern material and construction specifications are intended to prevent this form of failure by providing enough ductility in the materials.

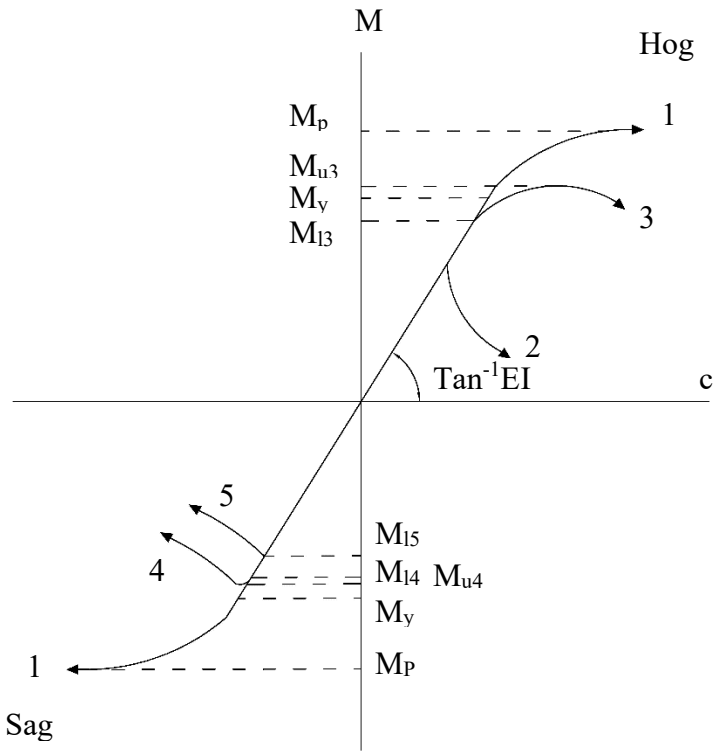

Figure 2.1 Moment-curvature relationship

Lines 3, 4 and 5 in Figure 2.1 display the failure modes in which buckling of compressed elements of cross-section initiates the failure and dominates the ultimate bending strength of the ship hull. Determination of the buckling load and also prediction of the relationship between the compressive load and resulting compressive strain especially in the post buckling regions is in special interest of designers and society rules.

2.2 Historical review of ultimate strength analysis

One of the first methods for computation of the ultimate longitudinal bending strength of hull girders was suggested by Caldwell (1965). In this method, the structural members were divided into panels and the collapse load of each panel was calculated introducing the concept of structural instability strength reduction factor for compression. However the Caldwell's method did not take into account the post collapse strength of the panels which significantly affects the ultimate strength of the ship hull.

The Caldwell's method was further developed by Smith (1977). Smith divided the cross-section of ship hull into a number of beam-columns; each of them consisted of a stiffener, attached to a certain width of plate. The moment-curvature relationship is determined by imposing an incremental curvature to the hull girder. For each curvature applied to the hull girder the average strain of each beam-column element is calculated based on its location relative to the neutral axis. Entering these values in the predefined load-shortening curve of each element, the associated stress state and the load carrying capacity of the element is calculated. Then the bending moment resisted by the cross-section is obtained from the summation of the contribution from the individual elements. By using this method the post-collapse behaviour of the hull girder can be obtained.

Smith's method has inspired the development of several other methods. These methods included the simplified approaches by Billingsley (1980), Adamchak (1984), Dow et al. (1981), Rutherford and Caldwell (1990), Yao and Nikolov (1991, 1992) and Ueda et al. (1982, 1984). The main difference in these methods is the different approaches for derivation of the load-shortening curves of the beam-column elements.

The Idealized Structural Unit method (ISUM) is another type of method which was developed by Ueda et al. (1982). This method is similar to the beam-column method; however instead of simplifying the model using only beam-columns, entire stiffened panels may be replaced by a single element called an idealized structural unit with similar behaviour. Various combinations of different members making up the hull cross-section may be used as idealized structural units. Each idealized structural unit may consist of an individual stiffener, a plate between stiffeners, or a plate with several attached stiffeners. This method is further developed by other researchers such as Ueda et al. (1984), Paik (1993) and Bai et al. (1993).

2.3 Current design practice

Two marine classification society rules, the DNV Rules for Classification of High Speed, Light Craft and Naval Surface Craft (2013) and the ABS Guide for Building and Classing High Speed Naval Craft (ABS 2007) approaches regarding the HAZ in aluminum structures rely on a reduced allowable stress for welded structures. Neither method requires an explicit consideration for the size of the HAZ or location of the HAZ in the structure. These approaches apply a blanket strength reduction to the allowable stresses in the structure to account for HAZ regions, ignoring the effect of HAZ on the buckling mode of the structure. While this makes design simpler and does allow greater freedom for locating structural welds, the penalty is a presumably a heavier and more conservative structure.

Ship Structure Committee *Effect of Welded Properties on Aluminum Structures* (SSC-460, 2011) studied the effect of HAZ using finite element method. They concluded

that there is a significant advantage for modeling aluminum marine stiffened panels by explicitly considering the HAZ extent, location, and strength in place of applying a uniform knock-down factor to the strength of the HAZ material. For the compressive applied forces the strength penalty for modeling the stiffened panel as all-HAZ material in place of a combined base/HAZ material model ranged from roughly 10% to 30%. They proposed that reducing the material strength by 10% appears to be a good "FIRST STEP" for including conventional HAZ in 5xxx series alloy stiffened panels, but they noted that this approach did not appear practical and consistent for the 6xxx series panels. However, the models used in this study just had two slenderness for the stiffener and the plate, also in the modeling the residual stress was ignored and a constant 2 mm initial deflection was assumed regardless of the slenderness. Ship Structure Committee (SSC-460, 2011) also recommended a further investigation of the effect of HAZ on the aluminum stiffened plates in order to develop HAZ-specific strength formulations to remove the penalty approach in marine classification. A study of extrusion design of aluminum stiffened panels was also considered necessary.

2.4 Load-shortening curves

It is noted that since there are no published analytical methods for determination of load-shortening response specific to aluminum alloys, the following presents those proposed for steel stiffened plates.

2.4.1 Rutherford and Caldwell (1990)

Rutherford and Caldwell (1990) checked the validity of the Smith's method for predicting the ultimate strength of steel ship hull girder using a computer programs developed at Lloyd's Register. They considered the plate induced failure mode and the stiffener induced failure mode. The load-shortening curves were obtained and then used to calculate the bending moment and curvature relationship for the ship section using the Smith's method. They correlated the yield strength of the ship material to the yield strength of the hull girder and concluded that a variation of $x\%$ in the yield strength caused a variation of $0.5x\%$ in the ultimate strength of the ship hull. The authors noted that future work is necessary on the prediction of the magnitude and distribution of welded induced residual stresses and their effects on the overall strength. The effect of lateral pressure acting on the bottom and side shells on the ship hull ultimate strength was also investigated. The results indicate that the lateral pressure increases the ultimate strength of ship hull. This can be explained that as the lateral pressure is applied on the plate side it results in a tensile stress in the stiffener flange. This tensile stress delays the stiffener buckling and hence increases the ultimate strength.

2.4.2 Gordo and Guedes Soares (1993)

Gordo and Guedos Soares (1993) proposed a model to predict the load-shortening curves of the steel stiffened panels based on the model proposed by Faulkner et al. (1973) for thin stiffened plates. Faulkner et al. (1973) considered both the stiffener and the effective width of the associated plate as a column that is subjected to an edge stress of σ_e

. In the Faulkner's approach the ratio of the average stress at failure to the yield stress may be calculated by the equation:

$$\frac{\sigma_a}{\sigma_0} = \frac{\sigma_e}{\sigma_0}\left\{\frac{A_s + b_e t}{A_s + b\ t}\right\} \tag{2.1}$$

Where:

σ_a : Average stress at failure

σ_0 : Yield stress

σ_e : Edge stress at failure, equal to $(\varepsilon.E)$

A_s : Area of the stiffener

b : Width of the plate

b_e : Effective width of the plate

t : The thickness of the plate

For the calculation of the effective width of the plate, b_e, Eqn (2.2) by Faulkner (1975) can be used:

$$b_e = b\left(\frac{2}{\beta_0} - \frac{1}{\beta_0^{\,2}}\right) \qquad \text{for} \qquad \beta_0 > 1 \tag{2.2}$$

$$b_e = b \qquad \text{for} \qquad \beta_0 \le 1$$

where β_0 is the slenderness of the plate:

$$\beta_0 = \frac{b}{t}\sqrt{\frac{\sigma_0}{E}} \tag{2.3}$$

In Eqn (2.1) the ratio of the edge stress to the yield stress, $\frac{\sigma_e}{\sigma_0}$, can be calculated by Johnson-Ostenfeld interaction equation:

$$\frac{\sigma_e}{\sigma_0} = 1 - \frac{1}{4}.\frac{\sigma_0}{\sigma_E} \qquad for \quad \sigma_E \geq 0.5\sigma_0 \tag{2.4}$$

$$\frac{\sigma_e}{\sigma_0} = \frac{\sigma_E}{\sigma_0} \qquad for \quad \sigma_E \leq 0.5\sigma_0$$

Where:

σ_E: Euler buckling stress, $\sigma_E = (\frac{\pi r_{ce}'}{l})^2 E$

l: length of the plate

r_{ce}': Radius of Gyration, $r_{ce}' = \sqrt{\frac{I_{ce}'}{A_s + b'_e t}}$

I_{ce}' : Equivalent moment of inertia

And the tangent effective width of the plate b'_e, can be calculated by Faulkner's tangent effective width equation:

$$\frac{b_e'}{b} = \frac{1}{\beta}.\sqrt{\frac{\sigma_0}{\sigma_e}} \tag{2.5}$$

Gordo and Guedes Soares modified and generalized this approach to generate the entire stress-strain curve of stiffened plates. This was done based on the assumption that for any strain, the ratio of $\frac{\sigma_E}{\sigma_0}$, has an instantaneous value. This ratio for the Euler's nominal stress is given by:

$$\Phi_E = \frac{\sigma_E}{\sigma_0} = \left(\frac{\pi}{\lambda}\right)^2 \tag{2.6}$$

where λ is the column slenderness, $\lambda = \left(\frac{l}{r_{ce}}\right)\sqrt{\varepsilon_0}$, and ε_0 is the yield strain. Replacing ε_0 by current strain of ε the Euler stress ratio at a strain of ε becomes:

$$\Phi_E(\bar{\varepsilon}) = \frac{\Phi_E}{\bar{\varepsilon}} \tag{2.7}$$

where $\bar{\varepsilon} = \frac{\varepsilon}{\varepsilon_0}$ .The column slenderness λ varies by the increase of strain due to the changes in the effective width. By assuming that Eqn (2.4) is valid and it can be modified for every strain:

$$\Phi_{jo} = \left(1 - \frac{1}{4.\Phi_E(\bar{\varepsilon})}\right).\frac{\sigma_e}{\sigma_0} \qquad for \quad \Phi_E(\bar{\varepsilon}) \geq 0.5 \tag{2.8}$$

$$\Phi_{jo} = \Phi_E(\bar{\varepsilon}).\frac{\sigma_e}{\sigma_0} \qquad for \quad \Phi_E(\bar{\varepsilon}) \leq 0.5$$

Finally the ratio of the average stress in the stiffened plate to the yield stress can be used to calculate the load-shortening curves including the buckling inelastic effects. This expression might be written as:

$$\Phi_{ab}(\bar{\varepsilon}) = \Phi_{jo}\left\{\frac{\mathrm{A_s} + b_e' t}{\mathrm{A_s} + b\ t}\right\} \tag{2.9}$$

Where $\Phi_{ab}(\bar{\varepsilon})$ is the average stress of a column composed by a stiffener of area $\mathrm{A_s}$ and a plate of area bt under a strain of $\bar{\varepsilon}$. In Eqn (2.9), b_e' is the tangent effective width of the plate given by:

$$b_e' = b\left(\frac{2}{\beta} - \frac{1}{\beta^2}\right) \tag{2.10}$$

Where β is the instantaneous slenderness of the plate for each strain given by:

$$\beta = \frac{b}{t}.\sqrt{\varepsilon} \tag{2.11}$$

2.4.3 Hansen (1996)

Hansen (1996) developed a method to predict the load-shortening curves for steel beam-columns to be used in the Smith's method, taking into account the effects of welding induced initial deflection and residual stresses. Hansen assumed that the failure occurs locally between two adjacent frames and each beam-column element behaves independently. In this method,the stress distribution at the middle of a beam with a cross section area of A_E and length of l subjected to a normal force of P and a lateral load of q

with an end rotation of θ and initial deflection of w_0 at the middle of the beam, is given by:

$$\sigma(z) = -\frac{P}{A_E} - \frac{w_0 E z P \pi^2}{L^2 (P - P_E)} - \frac{Eqz}{P} + \frac{\alpha E z}{\sin \frac{\alpha L}{2}} \left(\frac{w_0 P \pi}{L(P - P_E)} + \frac{Lq}{2P} + \theta \right) \tag{2.12}$$

where z is the distance measured from the neutral axis of the beam and:

$$\alpha = \sqrt{\frac{P}{EI_E}} \tag{2.13}$$

$$P_E = EI_E \left(\frac{\pi}{L} \right) \tag{2.14}$$

where I_E is the effective moment of inertia. By finding the sectional parameter A_E, in every iteration the corresponding displacement can be calculated by:

$$\delta = \frac{PL}{EA_E} \tag{2.15}$$

Eqn (2.12) and (2.15) can be used to calculate the force P as a function of end displacement δ and the rotation θ, to generate the load-shortening curve in the elastic compression region.

2.4.4 Office of Naval Research's (ONR) simplified approach (2011)

Ship Structure Committee (SSC-460, 2011) presented an early version of ONR simplified approach for predicting the buckling strength of aluminum panels. This method

is based on the Hopperstad et al.'s (1999) development of Stowell's (1948) unified buckling theory. Stowell suggested that the uniaxial buckling stress of a plate can be calculated as:

$$\sigma_{Buckle} = \eta \sigma_{Elastic} \tag{2.16}$$

where $\sigma_{Elastic}$ is the elastic buckling stress, and η is the correction factor for the plastic effects of stockier plates. Elastic bucking stress for plates can be calculated from the equation:

$$\sigma_{Elastic} = k \frac{\pi^2 E}{12(1-\nu^2)} \left(\frac{t}{b} \right)^2 \tag{2.17}$$

where E is the Young's modulus, ν is the elastic Poisson's ratio taken as 0.3 for aluminum, t is the thickness of the plate, b is the width, and k is the buckling geometry coefficient which is 4 for plates simply supported on all of four edges.

Hopperstad et al. (1999) extended this method to predict the load-shortening curves of plates in compression including the post buckling region. The effective width approach was used where the effective width of the plate is reduced after buckling to take into account the plate's stiffness reduction. For any instantaneous compressive stress the effective width is given by:

$$b_e = b \frac{\sigma_{avg}}{\sigma_e} \tag{2.18}$$

where $\sigma_{Average}$ is the average compressive stress, and σ_e is the instantaneous edge stress which is the stress in the material stress-strain curve that corresponds to the current axial strain. In the Hopperstad et al.'s method it is assumed that the effective width of the material in post-buckling region is equal to the width of a plate that would first buckle in the same corresponding edge stress. Hence, the stress in the post-buckling region is equal to:

$$\sigma = \sqrt{\eta \sigma_{Elastic} \sigma_e} \leq \sigma_e \tag{2.19}$$

where η is the buckling coefficient calculated at the current edge-stress, and $\sigma_{Elastic}$ is the elastic buckling stress calculated from Eqn (2.17) with the original plate geometry.

2.5 Effect of MIG welding on aluminum plates

One of the earliest studies on the welding of aluminum alloys was conducted by Nelson and Howell in (1952). The composition of the alloy that they used was close to modern 5xxx and 6xxx series. In this study they investigated the strength of butt and fillet welds in aluminum structures as well as the increase in the buckling susceptibility of aluminum structure as a result of welding process.

Hill et al. (1960) extended the work of Nelson and Howell by studying the strength reduction in the welding area of aluminum structures. Based on a large amount of experimental work on different aluminum alloys with both butt and fillet welds, they proposed to model the heat affected zone of welding as a single HAZ block with an

effective width of 37.5mm from the weld centerline. Based on this assumption they developed some formulas for calculating the strength of different aluminum structural members such as beams, columns, and plates.

In early 1980s, Mofflin (1983), and Mofflin and Dwight (1984) studied the collapse strength of a series of 76 aluminum un-stiffened plates under uni-axial compressive loading. The components were made of 5083 and 6082 aluminum alloys that are widely used in ship building industry. In the fabrication of the specimens they used tungsten insert gas (TIG) welding for longitudinal direction and metal inert gas (MIG) welding for transverse direction. Test results revealed that the longitudinal welding resulted in a 10 to 15% reduction in plate strength for both the 5083 and 6082 specimens. The presence of the transverse welding also reduced the plate strength by 30%. They concluded that the difference of some results for 5083 and 6082 alloys are related to the difference in material properties.

Hopperstad et al. (1997) investigated the studies of Mofflin (1983) and Mofflin and Dwight (1984) on un-stiffened aluminum plates using ABAQUS non-linear finite element program. They used shell elements for plates and refined meshing in the heat affected zone (HAZ) area. In the finite element modeling the welding was not modeled directly but in the analysis they assumed the strength reduction of material in the HAZ. They also assumed an idealized residual stress distribution and amplitude in the finite element model. They concluded that the finite element method can be used reliably to predict the behaviour and strength of welded aluminum plates under compressive loading.

Matusiak and Larsen (1998) and Matusiak (1999) performed experimental tests on aluminum 6082-T6 alloy butt and fillet welds with 5183 filler metals. Results revealed that the material in HAZ areas near the welding line has less ductility in comparison with HAZ material far from the welding line. The welding line perpendicular to the applied stress and loading direction can reduce the strength significantly. Matusiak (1999) observed that ignoring the HAZ in fillet welded aluminum 6082-T6 joints can considerably overestimate its tensile strength.

Kristensen and Moan (1999) studied the effect of HAZ in the ultimate strength of rectangular aluminum plates using finite element program ABAQUS. Specimens were made of 5xxx and 6xxx series aluminum alloys. The welding was not modeled in the numerical analysis and the initial imperfection in a sinusoidal form was assumed. The extent of the HAZ was assumed for the models and an idealized residual stresses equal to 75% of the yield stress was considered for the plates in the HAZ. They found that the presence of HAZ resulted in reductions of 10% to 35% in the ultimate strength of 5xxx series and 6xxx series aluminum plates under axial compressive loading.

Kristensen (2001) carried out a parametric study on the collapse strength of aluminum plates using non-linear finite element code ABAQUS. Again, the welding was not directly modeled, but the residual stresses and initial deflections were assumed. In this study Kristensen investigated the effects of a wide range of parameters, such as assumed sizes of HAZ, plate aspect ratio, and material properties as well as the assumed values for residual stresses and initial deflections on the ultimate strength of 5xxx and 6xxx series aluminum plates. Results revealed that the impact of HAZ on the ultimate strength of aluminum plates do not vary significantly for the relative slenderness of the plates. There

is a linear relation between the yield stress reduction in HAZ and plate strength, as well as HAZ width and plate strength.

Aalberg et al. (2001) tested a series of extruded 6082-T6 aluminum profiles with longitudinal welds. The section types were open L-shaped section stiffeners and closed section (box) stiffeners. The tested specimens failed in different modes such as overall flexural buckling, flexural buckling combined with local plate buckling, and stiffener tripping. Test results revealed that the post buckling levels of the load-shortening curves are strongly dependent on the failure mode of the stiffened plate. Among the buckling failure modes, stiffener tripping is the least desirable due to its abrupt reduction in resistance beyond the ultimate load. The effects of welding induced imperfections were not studied in this study.

One of the major research on aluminum stiffened panels was carried out by Zha and Moan (2001, 2003). They tested the ultimate strength of aluminum stiffened plates of various geometric configurations with predominately torsional failure modes. Various heights of stiffener and plate thickness were studied. They also analyzed the specimens using non-linear finite element code ABAQUS. Models were made of AA5083-H116 and AA6082-T6 aluminum alloys. For modeling of stiffened panels, shell elements were used and one element was selected over the HAZ region. However, the welding process and weld elements were not modeled in the finite element study. The welding induced tensile residual stress was assumed equal to the reduced yield stress of the material in HAZ in a direction parallel to the weld line with a width equal to the width of HAZ. For each model two widths of 12.5 and 25 mm were assumed for the HAZ. The initial deflections measured in the experiments were applied to the finite element models. The results revealed that the

reduction in the ultimate strength of the specimens is affected by the presence of HAZ and the amount of the reduction is related to the height of the stiffener. The HAZ in the transverse direction was shown to have the dominant reduction effect on the ultimate strength of the stiffened panels due to the localization of plastic deformation in this region. Results of finite element analysis showed that due to the presence of residual stresses the ultimate strength of the panels was reduced by 1% to 7% for specimen made of 5083-H116 and by less than 3% for specimens made of 6082-T6.

Rigo et al. (2003) studied a range of parameters on the ultimate strength of axially compressed aluminum stiffened panels, including extruded profiles. The material used was aluminum AA6082-T6. The welding process and weld element were not directly modeled in the numerical studies. The welding induced initial deflection of the model was assumed to be 2 mm at the middle of the specimen and the residual stress was assumed to be same as the assumptions of Zha & Moan (2001). The parameters included the location of welding, HAZ extents, initial distortions, plate thickness, residual stresses, and yield stress of HAZ. They found that HAZ has no significant effect on slender panels with low ultimate strength, but as the plate becomes stockier the sensitivity of the ultimate strength to HAZ becomes more important. Results also showed that the ultimate strength of aluminum stiffened panels with extruded elements are less sensitive to HAZ. The effect of HAZ width (12.5 mm, 25 mm, 50 mm, 75 mm, and 100 mm HAZ widths) on the ultimate strength was not proportional to the HAZ width. For example, the reduction induced by first 25mm was twice the additional reduction induced by another 25mm. In the analysis, the strength reduction induced by the assumed residual stresses was 2.5% for a 5mm thick plate. Results

indicated that the thicker the plate, the more sensitive to the residual stresses the specimen became.

Paik and Duran (2004) studied the ultimate strength of AA5383 aluminum plates and stiffened panels under axial compressive loading using the non-linear finite element code ANSYS. The width of HAZ was assumed three times of the thickness of the plate for un-stiffened plates, and for the stiffened plates the width of the HAZ was taken from the popular "1-in" rule that considers the width of the base material softening 1 inch/25mm in all directions from the centerline of the weld (Mazzolani, 1995). The welding process was not modeled in the finite element study. An average level of initial deflections were assumed for both of the plates and stiffeners based on the data obtained from fabrication-related initial imperfections for steel structures (Paik and Thayamballi, 2003) and some measured data for aluminum structures (Zha and Moan 2001, Matsuoka et al. 1998). The influence of residual stresses was neglected in the finite element modeling. They analyzed 23 different plates and 50 different stiffened panels and derived formulas for the ultimate strength of aluminum plates and stiffened panels through the regression analysis of the computed results.

Paik et al. (2007) studied the collapse characteristics of aluminum stiffened plates by experimental testing and numerical study using the finite element code ANSYS. A total of 78 full-scale prototype aluminum structures were constructed by MIG welding and 6 types of welding induced initial imperfections were identified. They categorized the six types of the imperfection in three levels of "slight", "average", and "severe". Buckling collapse tests were conducted on the specimens and the axial load-displacement curves were obtained until and after the ultimate strength was reached. The FE model they used

had one shell element representing the HAZ in the plate and stiffener. The width of the HAZ was assumed based on an average level of HAZ from statistical analysis of the experimental data. The welding was not directly modeled in the finite element analysis but simplified average level of residual stresses and distortions were considered in the modeling. It was observed that models with higher ratio of stiffener height-to-thickness mostly collapsed by lateral torsional buckling or tripping, and the models with lower height of stiffener tended to have a beam-column type collapse. They proposed closed-form empirical ultimate limit state formulas for aluminum stiffened plate structures.

Ship Structure Committee (SSC 460, 2011) conducted a series of non-linear finite element analysis for tee-bar stiffened panels. Shell elements were used for modeling and welding process and weld elements were not modeled. Residual stresses were neglected in the modeling. The width of the HAZ was assumed to be 3 times of the plate thickness or stiffener thickness and both of the longitudinal and transverse HAZ were assumed. The yield strength of the materials was assumed to be either all HAZ or all base metal. The finite element results were compared with an early version of ONR strength method. Results revealed that modeling aluminum structures as all-HAZ material is overly conservative and will result in a substantial weight penalty.

2.6 Effect of FSW process on aluminum plates

Murphy et al. (2007) used finite element modeling to study the effect of FSW induced residual stress and HAZ on the ultimate strength and buckling performance of multi-stiffened integrally stiffened panel (ISP), that are used in aircraft wings, where L-

shaped stiffeners were joined to the plates (skin) by FSW. Shell elements were used in the finite element modeling and the FSW process was not simulated, however, different values for FSW induced residual stress, HAZ and distortions were assumed in the modeling. The distortion were assumed to be mainly a result of the production process of the skin. In the welded interface of the skin and stiffener rigid link elements were used and in the un-welded interfaces gap elements were used. The parametric finite element study revealed that the initial skin buckling is predominately affected by the magnitude of the FSW induced residual stress and HAZ while the ultimate collapse response of the considered structures were less sensitive to the welding induced residual stress and HAZ.

Yoon et al. (2009) studied the buckling collapse of ISP structures welded by FSW using finite element analysis. They chose two different sectional shapes of 400 and 600 kN for the models using the tools provided by Airbus. The FSW welding process was not simulated. The effect of FSW on the structure was considered in the finite element modeling just by assuming HAZ in the assumed weld lines. Shell elements were used in the modeling and a 30 mm HAZ width was considered in the weld lines based on the previous experimental results. Meanwhile no FSW induced residual stress or distortions were considered in the modeling. The models ran a second time without the HAZ. The results revealed that FSW induced HAZ can reduce the ultimate strength of the ISP structures by as much as 10%.

Caseiro et al. (2013) used finite element modeling to study the buckling and to develop optimization algorithms for extruded aluminum stiffened plates, made of AA2024-T351, under compressive loads using 3D elements. Two kinds of stiffened plates were considered including built-up profile and completely extruded tee-bar stiffened

plates. Though the welding was not simulated but for representing the FSW in the models, a width for the HAZ was assumed and the material properties of the areas that were considered as the weld line was reduced. No FSW induced residual stress and distortions were assumed. The models were analyzed with and without the FSW induced HAZ. They developed algorithms to determine the optimized dimensions for the stiffened plates taking into the account the effect of the FSW (presence of the HAZ).

Paulo et al. (2014) studied the buckling behaviour of aluminum plates joined by FSW. For measuring the residual stress, a contour method was used. However the obtained residual stress was not reasonable as the compressive residual stresses of as high as 200 MPa were presented around the weld line. In the finite element modeling shell elements were used. The width of the HAZ was assumed based on the other studies. To study the effect of distortions, three different distortion magnitudes were considered. The results revealed that residual stress can decrease the ultimate strength of the plates. The percentage of the reduction was related on the plate length and the assumed distortions. The percentage of the reduction increased by the increase of the magnitude of the distortion. However it was shown that in the plates with a length greater than 300 mm the magnitude of the ultimate strength was almost the same for the different assumed magnitudes of distortions.

2.7 Summary of the literature review

Although the effect of HAZ and residual stress and distortion fields on the strength of aluminum stiffened plates has been studied in the past, it needs to be pointed out that these studies are, in general, very limited and assumptions and idealizations made in these

studies varied, which may have led to some conflicting or inconclusive information reported in these studies.

For simplicity, the main general conclusions are listed below in point form. A detailed literature review can be found in the proposal.

1. To the best knowledge of the author there is no reported study on the structural performance of aluminum structures typical to the ship building fabricated using friction stir welding. Among the few researches that studied the structural performance of structures fabricated by FSW, idealizations and assumptions were used in the modeling instead of actual simulation of the welding and in most cases the presence of the residual stress was ignored.

2. There is no reliable method for determining the load-shortening curves of aluminum stiffened plates. Design codes underestimate the strength of the aluminum stiffened plates (Aalberg et al, 2001). Approaches regarding the HAZ in aluminum structures rely on a reduced allowable yield stress for welded structures. The penalty is presumably a heavier and more conservative structure (SSC-460, 2011). Ship Structure Committee SSC-460 (2011) indicates that "Investigation of the effect of HAZ on the aluminum stiffened plates in order to develop HAZ-specific strength formulations to remove the penalty approach in marine classification is necessary."

3. The HAZ due to MIG welds can reduce the ultimate strength significantly, but different studies indicated different degrees of reduction ranging from 0 to 35%. One study (Rigo et al. 2003) showed that HAZ has no significant effect on

slender models, and as the panels become stockier the effect of HAZ on ultimate strength increases. However, another study (Kristensen 2001) noted that the strength reduction due to HAZ is constant regardless of plate slenderness.

4. For different stiffener configurations and slenderness, the effect of HAZ on the ultimate strength reduction might be different. Numerical analysis by Zha and Moan (2001) showed that the reduction of the ultimate strength of flat-bar aluminum stiffened plates, designed to fail by torsional buckling of stiffeners, due to HAZ for AA6082-T6 and AA5083-H116 on the average, was about 15% and 10% respectively while the results of Rigo et al. (2003) for angle-bar stiffened plates shows a 0% to 30% reduction depending on the slenderness of the stiffened plate.

5. The effect of HAZ on the angle-bar aluminum stiffened plates with a λ typical of naval structures and with transverse welds in the location of transverse frames are inconclusive in the Rigo et al. (2004) study. Also the effect of transverse and longitudinal HAZ on the flat-bar aluminum stiffened plates with geometry and buckling modes other than torsional buckling of stiffeners are inconclusive in the Zha and Moan (2001) study.

6. The literature review concluded that the effect of residual stress on the ultimate strength reduction is much less than the effect of HAZ, even Ship Structure Committee SSC-460 (2011) ignored the presence of the residual stress. However, there is uncertainties on the magnitude of the reduction caused by

residual stress. This could also resulted from the limited slenderness of the studied models or different assumptions and idealizations made with regard to the magnitude and distribution of residual stresses, distortions, and HAZ.

7. None of the previous studies modeled the welding process. In some studies, the effects of welding are taken into account by assuming idealized distribution and amplitude of welding induced residual stresses, distortion and HAZ while other studies ignored the presence of residual stresses in the finite element modeling.

8. The effect of using extruded aluminum stiffened plates instead of non-extruded aluminum stiffened plates and also the effect of using FSW or MIG welding on the structural performance of aluminum stiffened plates have not been studied.

9. The effect of MIG welding induced residual stress and HAZ on the ultimate strength of aluminum ships are unclear.

10. The effect of using extruded elements instead of non-extruded elements on the ultimate strength of aluminum hull girders has not been studied.

11. The effect of using FSW instead of traditional MIG welding on the ultimate strength of aluminum hull girders is unclear.

Chapter 3 - **Welding simulation by the finite element method**

3.1 Fundamentals

A two-step nonlinear finite element analysis can be used for the modeling of welding. In the first step of this process, the time-dependant temperature distribution is determined in a transient thermal analysis. For the heat transfer analysis, we assume that the material obeys Fourier's law of heat conduction. The rate of heat flow in a Cartesian system can be written as:

$$q^T = \left[q_x, q_y, q_z\right] \tag{3.1}$$

Where q_x, q_y and q_z are the rate of heat flows conducted per unit area. And:

$$\begin{aligned} q_x &= -k_x \frac{\partial \theta}{\partial x} \\ q_y &= -k_y \frac{\partial \theta}{\partial y} \\ q_z &= -k_z \frac{\partial \theta}{\partial z} \end{aligned} \tag{3.2}$$

where θ is the body temperature, and k_x, k_y and k_z are the thermal conductivity corresponding to the principal.

If the rate of heat generation or rate of the heat source per unit volume at every point in the domain Ω is assumed to be Q, the heat flow equilibrium for a steady state condition becomes:

$$\frac{\partial q_x}{\partial x}+\frac{\partial q_y}{\partial y}+\frac{\partial q_z}{\partial z}=-Q \tag{3.3}$$

Using the gradient operator:

$$\nabla=\begin{pmatrix}\frac{\partial}{\partial x}\\ \frac{\partial}{\partial y}\\ \frac{\partial}{\partial z}\end{pmatrix} \tag{3.4}$$

And,

$$q=\begin{cases}q_x\\ q_y=-k\begin{cases}\frac{\partial\theta}{\partial x}\\ \frac{\partial\theta}{\partial y}\\ \frac{\partial\theta}{\partial z}\end{cases}=-k\nabla\theta\\ q_z\end{cases} \tag{3.5}$$

The Eqn (3.3) can be written as:

$$\nabla^{\theta}q+Q=0 \tag{3.6}$$

By substituting Eqn (3.4) and (3.5), Eqn (3.6) can be written as:

$$\frac{\partial}{\partial x}(k_x \frac{\partial \theta}{\partial x}) + \frac{\partial}{\partial y}(k_y \frac{\partial \theta}{\partial y}) + \frac{\partial}{\partial z}(k_z \frac{\partial \theta}{\partial z}) = -Q \tag{3.7}$$

In the case of welding process thermal simulation, which the temperature distribution changes with time, an additional term must be added to the right side of the equation:

$$\frac{\partial}{\partial x}(k_x \frac{\partial \theta}{\partial x}) + \frac{\partial}{\partial y}(k_y \frac{\partial \theta}{\partial y}) + \frac{\partial}{\partial z}(k_z \frac{\partial \theta}{\partial z}) + Q = c \frac{\partial T}{\partial t} \tag{3.8}$$

where c is the volumetric specific heat (J/m^3C)

Eqn (3.8) is nonlinear if any of c or k is a function of T, and either of the essential or natural boundary conditions must be satisfied on the boundary of Ω. Goldak et al. (1984) defined the essential boundary conditions as:

$$k_n \frac{\partial T}{\partial n} + q + \alpha(T - T_0) + \sigma\varepsilon(T^4 - T_0^4) = 0 \tag{3.9}$$

where:

k_n = thermal conductivity normal to the surface (W/mC)

q(x, y, z, t) = prescribed flux (W/m^2)

α = heat transfer coefficient for convection (W/ m^2C)

ε = emissivity

T_0 = the ambient temperature for convection and/or radiation (C)

If radiation is included or if the convective heat transfer coefficient is temperature dependant, this boundary condition is nonlinear.

The initial conditions can be specified for (x, y, z) in the domain of **Ω** as:

$$T(x,y,z) = T_0(x,y,z) \tag{3.10}$$

If the partial differential of Eqn (3.8), the initial boundary conditions, and the natural boundary conditions are consistent, the problem is considered to be well posed and there is a unique solution for the problem.

The finite element method for solving Eqn (3.8) is based on a piece-wise polynomial approximation for the temperature field within each element:

$$T(x,y,z) = \sum_{i=1}^{nodes} N_i(x,y,z) T_i(t) \tag{3.11}$$

Where $T_i(t)$ are the nodal values of temperature at the time t, and N_i are the polynomial interpolation function depending on the type of element, its size, and its shape. The temperature gradient can be calculated at any point from Eqn (3.11):

$$\left[\frac{\partial T}{\partial x}, \frac{\partial T}{\partial y}, \frac{\partial T}{\partial z}\right] = \left[\frac{\partial N_i}{\partial x} T_i, \frac{\partial N_i}{\partial y} T_i, \frac{\partial N_i}{\partial z} T_i\right] \tag{3.12}$$

In order to evaluate T_i, Galerkin method can be used. Galerkin method requires:

$$\int_{\Omega} \varepsilon N_i d\Omega = 0 \tag{3.13}$$

Where N_i in Eqn (3.13) is a test function and N_i in Eqn (3.11) are the trial functions. Because of the fact that Eqn (3.11) is an approximate to the exact solution, there are some residual or error terms. If there would be no residual or error terms, Eqn (3.11) is the exact solution. Since there are i nodes, Eqn (3.13) results in a set of i ordinary differential equation which are integrated to form a set of nonlinear algebraic equations:

$$[K][T] = [R] \tag{3.14}$$

where $[K]$ is an effective thermal activity of stiffness matrix, $[R]$ is an effective load vector, and $[T]$ is the vector of nodal temperature.

3.2 Heat source modeling in MIG welding

Accurate modeling of heat source is a complicated task, and the choice of how to model it in finite element is depended on the purpose of study. If the aim of study is to accurately model the heat affected zone (HAZ) and fusion zone (FZ), a detailed model of heat source and a fine finite element meshing in the vicinity of the heat source must be used, which consequently limits the size of the model that can be solved in a practical amount of time. When the objective of the analysis is to predict the residual stresses and deformations of the larger surrounding area, the modeling of the heat source can be

simplified to allowing for a courser mesh and reduced time of analysis. In larger models, it is usually not necessary to predict the size and shape of the FZ. These parameters may be estimated to simplify the heat source model.

The basic theory of heat flow was first developed by Fourier and then Rosenthal (1946) developed it for moving point, line, or plane sources of heat. Although Rosenthal's model is still the most popular method for calculating the thermal history of welds, many researchers have shown that it is subjected to serious errors for temperatures near the fusion and heat affected zones. These errors are mostly due to the basic assumptions of the method where the temperature is assumed infinite in the heat source and the material properties are assumed to be temperature independent. A detailed discussion on the accuracy of Rosenthal analysis is presented by Myres et al. (1967).

Paley and Hibbert (1969) and Westby (1968) used a constant power density distribution in the fusion zone (FZ) to distribute the heat throughout the molten zone to reflect the digging action of the arc more accurately. Pavelic et al. (1969) proposed a Gaussian distribution of flux (W/m^2) deposited on the surface of the workpiece. In Pavelic et al.'s disc model, the thermal flux has a Gaussian or normal distribution in the z-z plane as shown in Figure 3.1. This disc model is more realistic than the point source as it is able to distribute the heat over a source area. Krutz and Segerlind (1978) and Friedman (1975) combined the Pavelic's disc model with FEM analysis in order to achieve a better temperature distribution in the fusion and heat affected zones. Their developed alternative form is expressed in a coordinate system that moves with the heat source. The power distribution in this model is:

$$q(x,\xi) = \frac{3Q}{\pi c^2} e^{-3x^2/c^2} . e^{-3\xi^2/c^2} \tag{3.15}$$

where Q is the energy input rate (W) and C is the characteristic radius of flux distribution (m).

Goldak et al. (1984) proposed a double ellipsoid non-axisymmetric three dimensional heat source model which is more realistic and more flexible in comparison with other models. The double ellipsoids of this model represent the volumetric heat from the molten metal droplets and a Gaussian power density to represent the heat of the welding torch. The combination of two ellipsoidal sources makes it possible to simulate the different steps of temperature gradient around the heat source as shown in Figure 3.2.

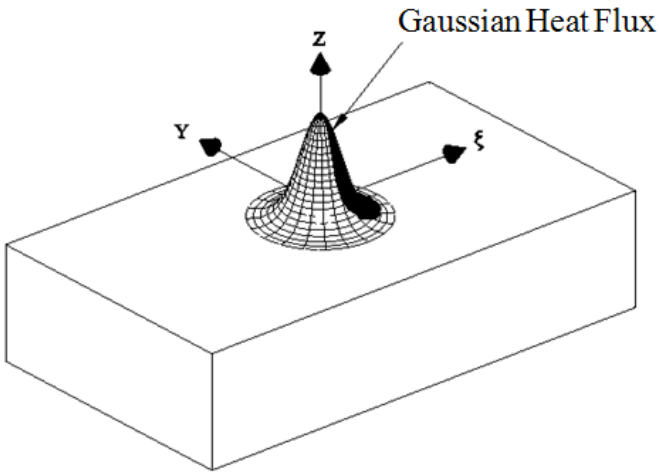

Figure 3.1 Pavelic heat disc source. (Anderson, 2000)

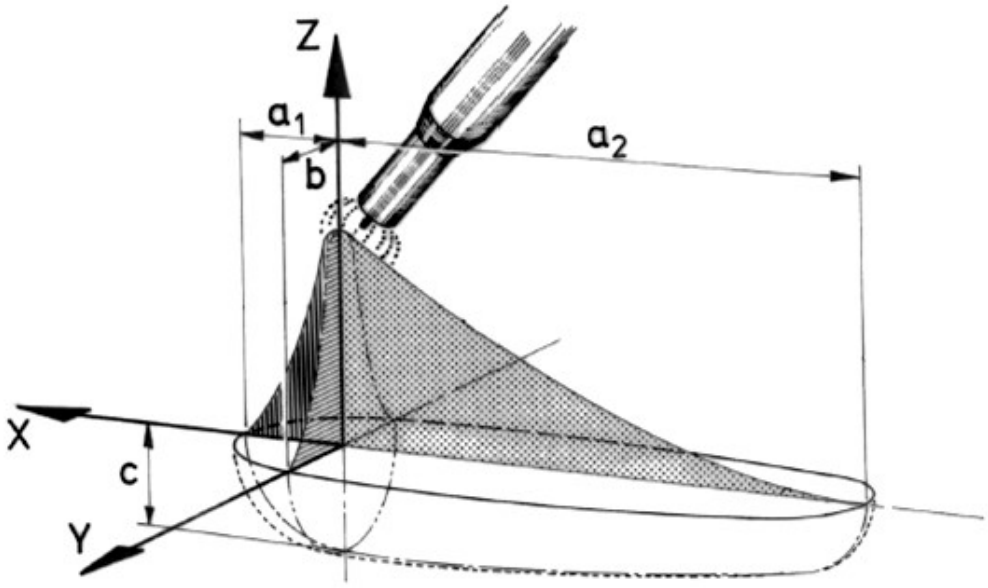

Figure 3.2 Double ellipsoidal power density distribution (Anderson, 2000)

The front half of the source is the quadrant of one ellipsoidal source, and the rear half is the quadrant of another ellipsoidal. The power density distribution in the front and the rear ellipsoids as given by Anderson (2000) are presented as follows:

$$q_f(x,y,z,t) = \frac{6\sqrt{3} f_f Q}{a_1 bc\pi\sqrt{\pi}} e^{-3y^2/b^2} e^{-3z^2/b^2} e^{-3[x+v(\tau-t)]^2/a_1^2} \tag{3.16}$$

$$q_r(x,y,z,t) = \frac{6\sqrt{3} f_f Q}{a_2 bc\pi\sqrt{\pi}} e^{-3y^2/b^2} e^{-3z^2/b^2} e^{-3[x+v(\tau-t)]^2/a_2^2} \tag{3.17}$$

$$f_f + f_r = 2 \tag{3.18}$$

$$Q = \eta VI \tag{3.19}$$

where:

f_f, f_r: Fractions of the heat in rear and front ellipsoids

g_f, g_r : Power density in the front and the rear ellipsoids

v, t, τ : Welding speed, time, and heat source x-position at t = 0

Q : Effective energy input

η, V, I : Heat source efficiency, welding voltage, welding current

3.3 Heat source modeling in FSW welding

The key component of friction stir welding simulation is the modeling of heat generation. In this study, the thermal boundary value problem for of the FSW is schematically shown in Figure 3.3. The energy balance at any time during the FSW requires (Chao et al., 2003):

$$Q_f = q_s + Q_b + Q \tag{3.20}$$

where Q_f is the heat flux due to the tool shoulder and pin interface friction with the workpiece, q_s is heat loss due to convection and radiation between the free surfaces and air, Q_b is the heat loss from the bottom surfaces of the workpiece due to the heat conduction to the backing plate, and Q is the increase of the heat content in the workpiece (W). Because of the term Q, the heat transfer process in the workpiece is not steady state. However, Q_f is expected to be constant except in the beginning and the end of the FSW process due to fact

that it is only function of physical interact between the tool pin/shoulder and the workpiece. Hence in this study a moving heat source with a constant Q_f is developed for the finite element simulation.

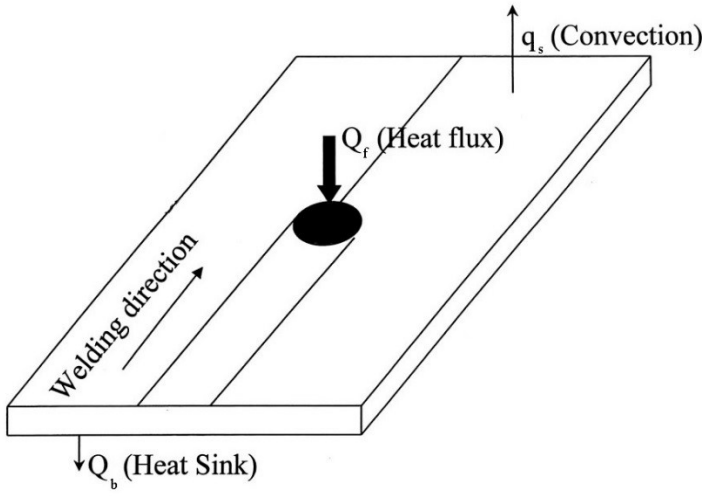

Figure 3.3 FSW thermal boundary conditions (Chao et al., 2003)

Chen and Kovacevic (2003) were one of the first researchers to propose a heat generation rate equation to calculate the heat input. By considering an element at radius *r*, the rate of the heat generated due to the friction in the interface of the tool shoulder and the workpiece surface was given by:

$$dQ_f = 2\pi\omega.r^2\mu(T)p(T)dr \tag{3.21}$$

Where ω is the angular velocity, μ is the coefficient of friction, and p is the pressure due to the plunging force. Hence the rate of heat generation over the entire interface of the tool shoulder and workpiece were obtained as:

$$(Q_f)_{shoulder} = \int_{R_{pin}}^{R_{shoulder}} 2\pi\omega.r^2 \mu(T) p(T) dr = \frac{2}{3}\pi\omega\mu(T) p(T)(R_{shoulder}^3 - r_{pin}^3) \quad (3.22)$$

where $R_{shoulder}$ and R_{pin} are the radius of the tool shoulder and tool radius. Chen and Kovacevic (2003) used the same expression to calculate the heat generation from the interface of the tool pin and workpiece. As the friction and the pressure are functions of temperature T and radius r Eqn (3.22) is difficult to evaluate. As the temperature increases the work done by the plastic deformation is expected to be increased and the friction coefficient decreases. Hence a constant value for friction coefficient might be used in the evaluation to take into account the comprehensive effects of both of the thermal and plastic effects during the FSW process.

Schmidt et al. (2004) extended the previous analytical expressions to include the heat generation due to the friction of the conical shoulder and cylindrical pin surfaces. Schmidt et al. (2004) proposed that the heat generation (W) in the interface of the tool shoulder and workpiece interface due to friction can be calculated as:

$$Q_{shoulder} = \int_0^{2\pi} \int_{R_{pin}}^{R_{shoulder}} \omega \tau_{contact} r^2 (1 + \tan\alpha) dr d\theta \quad (3.23)$$

where $\tau_{contact}$ is the shear stress in the surface, ω is the angular velocity, and α is the shoulder cone angel.

The heat generated from the pin consists of two parts, heat generated from the side surface of the pin and heat generated in the tip of the pin. Schmidt et al. evaluated that the heat generated from the pin side surface as:

$$Q_{pin,side} = \int_0^{2\pi} \int_0^{h_{pin}} \omega \tau_{contact} {R_{pin}}^2 dz d\theta \tag{3.24}$$

And the heat generated from the pin tip surface, assuming a flat tip, gave:

$$Q_{pin,tip} = \int_0^{2\pi} \int_0^{r_{pin}} \omega \tau_{contact} r^2 dr d\theta \tag{3.25}$$

Hence the total heat input, Q_f, calculated from the combination of the heat generation from the tool shoulder and pin as:

$$Q_f = Q_{shoulder} + Q_{pin,side} + Q_{pin,tip} \tag{3.26}$$

Recently Riahi and Nazari (2011) suggested that the heat generation due to the friction in the tool shoulder surface and the tool pin can be calculated as:

$$Q_{shoulder} = \frac{4\pi^2}{3} \mu N p (R_{shoulder}^3 - R_{pin}^3) \tag{3.27}$$

$$Q_{pin} = \frac{4\pi^2}{3} \mu N p (R_{pin}^3 - 3R_{pin}^2 h_{pin}) \tag{3.28}$$

where N is the number of revolution of the tool per second.

3.4 Mechanical finite element analysis

3.4.1 Fundamentals

The governing finite element equations in terms of stress for a solid element are:

$$\begin{cases} \dfrac{\partial \sigma_x}{\partial x} + \dfrac{\partial \tau_{xy}}{\partial y} + \dfrac{\partial \tau_{xz}}{\partial z} + b_x = 0 \\ \dfrac{\partial \tau_{yx}}{\partial x} + \dfrac{\partial \sigma_y}{\partial y} + \dfrac{\partial \tau_{xz}}{\partial z} + b_y = 0 \\ \dfrac{\partial \tau_{zx}}{\partial x} + \dfrac{\partial \tau_{zy}}{\partial y} + \dfrac{\partial \sigma_z}{\partial z} + b_z = 0 \end{cases} \tag{3.29}$$

where σ and τ are the normal and shear stresses and b_x, b_y, and b_z are the body force component.

The total weighted residual of each equation is obtained by multiplying it by its own weighting function ($\bar{u}, \bar{v}$ and $\bar{w}$), integrating over the volume and adding all of the three terms. Using the Green-Gauss theorem the total weighted residual can be written as (Bhatti, 2005):

$$\begin{aligned} &\iiint_V \left(\sigma_x(\bar{\varepsilon})_x + \sigma_y(\bar{\varepsilon})_y + \sigma_z(\bar{\varepsilon})_z + \tau_{xy}(\bar{\gamma})_{xy} + \tau_{xy}(\bar{\gamma})_{xy} + \tau_{xy}(\bar{\gamma})_{xy}\right) dV \\ &- \iint_S (q_x \bar{u} + q_y \bar{v} + q_z \bar{w}) dS - \iiint_V (b_x \bar{u} + b_y \bar{v} + b_z \bar{w}) dV = 0 \end{aligned} \tag{3.30}$$

where q_x, q_y and q_z are applied surface loads.

The left hand side of the Eqn (3.30) can be linearized in the form of an algebraic equations system as follows:

$$k_T \Delta d = -r_I + r_q + r_b \tag{3.31}$$

where $\boldsymbol{K_T}$ is the tangent stiffness matrix, $\boldsymbol{\Delta d}$ is the incremental displacement vector, $\boldsymbol{r_b}$ and $\boldsymbol{r_q}$ are the equivalent nodal load vectors due to body forces and surface forces respectively and $\boldsymbol{r_I}$ is the internal force vector.

3.4.2 Thermal stress

A temperature rise of ΔT in element can result in a uniform strain that depends on the thermal expansion coefficient α of the material. The temperature change does not cause shear strain, hence the resulted initial strain vector due to temperature change in a 3D element can be expressed as follows (Bhatti, 2005):

$$\varepsilon_0 = \begin{pmatrix} \alpha\Delta T \\ \alpha\Delta T \\ \alpha\Delta T \\ 0 \\ 0 \\ 0 \end{pmatrix} \tag{3.32}$$

In the presence of the initial strain ε_0 the constitutive equation can be written as follows:

$$\sigma = C(\varepsilon - \varepsilon_0) \tag{3.33}$$

where C is the stress-strain constitutive matrix. The strain energy within an element can be written as:

$$U = \frac{1}{2}\iiint_V (\varepsilon - \varepsilon_0)^T C(\varepsilon - \varepsilon_0) dV \tag{3.34}$$

Expanding the product:

$$\begin{aligned} U = &\frac{1}{2}\iiint_V \varepsilon^T C\varepsilon dV - \frac{1}{2}\iiint_V {\varepsilon_0}^T C\varepsilon dV \\ &- \frac{1}{2}\iiint_V \varepsilon^T C\varepsilon_0 dV + \frac{1}{2}\iiint_V {\varepsilon_0}^T C\varepsilon_0 dV \end{aligned} \tag{3.35}$$

The last term can be ignored as it contains all the known quantities that do not depend on the solution. Also, since C is a symmetric matrix the second and third term can be combined together. Hence the effective strain energy can be expressed as follows (Bhatti, 2005):

$$U_e = \frac{1}{2}\iiint_V \varepsilon^T C\varepsilon dV - \frac{1}{2}\iiint_V {\varepsilon_0}^T C\varepsilon dV \tag{3.36}$$

Making the substitution $(\varepsilon = B^T d)$, Eqn (4.26) becomes:

$$\begin{aligned} U_e &= \frac{1}{2} d^T \iiint_V BCB^T dV d - \iiint_V {\varepsilon_0}^T CB^T dV d \\ &= \frac{1}{2} d^T k d - {r_\varepsilon}^T d \end{aligned} \tag{3.37}$$

where $k = \iint_V BCB^T dV$ is the element stiffness matrix and ${r_e}^T$ is the external nodal load vector due to the thermal strains. As the effective potential energy is minimized, Eqn (3.27) reduces to the familiar form:

$$kd = r_{\varepsilon} \tag{3.38}$$

Chapter 4 - **Finite element study of 3D simulated welding effect in aluminum plates**

Vahid Farajkhah[a], Yi Liu[b,*] and Liam Gannon[c]

Published in: Ships and Offshore Structures,

DOI: 10.1080/17445302.2015.1123865

[a] Ph.D candidate, Dalhousie University, Department of Civil and Resource Engineering, 1360 Barrington St., Halifax, NS, Canada B3J 1Z1., Email: vahid@dal.ca

[b, *] Corresponding author. Professor, Dalhousie University, Department of Civil and Resource Engineering, 1360 Barrington St., Halifax, NS, Canada B3J 1Z1, Email: yi.liu@dal.ca

[c] Defence Research and Development Canada Atlantic, Dartmouth, Nova Scotia, Canada B2Y 3Z7, Email: liam.gannon@drdc-rddc.gc.ca

4.1 Abstract

The effects of metal inert gas (MIG) welding and friction stir welding (FSW) on the development of the heat affected zone (HAZ), residual stress and distortion fields in aluminum plates were investigated in this paper. The FSW and MIG butt welding process of two aluminum alloy 6061-T6 plates were simulated in a three-dimensional, two-step thermo-mechanical analysis using the finite element code ANSYS. The element birth and death technique was implemented in the MIG simulation to model the addition of weld metal to the workpiece and the tool plunging force and fixture release were considered in the FSW simulation. The finite element thermal results revealed that the FSW process resulted in significantly lower temperatures in comparison with MIG welding, and hence formed a smaller HAZ around the weld line. The obtained mechanical results indicated that in comparison with MIG welding, the FSW process resulted in up to 40% and 75% less peak tensile and compressive residual stresses respectively. In addition, the FSW process showed a reduction of 40% to 60% in HAZ area and also considerably smaller distortions.

4.2 Introduction

Friction stir welding (FSW) is a recently emerged solid-state joining technology primarily used on aluminum or other metals that are sensitive to welding (Thomas et al. 1991). It is believed that the first commercial application of FSW process was in the ship building industry for the welding of 6xxx series of aluminum extrusions for fishing vessels (Midling et al. 1999; Threadgill et al. 2009). Since then, FSW has become increasingly popular in the welding of aluminum extrusions in various high speed vessels as well as aluminum superstructures of large steel cruise ships (Gesto et al. 2008). As illustrated in Figure 4.1, typically in FSW process the workpieces are clamped to a back-plate to prevent the lateral movement during welding, and a cylindrical tool with a pin rotating with a speed of several hundred RPM is slowly plunged into the conjunction of the two workpieces that are to be jointed together. As the tool is plunged into the workpieces heat is generated by the friction between the surfaces of the rotational welding tool including the shoulder and pin, and the workpieces, which causes the weld material to soften into a plasticized state. As the FSW progresses along the contact line of workpieces, the plasticized material is stirred by the tool to flow to the sides and back of the tool. The stirred material forges to the other materials in the vicinity resulting in a solid phase joint between the two workpieces. During the FSW process, the generated heat is high enough to make the materials around the pin to soften for stirring action but low enough so that the material does not reach the melting temperature. Since the welding takes place at a temperature below the material melting point, the FSW process yields fine microstructure, absence of cracking and solidification defects, and no loss of alloying elements (Zhu and Chao, 2004).

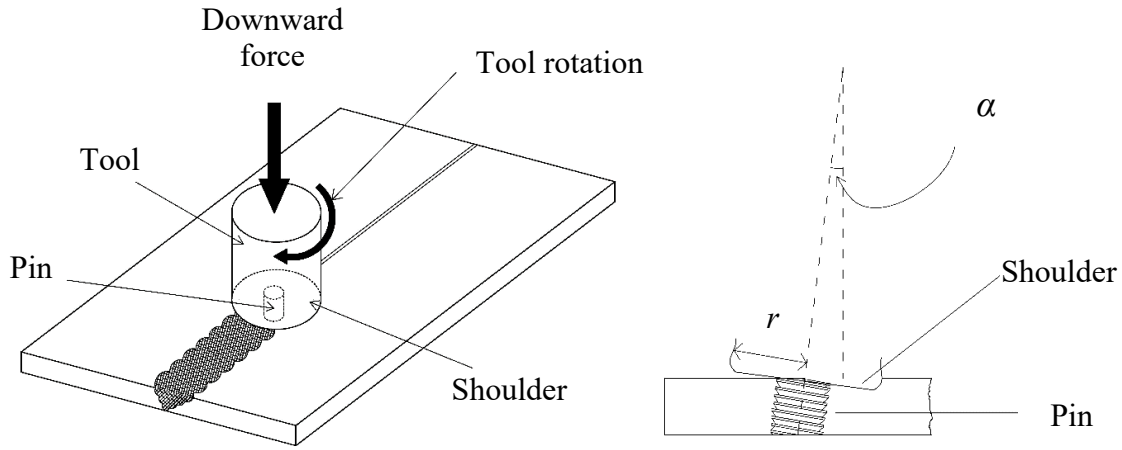

Figure 4.1 FSW process

It is commonly acknowledged that welding aluminum results in significant changes to the material properties in the area around the weld known as the heat affected zone (HAZ). Those changes can be detrimental to the performance of aluminum structures because aluminum is often heat-treated to increase strength and hardness. In 6000 series aluminum alloys for example, all the effects of heat treatment will be lost if the temperature reaches 300 °C for only a short time (Beaulieu 2006, Davis 1993). After the cooling down period, they regain about 40% to 80% of their heat treated strength. In aluminum joints welded by FSW, the reduction of the yield stress in HAZ is not only affected by the high temperature fields but also by the mechanical deformation during the FSW process. Previous studies have reported reductions in the range of 30-60% in yield stress in the HAZ for different types of aluminum alloys (Mahoney et al. 1998; Reynolds and Duvall 1999). Chao and Qi (1998) defined the extent of HAZ in FSW of aluminum as the area that experienced 300 °C and higher. They also defined a semi-HAZ area where the material reached a temperature between 200 °C and 300 °C and has a material strength between the strength of HAZ and base material.

Most existing research on the FSW process focused on the thermal aspects of FSW. While some experimental work was conducted (Tang et al. 1998; Chao et al. 2003), more studies were based on three-dimensional heat flow numerical models to investigate the heat generation and temperature distribution during the FSW (Gould 1998; Frigaard et al. 2001; Chao et al. 2003; Song & Kovacevic 2003; Schmidt et al. 2004). The results revealed that the heat generation during the FSW process was mainly due to the contact condition between the tool shoulder and workpieces, and most of the generated heat flowed to the workpieces. Zhang and Zhang (2007, 2008) developed a thermo-mechanical finite element model of FSW for 6061-T6 aluminum alloy and studied the effect of the shoulder rotating speed and welding speed on the temperature distribution, and material deformation. The study showed that the temperature field was approximately symmetrical to the welding line and the maximum temperature in the FSW process increased with the speed of tool rotation.

Where FSW induced residual stress and distortion fields are concerned, existing studies are limited in that potentially significant aspects of the process are often not considered. One of the first studies on the finite element modeling of FSW residual stress was carried out by Chao and Qi (1998, 1999). They developed a moving heat source model for FSW of 6061-T6 aluminum plates based on a reverse engineering method and then studied the residual stresses caused by thermal effects. However, tooling geometry and plunging force from the welding tool to the workpieces were not modeled. Zhu and Chao (2004) developed a 3-D nonlinear thermo-mechanical finite element model to simulate the FSW of 304L stainless steel plate. This is one of few studies that took into account the changes in material strength at the HAZ, however the plunging force was ignored.

Khandkar et al. (2006) used a thermo-mechanical finite element model to simulate the transient temperature and residual stress in the FSW of aluminum alloys of 2024 and 6061 as well as stainless steel 304L. Neither development of the HAZ nor the plunging force were considered in the modeling. The aforementioned studies generally concluded that the longitudinal residual stress is predominant and that the transverse residual stress is considerably smaller. The maximum longitudinal residual stress due to welding can range from 50% to 100% of the yield strength of the base material in aluminum plates. A higher traveling speed of welding tool causes higher longitudinal residual stress in a narrower region. However, ignoring the modeling components such as HAZ and plunging force were believed to attribute to the discrepancies between the finite element and experimental results reported in these studies.

As friction stir welding gains popularity with materials such as aluminum whose strength may be sensitive to welding, a comparison with traditional metal inert gas (MIG) welding in terms of welding induced residual stress, distortion, and heat affected zone is necessary. In this study both the FSW and MIG butt welding of aluminum 6061-T6 plates were simulated using the finite element code ANSYS. To the authors' knowledge, this study is the first where FSW and MIG welding induced residual stress and distortion considering the effect of HAZ in aluminum plates are examined and compared. The 6061-T6 alloy was selected because it is the most popular 6000 series alloy and is widely used in ship building. The modeling was carried out by sequential two-step thermal-structural analyses, where the mechanical force between the traveling welding tool and the workpiece as well as the development of HAZ during the welding process were considered. The model was validated by comparison against experimental results obtained for both MIG welding

and FSW processes. A parametric study was also conducted to investigate the effects of plate thickness and welding speed on FSW induced residual stresses and distortions.

4.3 Numerical simulation

A two-step finite element modeling procedure was used for the simulation of both FSW and MIG welding process using ANSYS. In the first step of analysis, the thermal loads due to FSW and MIG welding were simulated and applied to the model and a nonlinear transient thermal analysis was performed to determine the time-dependent temperature distribution. In the second step, the temperature field history calculated from the thermal analysis, and also the plunging force in the case of FSW were applied to the structural model as a series of loads, where each load step represented an increment in the position of the traveling welding tool. A structural analysis was then performed to provide the residual stresses and distortions induced by the welding. The meshing patterns for both of the thermal and structural analysis were the same but with different element types. The SOLID70 thermal element was used in the thermal model whereas its equivalent structural element SOLID185 was used in the structural model. The SOLID70 element has eight nodes with a single degree of freedom, i.e. temperature, at each node whereas SOLID185 element also has eight nodes but having three degrees of freedom at each node: translations in the nodal x, y, and z directions.

Temperature dependent thermal and mechanical material properties were incorporated in the models. The thermal material properties required are density, specific heat and thermal conductivity, and the mechanical material properties include Young's

modulus, yield stress and thermal expansion coefficient. For the Poisson's ratio a constant value of 0.33 was considered over the temperature history. Temperature dependent mechanical and thermal material properties for 6061-T6 were adopted from Riahi & Nazari (2011), and the temperature dependent heat transfer coefficient was adopted from Moraitis and Labeas (2008). The details are shown in Figure 4.2.

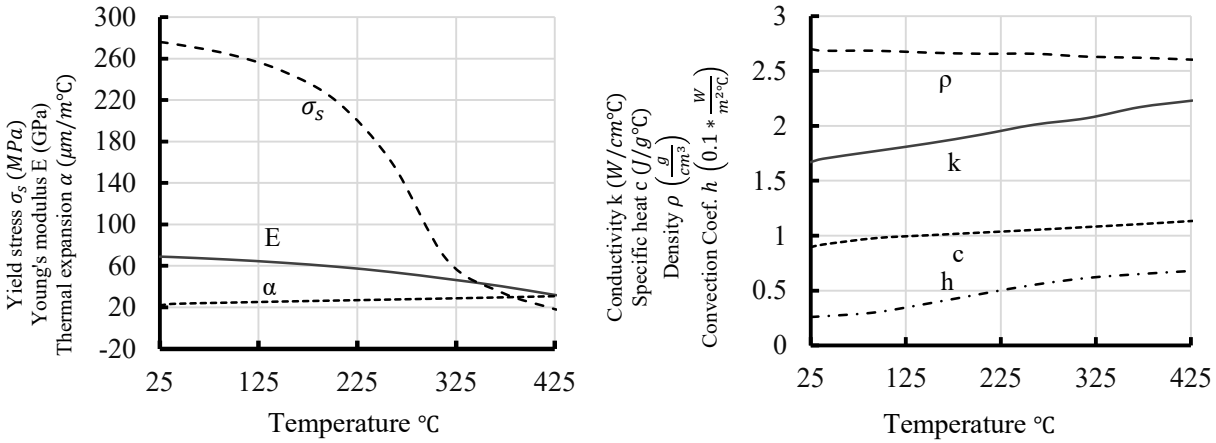

Figure 4.2 Temperature dependent material properties for aluminum alloy 6061-T6 (Riahi & Nazari, 2011)

Similar to concepts used by Chao and Qi (1998), it is assumed in this study that the weld area was divided into three zones, i.e., HAZ, semi-HAZ, and base metal zone. The correlation between the strength in these zones and temperature is summarized in Table 4.1. In the finite element analysis of both the FSW and MIG welding processes, as welding progressed the average temperatures of elements were queried and the material properties of those elements were changed corresponding to the maximum average temperature according to Table 4.1.

Table 4.1 Material strength with respect to temperature

	Temperature T	% of yield stress of base metal
HAZ	T ≥ 300 ºC	60
Semi-HAZ	200 ºC ≤ T< 300 ºC	80
Base metal zone	T < 200 ºC	100

4.3.1 Finite element simulation of MIG welding

The MIG welding process was modeled in a two-step nonlinear analysis based on a similar approach developed by Gannon et al. (2010). In this case, butt welding of two plates was simulated. A typical finite element meshing was developed for the current study and the boundary conditions are shown in Figure 4.3. A mesh convergence study revealed that a relatively dense mesh was required in the region surrounding the weld. The boundary conditions were applied such that the model can deform in all directions so that the thermal expansion and contraction were not restricted. In this study it is assumed that 60% of the total heat input of welding was transferred to the work piece via the molten metal droplets and the other 40% was transferred by surface heat flux (Pardo & Wekman, 1989). The total heat input of welding can be calculated using Eqn (4.1) as follows:

$$Q = \eta VI \tag{4.1}$$

where V is the arc voltage, I is the arc current, and η is the arc efficiency which is assumed to be 0.85 for CO_2 gas metal arc welding (Michaleris et al. 1997). The heat of the molten metal droplets was described by a volumetric heat generation and for the heat flux a Gaussian distribution with an arc radius of 5 mm was assumed based on work by

Kumaresan et al. (2011) and Zhu and Chao (2002). The Gaussian distribution is defined relative to the coordinate system of the traveling heat source and it is expressed as:

$$q(x,\xi) = \frac{3Q}{\pi c^2} e^{-3x^2/c^2} e^{-3\xi^2/c^2} \tag{4.2}$$

where c is the radius of the welding arc. User-defined macros were created using parametric design language (APDL) to model the movement of the heating source and the deposition of molten metal droplets on the workpiece. Heat loss due to the combined effects of convection and radiation was accounted for by using a temperature dependent heat transfer coefficient (Figure 4.2) on the free surfaces of the work piece (Moraitis and Labeas, 2008).

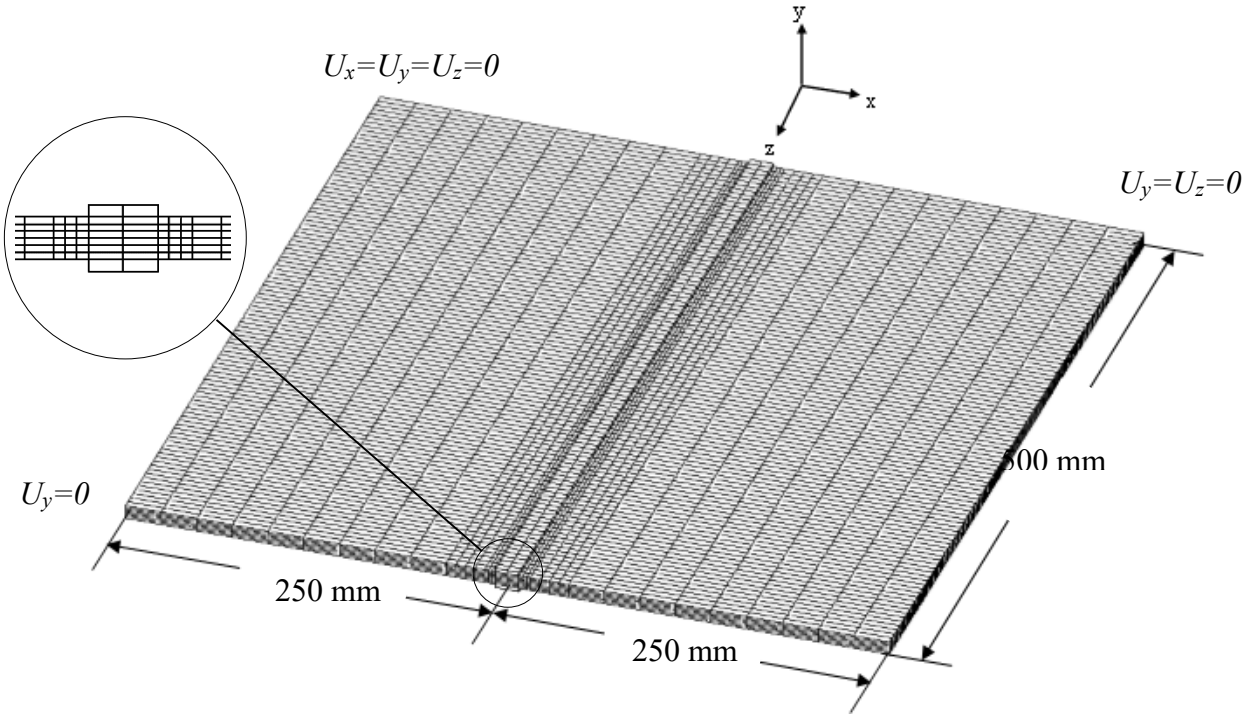

Figure 4.3 Typical meshing pattern of MIG finite element model and boundary conditions

In the structural analysis, the temperature field time history calculated from the thermal analysis was applied to the model as a series of thermal loads, where each load step represented an increment in the weld deposition. To correctly model the addition of the molten weld metal to the workpiece, the element birth and death feature available in ANSYS was used (Playdon & Simmonds, 1984). In the beginning of the structural analysis all of the weld elements were deactivated (killed). As the weld progressed a subroutine was used to apply the calculated temperature field at the corresponding time and to calculate the average temperature of the welded elements. Those welded elements whose temperature had fallen below the solidification temperature, which is 610 ^{o}C for aluminum 6061-T6, were activated again simulating the deposition of the weld elements on the work piece. The weld elements were activated with no strain history and their reference temperature was set to the solidification temperature in order to calculate the thermal strains (Gannon et al. 2010).

To verify the model for MIG welding process, experimental results obtained by Masubuchi (1980) were used where the welding of an aluminum plate was conducted. The geometry and welding configuration of Masubuchi (1980) test are shown in Figure 4.4. The plate was simply supported on both ends and the upper longitudinal edge of the plate was welded by MIG welding. The plate was made of aluminum alloy 5052-H32 and measured 1220 mm long, 152.4 mm wide and 12.5 mm thick. The welding parameters and material properties were given by Masubuchi (1980).

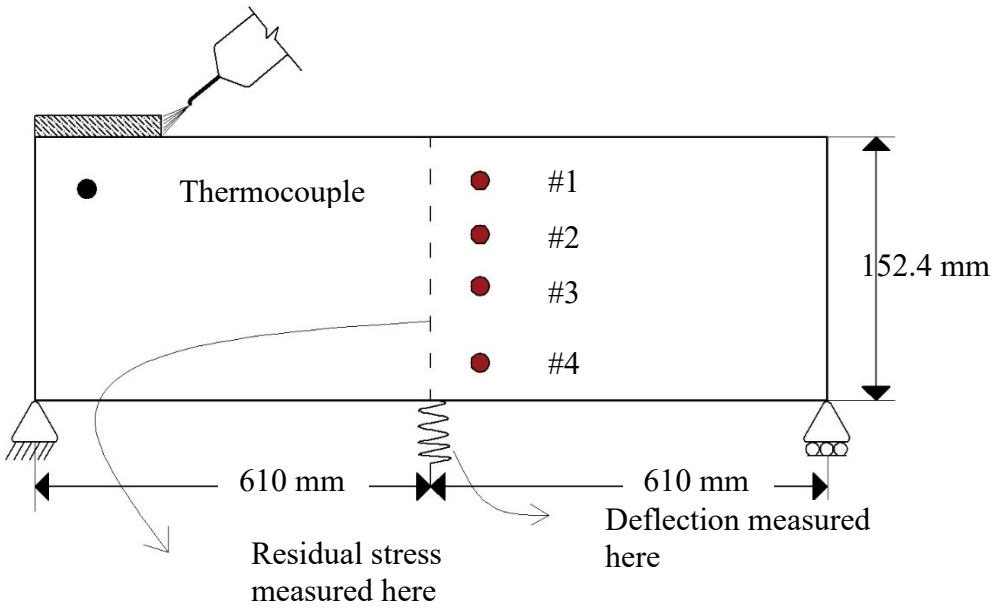

Figure 4.4 Test setup of Masubuchi (1980)

Figure 4.5 compares the finite element and experimental results of temperature history. Figure 4.6 compares the structural results including the transient vertical deflection at the mid-point of the plate and the longitudinal residual stresses in the mid-thickness of the cross-section. The figures show that the finite element results compare well with the test results in both temperature distribution and the resulting deformation and residual stress.

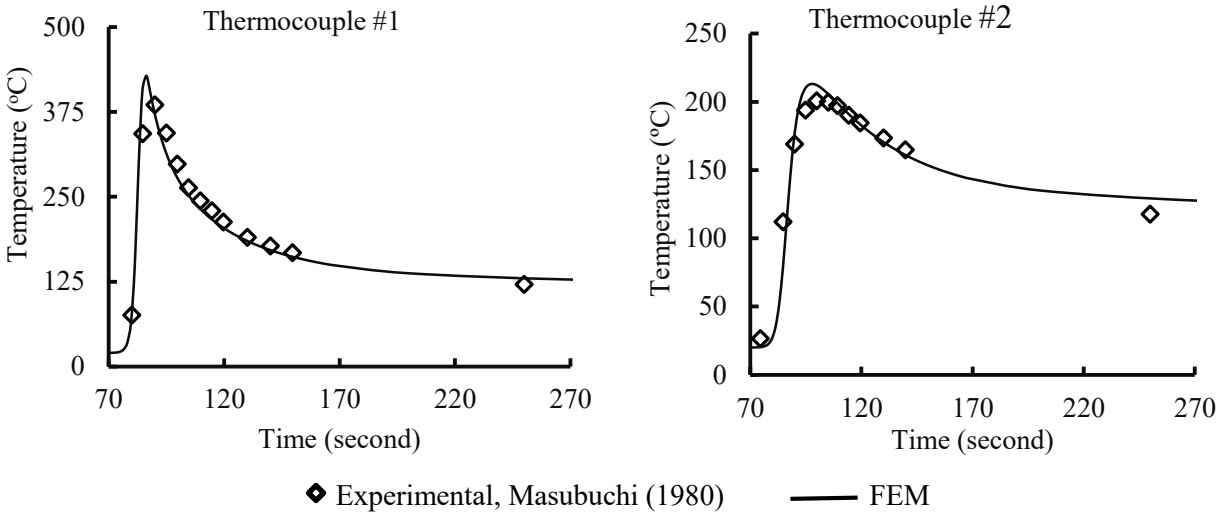

Figure 4.5 Comparison of temperature history at thermocouples

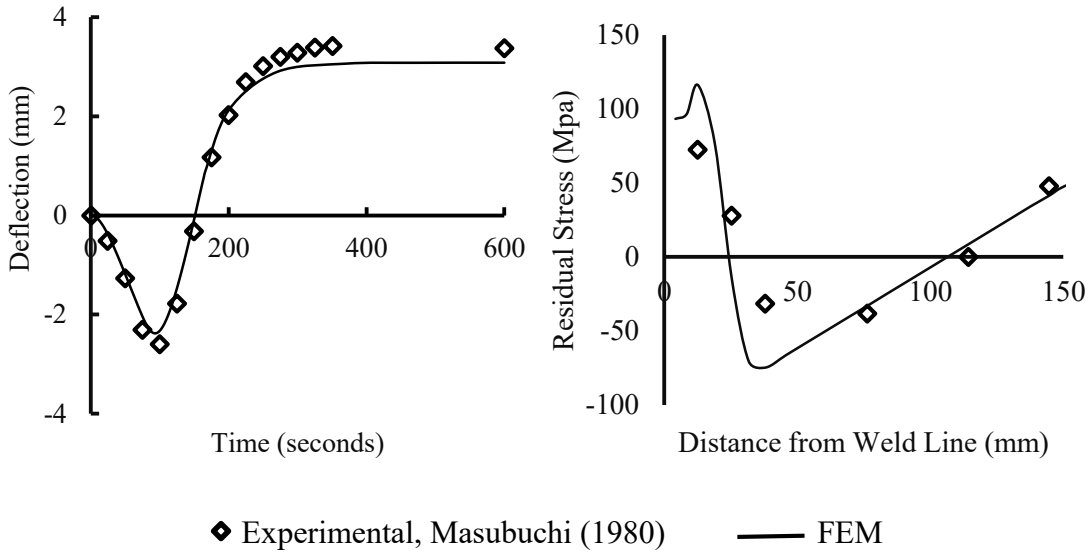

Figure 4.6 Comparison of transient vertical deflection and longitudinal residual stress at the middle of the plate

4.3.2 Finite element simulation of FSW

The weld zone in the finite element modeling was defined as the interface of the weld tool and the workpieces. The finite element meshing pattern used for the FSW process simulation and the applied boundary conditions are shown in Figure 4.7. The highlighted areas in the figure indicate the location of the clamping fixture applied to the plates. In mechanical simulation the boundary conditions representing the backing plate and clamps were applied where the vertical deflection of all nodes in highlighted area was restrained. After the welding was complete and the workpieces cooled down to the room temperature, the clamps were released in the last step of analysis to allow the redistribution of residual stresses.

The key component of friction stir welding simulation is the modeling of heat generation. The energy balance at any time during the FSW requires the following (Chao et al. 2003):

$$Q_f = q_s + Q_b + Q \tag{4.3}$$

where Q_f is the heat flux due to the tool shoulder and pin interface friction with the workpiece; q_s is the heat loss due to convection and radiation at the free surfaces; Q_b is the heat loss from the bottom surfaces of the workpiece due to the heat conduction to the backing plate; and Q is the increase of the heat content in the workpiece (W). The heat flux Q_f is expected to be constant except in the beginning and the end of the FSW process since it is only dependent on the physical interaction between the tool pin/shoulder and the

workpiece. Hence a moving heat source with a constant Q_f was considered in the finite element simulation.

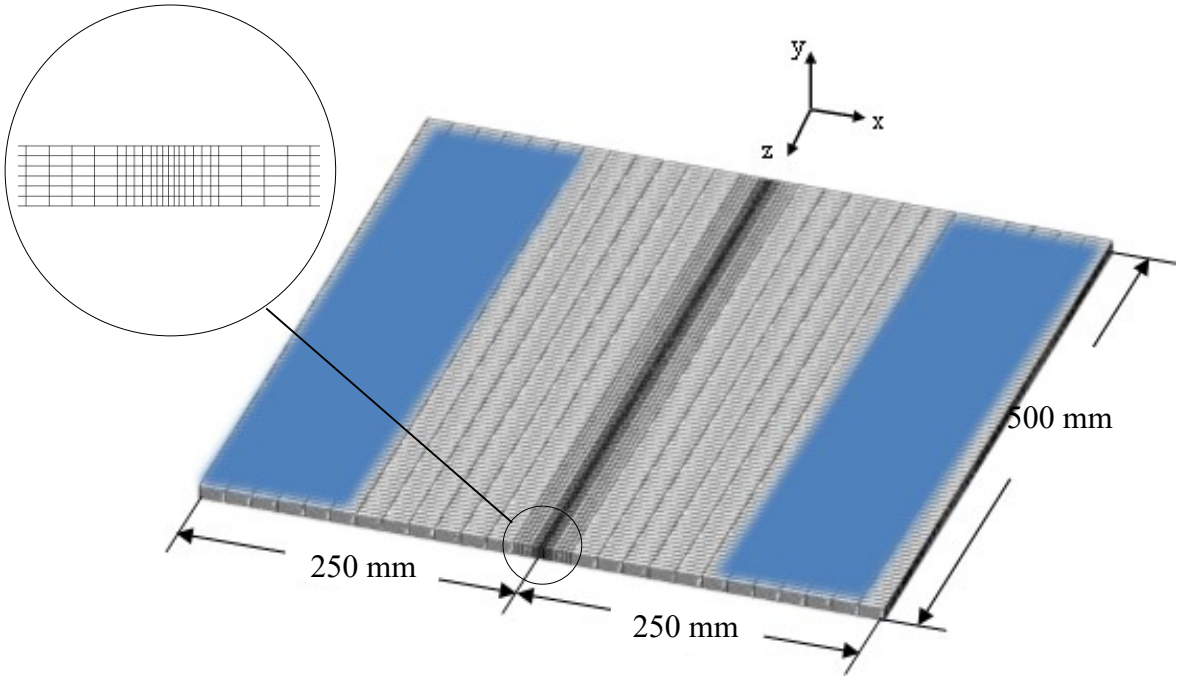

Figure 4.7 FSW finite element mesh and boundary conditions

In this study the heat generated due to friction during the FSW was considered to have three components using the method provided by Schmidt et al. (2004). They included the heat generated at the interface of the tool shoulder and workpiece, $Q_{shoulder}$; and the heat generated from the side surface of the pin, $Q_{pin,side}$, and on the tip of the pin, $Q_{pin,tip}$. The expressions for them are as follows:

$$Q_{shoulder} = \int_0^{2\pi} \int_{R_{pin}}^{R_{shoulder}} \omega \tau_{contact} r^2 (1 + \tan\alpha) dr d\theta \tag{4.4}$$

$$Q_{pin,side} = \int_0^{2\pi} \int_0^{h_{pin}} \omega \tau_{contact} R_{pin}{}^2 dz d\theta \tag{4.5}$$

$$Q_{pin,tip} = \int_0^{2\pi} \int_0^{r_{pin}} \omega \tau_{contact} r^2 dr d\theta \tag{4.6}$$

where $\tau_{contact}$ is the shear stress in the surface, r is the radius of shoulder, ω is the angular velocity, and α is the shoulder cone angle as shown in Figure 4.1. Hence the total heat input, Q_f (W), can be calculated from the combination of the heat generation from the tool shoulder and pin as:

$$Q_f = Q_{shoulder} + Q_{pin,side} + Q_{pin,tip} \tag{4.7}$$

This generated heat due to friction between the tool shoulder/pin and the workpiece was modeled as heat fluxes in the corresponding interface areas, moving with the weld speed. The heat input was assumed to be linearly proportional to the distance from the tool centerline to the edge of the shoulder based on the assumptions that the plunging force applied to the workpiece from the tool shoulder creates a uniform pressure and the heat is generated from the work done by the friction force. The heat fluxes were applied to the materials under the tool with a distribution given by Chao et al. (2003):

$$q(r) = \frac{3Q_f r}{2\pi R_{shoulder}^3} \tag{4.8}$$

where $R_{shoulder}$ is the outside radius of the shoulder of the tool and Q_f is the total heat input calculated using Eqn (4.7). On the boundary of the surfaces of the workpiece, the heat loss to the ambient temperature is caused by the heat transfer through convection and radiation.

The heat loss in all surfaces, except for the bottom surface where the workpiece is attached to the backing plate, is evaluated as (Zhu and Chao, 2004):

$$q_s = \beta(T - T_0) + \varepsilon B(T^4 - T_0^4) \tag{4.9}$$

where T_0 is the room temperature, ε is the emissivity of the plate surface and B is the Stefan-Boltzmann constant which equals to $5.67 \times 10^{-8} Wm^{-2}k^{-4}$, and β is the heat transfer coefficient as given in Figure 4.2.

The heat loss from the bottom surfaces due to heat conduction between the workpiece and the backing plate is evaluated as:

$$Q_b = \beta_b(T - T_0) \tag{4.10}$$

where β_b is the convection coefficient between the workpiece surface and the backing plate and it is assumed to be $350\, W/m^2K$ based on the work of Chao et al. (2003).

In the mechanical modeling, two types of loading were assumed including the transient temperature calculated from the thermal analysis, and the pressure due to the tool plunging force. The pressure, *P,* due to the plunging force applied to the workpiece by the tool shoulder was modeled as uniform pressure moving forward with the speed of welding and it is expressed as follows:

$$P = \frac{F}{A_{shoulder}} \tag{4.11}$$

where $A_{shoulder}$ is the area at the interface of the tool shoulder and the workpiece.

For the verification of the model developed for the FSW process, two experimental studies were used. The model was first verified for the transient temperature distribution and welding induced residual stress using experimental results obtained by Zhu and Chao (2004) on steel plates. The model was then verified with experimental thermal results obtained by Guo et al. (2014) on aluminum plates. The test setup of Zhu and Chao (2004) consisted of plates made of 304L stainless steel, measuring 304.8 mm long, 101.6 mm wide and 3.18 mm thick. Figure 4.8 compares the finite element and experimental results for the temperature distribution along the transverse direction of the workpiece. A good agreement between the finite element and experimental results is obtained. Figure 4.9 shows the comparison of longitudinal residual stresses measured 0.55 mm below the surface of the cross-section in the mid-length of the workpiece after the release of the clamps. Note that no experimental results were obtained before the release of the clamps, numerical results obtained both before and after the release of the clamps are shown in the figure. Also included in the figure are the numerical results obtained by Zhu and Chao (2004). It is observed that the longitudinal residual stress after the release of clamps decreased significantly as shown by both finite element models.

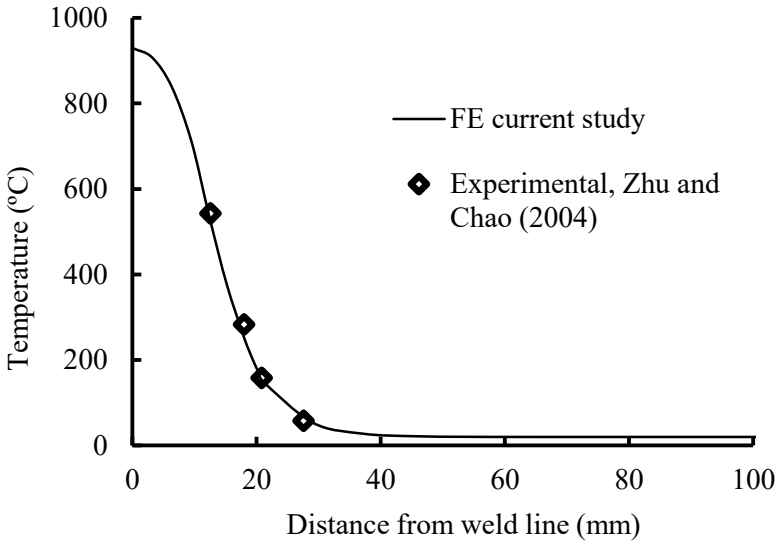

Figure 4.8 Comparison of temperature distribution along the transverse direction

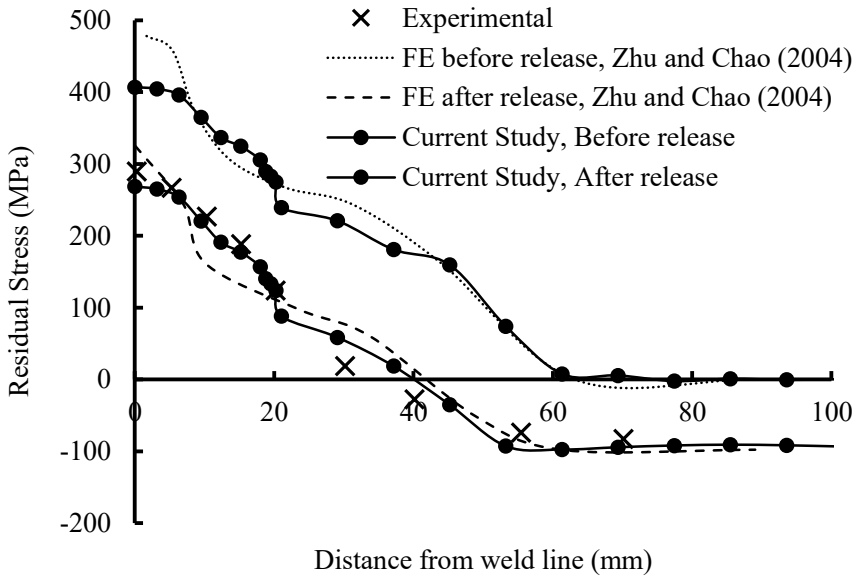

Figure 4.9 Longitudinal residual stress along the cross-section

Guo et al. (2014) obtained the temperature history of a plate of aluminum alloy 6061 welded to a plate of aluminum alloy 7075 using friction stir welding. Figure 4.10 shows the calculated temperature history where there is a good agreement between the finite element and the experimental results.

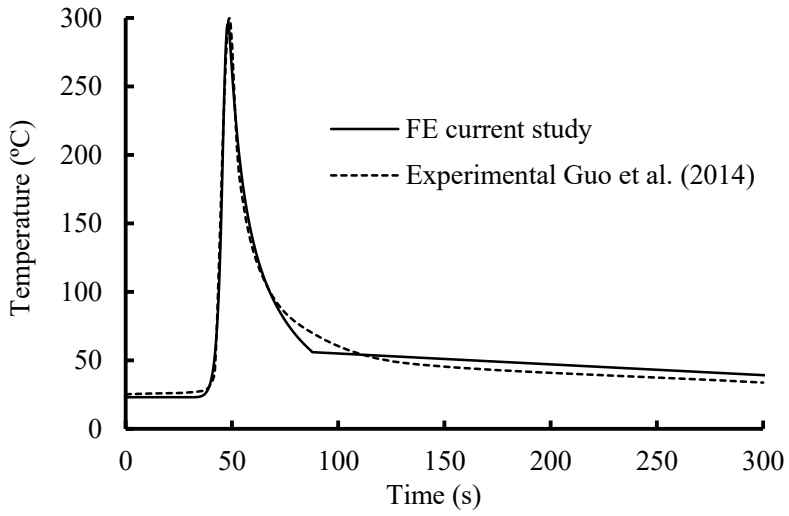

Figure 4.10 Comparison of temperature history profile at 10 mm away from the weld line

In summary, verification of the finite element model shows that the model is capable of simulating heat generation due to friction and plunging force as well as residual stress caused by friction stir welding, accounting for the release of clamping force.

4.4 Comparison study

Models of two plates being joined together by both the MIG welding and FSW processes were developed and results on the temperature distribution, residual stress and distortion fields were compared. The plates used were 6061-T6 aluminum alloy, both measuring 250 mm wide by 500 mm long. Meshing and dimensions of MIG and FSW models are shown in Figure 4.3 and Figure 4.7, respectively. Thicknesses of 4, 6 and 9 mm were considered. The MIG welding input parameters including voltage/current and welding speed, were adopted from Lincoln Arc Welding Foundation (2000) and are shown in Table 4.2. The MIG welding of the 4 mm thick plates was carried out on one side of the plates in a single pass whereas for the 6 mm and 9 mm thick plates both sides of the plates were welded in a single pass on each side. The plates were allowed to cool for 30 minutes after the welding of the first side, and were cooled to 20 ºC following the welding of the second side.

Table 4.2 Details of finite element models and MIG welding parameters

Model thickness (mm)	Voltage (V)	Current (A)	Speed (mm/min)
4	26	140	600
6	28	200	600
9	30	260	430

The FSW process details used in this study were adopted from Guo et al. (2014). The welding tool had a shoulder diameter of 15 mm and a pin diameter of 5 mm. The plates were supported on a backing plate, and were clamped by L-shaped steel strips through their

length at the distance of 125 mm from the weld line. The FSW process was carried out using tool rotational speed of 1200 rpm with a welding speed of 5 mm/s. The plunging force applied from the welding tool to the workpiece of 6.4 mm aluminum plates was measured between 6 and 7 kN. In the current study plunging forces of 5 kN, 6 kN and 7 kN were applied to the 4 mm, 6 mm and 9 mm models respectively. These welding parameters are considered typical for friction stir welding on aluminum plates. To have a thorough evaluation of FSW process, effects of varying welding tool speed and plunging force on the temperature distribution and residual stress were further investigated. Two additional tool speeds of 3 mm/s and 7.5 mm/s as well as a plunging force of 7 kN were considered in the analysis of 6 mm thick plates.

4.4.1 Thermal results

Figure 4.11 presents the simulated temperature distribution caused by FSW and MIG welding in the top surface and mid-thickness of the cross-section at the mid-length of the plate when the welding tool reaches this cross-section. It shows that for all three thicknesses considered, the finite element maximum temperatures for FSW ranged from 472 ºC to 500 ºC, and as expected, the maximum temperature occurred at the top surface of the plate which was in direct contact with the welding tool. These maximum temperature values were about 110 ºC to 140 ºC less than the melting temperature of aluminum alloy 6061-T6 and are within an acceptable range for FSW process (Chao and Qi 1998; Riahi and Nazari 2011). Figure 4.11 also shows that an area with temperature reaching 300 ºC or higher extended up to 9 mm from the weld centerline in each direction. This area is the HAZ formed by FSW process. It is also observed that the varying thickness had negligible impact on the temperature distribution and the extent of HAZ for the FSW process. On

the other hand, the HAZ extent caused by MIG welding measured 15 mm from the weld line in each direction for the 4 mm and 6 mm thick plates and 21 mm from the weld line for the 9 mm thick plates, which were 1.5 to 2.5 times HAZ caused by FSW process.

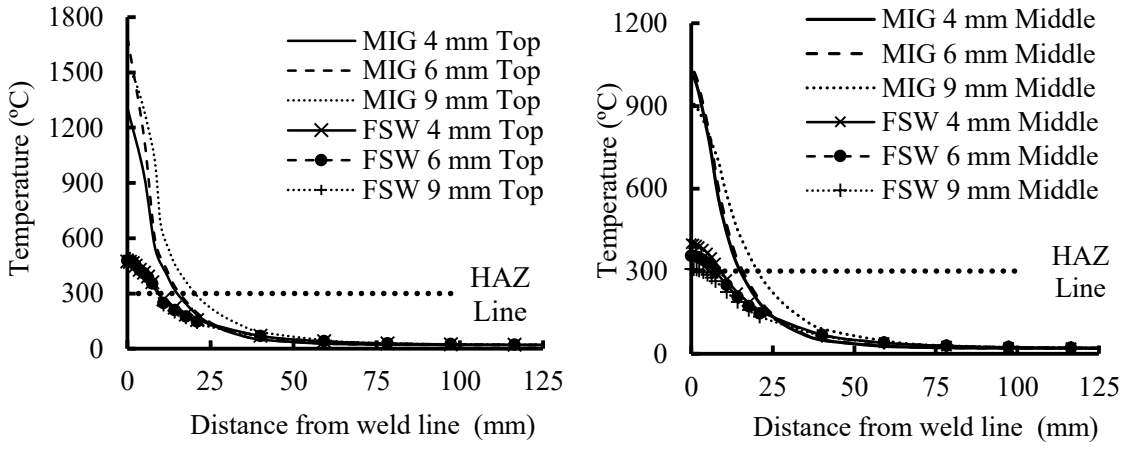

Figure 4.11 Temperature distributions along the transverse direction

Figure 4.12 further shows the through thickness temperature distribution in the cross-section during the FSW process for 6 mm thickness model. The models with 4 and 9 mm thickness showed similar temperature distribution patterns. As can be seen, in the mid-thickness of the cross-section the temperature was significantly less than the top, and the temperature decreased quickly through the thickness of the plate. This is mostly due to the relatively higher conduction in the bottom of the workpieces which are in contact with the backing plate.

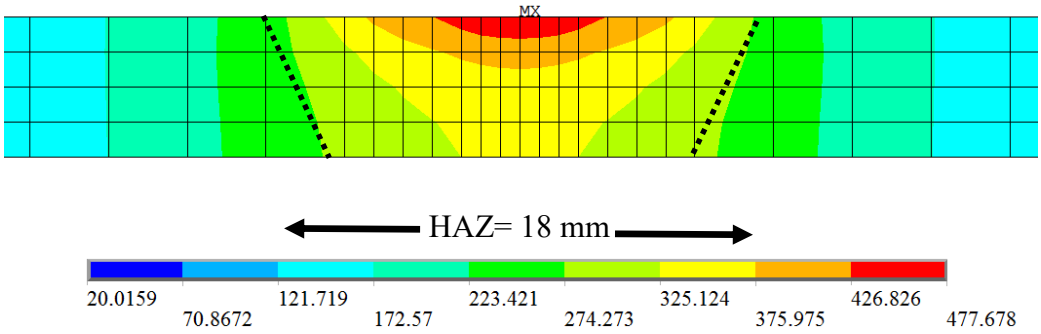

Figure 4.12 FSW temperature distribution at mid-length cross-section of the 6 mm model

Figure 4.13 shows the effect of varying welding speed and plunging force on the temperature distribution of the plates. It can be seen that as the welding speed decreased the maximum temperature and the HAZ width during the FSW process increased. For 6 mm thick plates, the maximum temperature during the process with a welding speed of 7.5 mm/s was 428 ºC as opposed to 528 ºC with a welding speed of 3 mm/s and the extent of the HAZ also increased from 7.5 mm to 11 mm as welding speed decreased. Figure 4.13 also shows that keeping the welding speed constant, when the plunging force increased from 6 kN to 7 kN, the maximum temperature in the model increased from 477 ºC to 547 ºC and the extent of the HAZ increased from about 7.5 mm to 11 mm.

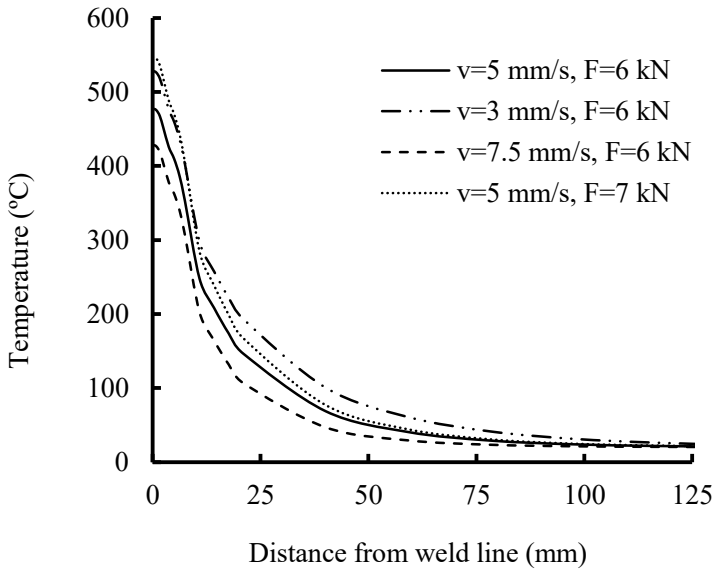

Figure 4.13 Temperature distributions for the FSW model with different welding parameters

4.4.2 Residual stress and distortion results

For the friction stir welding process, the clamps for securing the plates in place were released after welding and the plates were cooled down to the room temperature. Figure 4.14 shows the longitudinal residual stress distribution in the 6 mm model before and after the release of the clamps. It can be seen that the residual stress changed markedly after the clamp release. Thus the fixture release in the FSW must be considered in the numerical simulation of residual stress. In the current study, the FSW induced residual stresses are reported after the fixture release. The residual stresses in MIG welding are reported when the plates were cooled to the room temperature after welding.

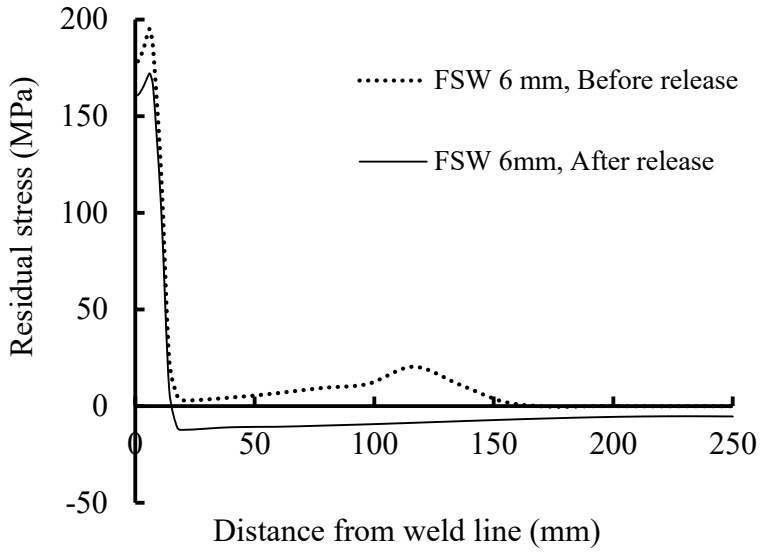

Figure 4.14 FSW induced longitudinal residual stress at mid-length cross-section before and after the fixture release

Figure 4.15 shows the variation of the longitudinal residual stresses obtained at mid-thickness in the mid-length cross-section of the models for both FSW and MIG welding. The FSW process resulted in significantly lower residual stresses in comparison with MIG welding. The maximum tensile residual stress caused by FSW varied between 164 to 171 MPa when plate thickness decreased from 9 mm to 6 mm, and the width of the tensile residual stress was 28.5 mm. For all models, the maximum tensile residual stresses developed about 6 mm away from the weld line. The developed tensile residual stresses were balanced with compressive residual stresses away from the weld line. The maximum compressive residual stress developed in the FSW models ranged from 11 MPa to 13 MPa, and decreased to 5 MPa at the edges of the plate. It also shows that the thickness of the plate did not have any significant effect on the residual stress magnitude and distribution in models welded by FSW process.

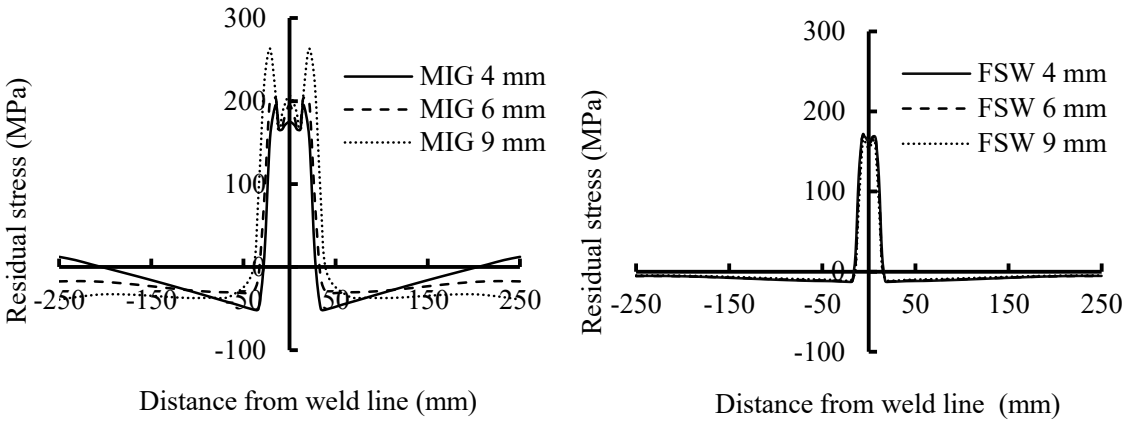

Figure 4.15 MIG & FSW induced longitudinal residual stress at mid-length cross-section

However, for MIG welding models, relatively high residual stresses were developed, and tensile residual stresses were formed in a wider area. The maximum tensile residual stress was developed for 9 mm thick plate which was 263 MPa and was located 21 mm away from the weld line in each direction and the width of the tensile residual stress zone was 80 mm. The tensile residual stress was balanced by the compressive residual stresses ranging between 33 MPa and 39 MPa. It also shows that as the plates became thicker, the residual stress magnitude increased. Recalling that the maximum tensile and compressive residual stresses for the 9 mm model joined by FSW process were 162 MPa and 9 MPa respectively, this observation shows that for 9 mm plates, FSW process resulted in 40% less maximum tensile stress and 75% less maximum compressive stress in comparison with MIG welding. It is noted that the maximum tensile residual stress occurred in the edges of the HAZ zone and the magnitude of the tensile residual stress at the weld line was smaller. This residual stress pattern is in accordance with the

experimental observations by other researchers (Feng et al. 2004) and can be attributed to the weaker material strength in the HAZ.

Figure 4.16 shows the vertical deflection of the plates welded by FSW in the mid-length cross-section after the release of the clamps. For all three thicknesses, the deflections caused by FSW process were small. The maximum deflection occurred in the 9 mm model and was 0.4 mm. Even smaller deflections were observed as the plate thickness decreased. The relatively low deflections caused by FSW process can be attributed to the low level of maximum temperature material experienced during the welding and also to the fixtures used to clamp the workpieces to the backing plate during the welding process. Figure 4.17 shows the vertical deflection of the MIG welding models in the transverse mid-length cross-section as well as the vertical deflection in the longitudinal direction along the weld line. The maximum distortion occurred in the 4 mm model, where a single weld pass resulted in an 8 mm relative distortion at the mid-length cross-section. For the 6 mm and 9 mm models, the maximum relative vertical distortions at the mid-length cross-section were approximately 6 mm and 3 mm respectively. It can be deduced that if the vertical deflection in the longitudinal direction was taken into account, the relative distortion will be even more significant. All these values were much greater than distortion due to the FSW process.

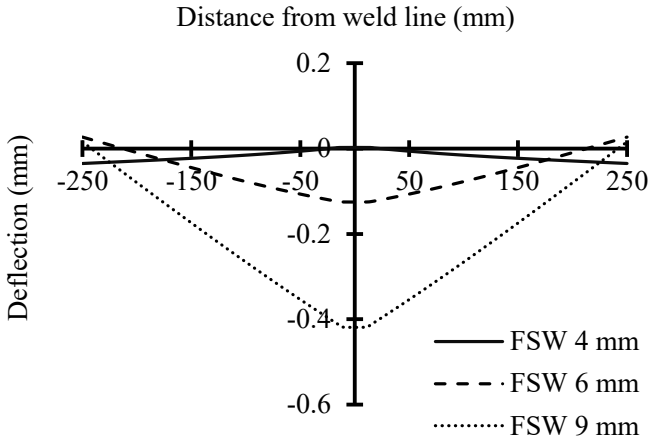

Figure 4.16 Vertical deflections at the mid-length cross-section of FSW models

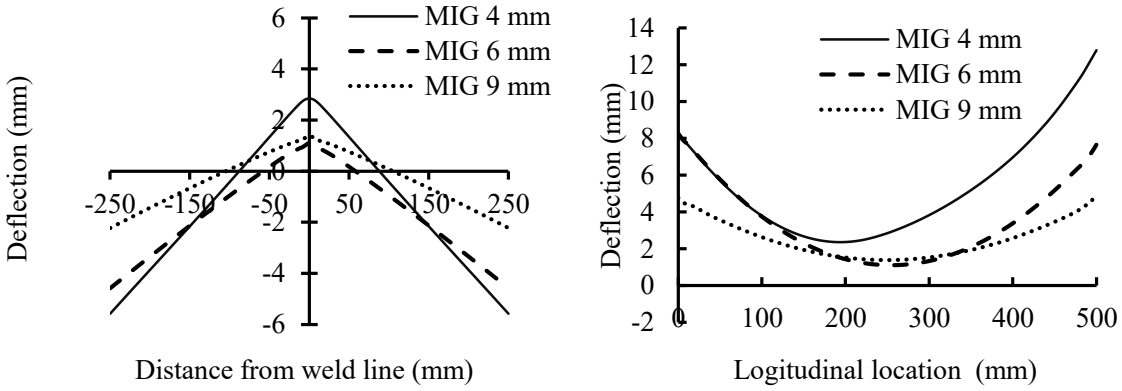

Figure 4.17 Vertical deflections in mid-span cross-section and along the weld line of MIG models

Figure 4.18 shows the effect of varying welding speed and plunging force on the residual stress distribution of plates. It can be seen that for a given welding speed, an increase in the plunging force from 6 kN to 7 kN did not have a significant effect on the residual stress distribution. However, for a given plunging force, an increase in welding

speed resulted in higher tensile stress but distributed within a narrower area and a reduction in the compressive residual stress. As the welding speed increased from 3 mm/s to 5 mm/s, the magnitude of the maximum tensile residual stress increased from 166 MPa to 172 MPa while the compressive residual stress decreased from 15 MPa to 12 MPa. Although there were changes in the residual stress, the magnitudes of the changes were marginal and hence in a practical standpoint, the effect of change in speed and plunging force from typical values can be considered negligible.

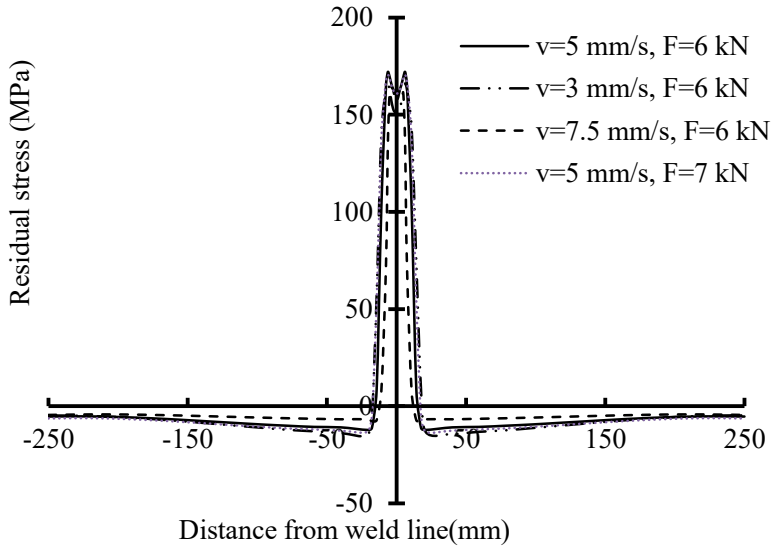

Figure 4.18 Residual stress at the mid-length cross-section of FSW models

4.5 Conclusions

A three-dimensional, two-step thermo-mechanical model was developed to simulate both the friction stir welding and metal inert gas welding processes. The model was verified with experimental results by comparison of transient temperature, residual stress and distortions. The finite element simulation was then used to examine and compare

the temperature fields, heat affected zone, residual stress and distortion generated during FSW and MIG welding of two aluminum alloy 6061-T6 plates. Some conclusions stemming from the study are as follows:

The thermal results indicated that while the maximum temperature during the FSW was about 80% of the aluminum melting point, the temperature caused by MIG welding reached up to 300% higher than the melting point of the material. The MIG welding resulted in a wider HAZ than the FSW process. For the models considered, the extent of HAZ as a result of MIG welding was about 1.5 to 2.5 times that caused by FSW process.

The structural results revealed that for all models studied, FSW resulted in up to 40% lower peak tensile and 75% lower peak compressive residual stress in comparison with MIG welding. In both of the FSW and MIG welding the maximum tensile residual stress occurred at the edges of the HAZ. While the thickness of the plates did not have a significant effect on the magnitude of the residual stresses caused by FSW, for MIG welding the residual stresses increased as the plates became thicker. In the case of welding induced distortion, the results indicated that MIG welding resulted in a considerable level of distortion in both transverse and longitudinal directions and this distortion increased as the plate thickness decreased. In comparison, the distortions due to FSW process were almost negligible. An increase in welding speed resulted in higher tensile stress distributed within a narrower area and a reduction in the compressive residual stress. However, either the increase or reduction was not significant from a practical standpoint for the welding speed and plunging force considered.

In summary, the FSW process showed better performance in lowering residual stress and distortions and resulting in a smaller HAZ than conventional MIG welding in aluminum plates.

Acknowledgements

The authors wish to recognize the contribution of financial assistance by the Natural Sciences and Engineering Research Council of Canada.

Chapter 5 - **Effect of metal inert gas welding on the behaviour and strength of aluminum stiffened plates**

Vahid Farajkhah [a], Yi Liu [b,*]

Under revision in: Marine Structures,

[a] Ph.D candidate, Dalhousie University, Department of Civil and Resource Engineering, 1360 Barrington St., Halifax, NS, Canada B3J 1Z1., Email: vahid@dal.ca

[b, *] Corresponding author. Professor, Dalhousie University, Department of Civil and Resource Engineering, 1360 Barrington St., Halifax, NS, Canada B3J 1Z1, Email: yi.liu@dal.ca

5.1 Abstract

This paper investigated the effect of a 3D simulated metal inert gas (MIG) welding induced heat affected zone (HAZ), residual stress and distortion fields on the behaviour of aluminum stiffened plates under compressive loading. A two-step, thermo-structural finite element model was developed for the simulation of the welding process and the model was verified using the available experimental results. The welding induced HAZ, residual stress and distortion were then studied for tee-bar stiffened aluminum plates of various geometries. The effect of these welding induced imperfections on the load vs. shortening curves, buckling mode, and the post-buckling behaviour of each stiffened plate geometry were investigated. It was found that welding induced tensile and compressive residual stresses ranged from 72 to 77% and 18 to 36% of the base metal yield stress, respectively. The width of the HAZ around the weld line increased as the plate slenderness increased. The reduction in ultimate strength of the tee-bar aluminum stiffened plates due to the presence of the HAZ and residual stress was as much as 10% and 16.5% respectively. The assessment of the existing analytical methods revealed that they provide significant underestimation of the ultimate strength of aluminum stiffened plates when compared with the finite element results.

5.2 Introduction

Aluminum has been used to build ship structures since the mid-20th century with an increasing application in high-speed vessels in the past 20 years. In ship structures made of either steel or aluminum, stiffened panels, constructed through welding, are mainly used as ship hull girders and they are usually designed for axial compressive loads (Aalberg et al. 2001). While welding induced residual stress and distortion are common in both aluminum and steel stiffened plates, the heat affected zone (HAZ) where the material strength sustains marked reduction due to welding is unique in aluminum stiffened plates. Analytical and experimental research showed that for aluminum stiffened panels, welding induced residual stresses and distortions, and yield strength reduction in the HAZ have substantial effects on the ultimate strength (Zha and Moan 2001, Rigo et al. 2003). Finite element studies by Rigo et al. (2003) showed that the effect of HAZ led to a 0 to 30% reduction on ultimate strength of angle-bar stiffened plates depending on their column slenderness. The reduction was minimal for high column slenderness, but increasingly significant as the stiffened plates became stockier. However, the slenderness typical of naval structures was not thoroughly studied. A numerical study conducted by Zha and Moan (2001) showed that the reduction of the ultimate strength due to the presence of HAZ was about 15% for AA6082-T6 and 10% for AA5083-H116 in flat-bar aluminum stiffened plates that were designed to fail by torsional buckling of stiffeners. Their parametric study revealed that over 90% of the reduction of ultimate strength was introduced by the presence of the transverse HAZ in nearby endplates. Their models were designed to buckle by the stiffener tripping mode; other models with other buckling modes were not included in the study. It should be pointed out that all aforementioned studies did not model the welding

process and instead, constant HAZ widths were assumed in the finite element modeling regardless of the material thickness and welding parameters. In terms of residual stress, Zha and Moan (2001) and Rigo et al. (2003) found that the maximum reduction in ultimate strength due to the presence of residual stresses was about 7% and 5%, respectively while the Ship Structure Committee (SSC-460, 2011) simply neglected the presence of residual stresses in the finite element modeling.

One major study on aluminum stiffened plates was conducted by Paik et al. (2007) where 78 full-scale prototype aluminum stiffened structures constructed by metal inert gas (MIG) welding were tested under compression, which was followed by a finite element study. Using experimental results, the welding induced residual stresses, distortions and HAZ were approximated and categorized in three levels of "slight", "average", and "severe". In the subsequent finite element study, they used one shell element representing the HAZ in the plate and stiffener. The welding process was not directly modeled but simplified average values of residual stresses, HAZ and distortions were assumed in the modeling. However, discrepancies between their experimental and finite element results were observed. Based on the regression analysis of the experimental and numerical results, they developed closed-form empirical ultimate limit state formulas for aluminum stiffened plates. For tee-bar aluminum stiffened plates the ultimate strength was expressed as in Eqn (5.1):

$$\frac{\sigma_u}{\sigma_Y} = \frac{1}{\sqrt{1.318 + 2.759\lambda^2 + 0.185\beta^2 - 0.177\lambda^2\beta^2 + 1.003\lambda^4}} \le \frac{1}{\lambda^2} \qquad (5.1)$$

where σ_u is the ultimate strength of the tee-bar aluminum stiffened plate, σ_Y is the yield stress of the aluminum, and β and λ are plate slenderness and column slenderness of the stiffened plate respectively.

Although there are methods by IACS (2009) and Gordo and Soares (1993) which can be used to determine the ultimate strength taking into account the welding induced residual stresses for steel stiffened plates (Gannon, 2011), whether they can be directly applied for aluminum stiffened plates remains a question due to the presence of HAZ. Two marine classification society rules, the DNV Rules for Classification of High Speed, Light Craft and Naval Surface Craft (2013) and the ABS Guide for Building and Classing High Speed Naval Craft (ABS 2007) apply an overall strength reduction to the yield stresses in the structure to account for HAZ and thus ignore the effect of HAZ on the buckling mode of the structure. While this makes design simpler, the penalty is presumably a heavier and more conservative structure. The Ship Structure Committee (SSC-460, 2011) suggested that the strength penalty for modeling the stiffened panel as all-HAZ material in place of a combined base/HAZ material model ranged from 10% to 30%. It recommended that modeling aluminum stiffened panels should explicitly consider the HAZ extent, location, and strength in place of applying a uniform reduction factor to the strength of the HAZ material.

In light of the above, this research was motivated to accurately characterize the welding-induced imperfections including residual stress and distortion fields as well as the HAZ in aluminum stiffened plates constructed by metal inert gas welding, and to evaluate the influence of these imperfections on the strength and behaviour of aluminum stiffened

plates. Tee-bar stiffened plates with varying plate and column slenderness were considered in this study. A three-dimensional, two-step thermal-structural finite element model was developed to simulate the welding process and the model was verified with available experimental results. The model was then used to obtain aforementioned welding induced imperfections and generate the load vs. shortening curves of the aluminum stiffened plates under the compressive loading for each geometry. The effect of welding induced imperfections on the ultimate strength, buckling mode and post-buckling behaviour of the aluminum stiffened plates were presented and discussed.

5.3 Numerical simulation

5.3.1 General

In this study, the ANSYS program was used in the two-step thermal-structural nonlinear analysis. In the thermal analysis, the model was meshed with thermal elements and the time-dependent temperature distribution due to the moving heat source was obtained. In the subsequent structural analysis, the temperature field time history calculated from the thermal analysis was applied to the model as a series of thermal loads, where each load step represented an increment in the position of the traveling heat source along the weld path. The structural analysis of the model provided the residual stresses and distortions induced by the welding heat source.

The model consisted of a tee-stiffener and plate assembly with transverse frame plates welded at each end. A schematic view of the model is shown in Figure 5.1. All

materials were made of AA5083-H116, which is widely used in aluminum high speed vessels. The stiffener was connected to the plate by fillet welds deposited on both sides of the stiffener. The transverse frames were also joined to the stiffener and plate by fillet welds. The stiffener was initially attached to the plate by 10 mm long tack welds placed at both ends as well as in the mid-length of both sides of the stiffener shown as dotted lines in Figure 5.1. The tack welds were also employed on both ends of the transverse frame plates. The welding sequence is shown in Figure 5.1. After each of the first and second weld line, the stiffened plate was allowed to cool down for 30 minutes, and after each transverse weld line, the stiffened plate was allowed to cool down for 1 minute. After the welding of all the weld lines was complete, the model was allowed to cool down to the room temperature. It is assumed in this study that a matching filler metal was used.

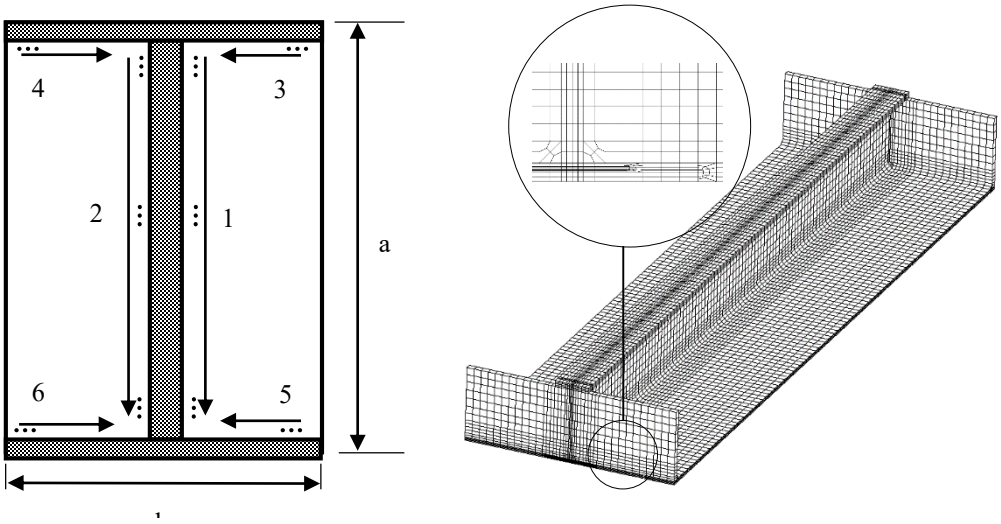

Figure 5.1 Model setup and welding sequence

5.3.2 Meshing and boundary conditions

The finite element meshing pattern for both the thermal and structural models were the same but with different elements. For thermal analysis SOLID70 thermal element was used. The element has eight nodes with a single degree of freedom, temperature, at each node. Its equivalent structural element SOLID185 was used in the structural analysis. This element has eight nodes, each having three degrees of freedom: translations in the nodal x, y, and z directions. Finite element meshing of the model is shown in Figure 5.2. A relatively dense mesh through the thickness of the plate and stiffener was considered in regions near the weld line in order to accurately represent the temperature gradient. A mesh convergence study revealed that 12 elements were needed through the thickness of the plate in regions near the weld line. In the regions away from the weld line the number of elements through the thickness was reduced to increase the computing efficiency. A minimum of four elements was considered through the thickness of the plate away from the weld. The complete model contained approximately 50,000 elements.

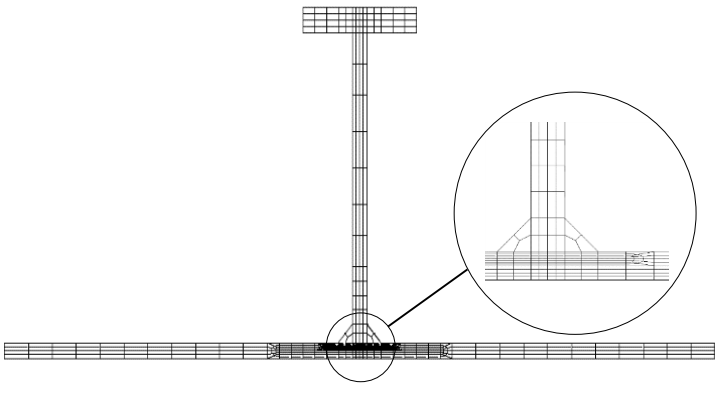

Figure 5.2 Finite element meshing of the model

The boundary conditions applied to the longitudinal edges of the plate were representative of the level of restraint in stiffened panels in ship hull girders. The longitudinal edges were restrained to remain straight when moving in the plane of the plating and free to move out of plane of the plating as suggested by Dow et al. (1981). This was achieved by restraining the rotation of the longitudinal edges about the longitudinal and vertical axis (Gannon et al., 2012). Simple support boundary conditions were applied to the ends of the stiffened plate where the centroid of one end was restrained for displacement in all three directions and the centroid of the other end was restrained for displacement in transverse and vertical directions.

5.3.3 Material model

Except for the material yield stress, all of the temperature dependent thermal and mechanical material properties for 5000 series of aluminum were adopted from Zhu and Chao (2002). The temperature dependent material yield stress was adopted from Eurocode 9 (1998). The temperature dependent heat transfer coefficient was adopted from Michaleries et al. (1997). A constant value of 0.33 was assumed for the Poisson's ratio through the temperature history. The temperature dependent thermal and mechanical material properties are shown in Figure 5.3.

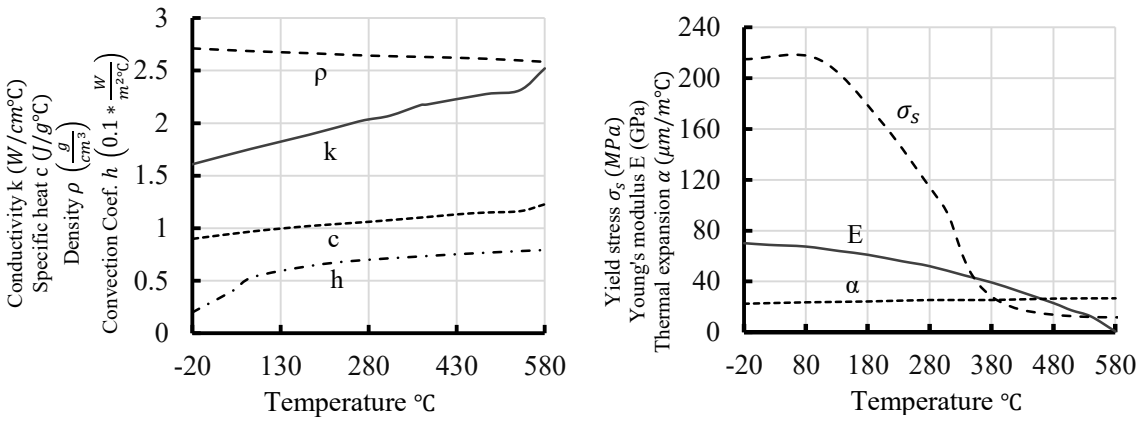

Figure 5.3 Temperature dependent material properties for AA5083-H116

A non-linear stress-strain relationship based on Ramberg-Osgood relation was used to model the AA5083-H116 material as shown in Eqn (5.2). Based on experimental data presented by Zha and Moan (2001), the 0.2% proof stress, σ_{02}, was taken as 215 MPa and the exponent, *n*, was taken as 14.

$$\varepsilon = \frac{\sigma}{E} + 0.002\left(\frac{\sigma}{\sigma_{0.2}}\right)^{n} \tag{5.2}$$

5.3.4 Heat source and thermal analysis

The heat input for the gas metal arc welding was divided into two parts. One was the volumetric heat from the molten metal droplets and the other was the surface heat flux from the welding arc. In this study it was assumed that 60% of the total heat was transferred to the work piece via the molten metal droplets and the remaining 40% was transferred by surface heat flux (Pardo & Weckman, 1989). In the surface heat source model, the angle of the torch was assumed to be normal to the surface of the weld. The heat of the molten

metal droplets was described using a volumetric heat generation rate with uniform density and for the heat flux a Gaussian distribution was assumed. The Gaussian distribution is defined relative to the coordinate system of the traveling heat source and it is expressed as:

$$q(x,\xi) = \frac{3Q}{\pi c^2} e^{-3x^2/c^2} e^{-3\xi^2/c^2} \tag{5.3}$$

where c is the arc radius of the welding arc. Figure 5.4 shows the thermal loads applied to a group of weld elements representing the deposition of the molten metal droplets on the work piece at the first thermal load step. In this figure the red elements represent the newly activated elements with prescribed heat generation rate and the arrows are the heat fluxes applied to the elements as nodal forces. Heat loss due to the combined effects of convection and radiation was accounted for by applying a temperature dependant heat transfer coefficient, shown in Figure 5.3, to all free surfaces of the model.

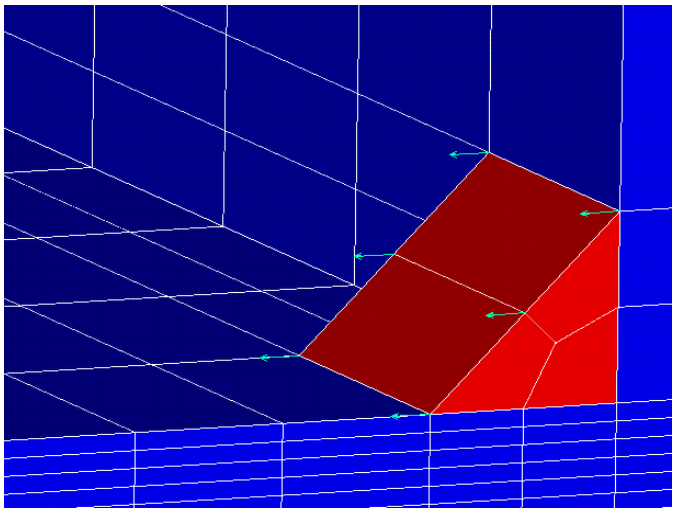

Figure 5.4 Heat input applied to the welding elements

5.3.5 Mechanical analysis

In the structural model, the coincidental nodes of the stiffener and plate at the interface of the plate and stiffener were connected using Combin39 nonlinear spring elements (Gannon et al., 2011). A high compressive stiffness and negligible tensile stiffness were assigned to these springs in the direction normal to the plate to prevent the penetration of the stiffener through the plate and allow the sliding and separation between the plate and stiffener.

In the structural analysis, the addition of the molten weld metal to the work piece was modelled using ANSYS element birth and death feature (Playdon and Simmonds 1984). In the beginning of the analysis all of the weld elements were deactivated (killed). As the heat source (torch) progressed, a user-defined subroutine was used to apply the calculated temperature field time history at the corresponding time and to query the average temperature of the weld elements. Those elements whose temperature had fallen below the solidification temperature were activated again simulating the deposition of the weld material on the work piece. The weld elements were activated with no strain history and their reference temperature was set to the solidification temperature to calculate the thermal strains. The calculated average nodal temperature of each element was then applied to that element as uniform body force replacing the nodal temperatures of the element. The application of constant temperature to elements prevented the excessive element distortion in areas with high temperature gradient and enhanced the solution convergence.

5.3.6 Development of HAZ

The development of HAZ due to the welding heat input was simulated based on the maximum temperature the elements experienced during the welding process. Three zones with different material strengths were defined, i.e., HAZ, semi-HAZ, and base metal zone. The correlation between the strength in these zones and temperature is summarized in Table 5.1. In the finite element analysis of both the FSW and MIG welding processes, as welding progressed the average temperature of elements were queried and the material properties of those elements were changed corresponding to maximum temperature according to Table 5.1. This method is consistent with the finding of Sato et al. (1999) and Terasaki and Akiyama (2003) where it was shown that the aluminum reached its minimum hardness in the areas that experienced a temperature above the 300 ºC to 325 ºC during the welding, and the areas that experienced a temperature between 200 ºC and 300 ºC obtained a hardness in between of the minimum hardness and the base metal hardness.

Table 5.1 Material strength with respect to temperature

	Temperature T	% of yield stress of base metal
HAZ	$T \geq 300$ ºC	67
Semi-HAZ	200 ºC $\leq T <$ 300 ºC	84
Base metal zone	$T <$ 200 ºC	100

5.4 Verification of the model

A literature survey yielded scarce experimental results on the welding induced residual stress and distortions in aluminum stiffened plates. In this study, the capability of the developed finite element model in simulating the temperature field, residual stress and distortions in aluminum plates was verified using experimental results obtained by Masubuchi (1980). In simulation of the fillet welding process in stiffened plates, the contact condition between the plate and the stiffener during the welding process is a critical aspect of simulation. In this study, the capability of the model in simulating this contact condition was verified using the experimental results of Deng et al. (2007a, b) on steel stiffened plates.

The specimen geometry and welding setup used by Masubuchi (1980) is shown in Figure 5.5. The plate was 12.5 mm thick and made of AA 5052-H32. The upper longitudinal edge of the plate was welded by metal inert gas welding (MIG).

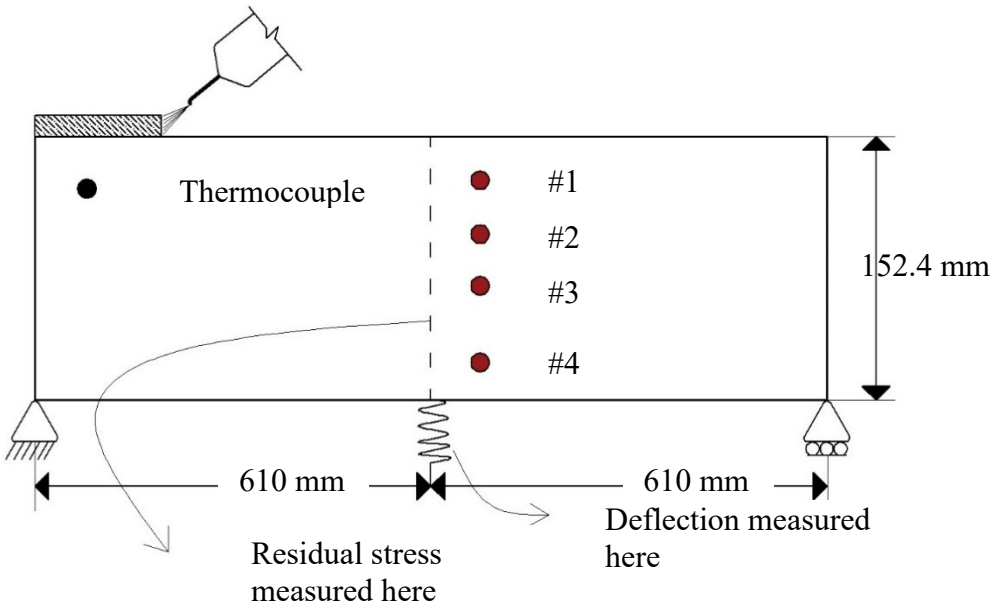

Figure 5.5 Test setup of Masubuchi (1980)

Figure 5.6 compares the temperature history whereas Figure 5.7 compares the transient vertical deflection and the longitudinal residual stresses, all at the mid-span of the plate. Both figures show that the finite element model provides reasonably accurate results in both temperature distribution and the resulted deformation and residual stress for welding in aluminum plates.

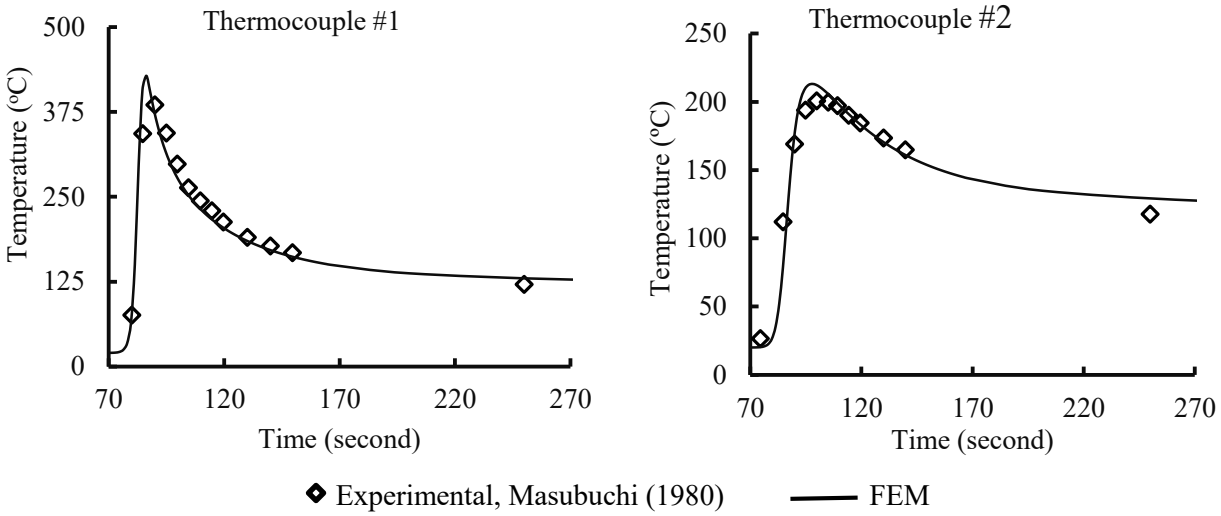

Figure 5.6 Comparison of temperature history at thermocouples

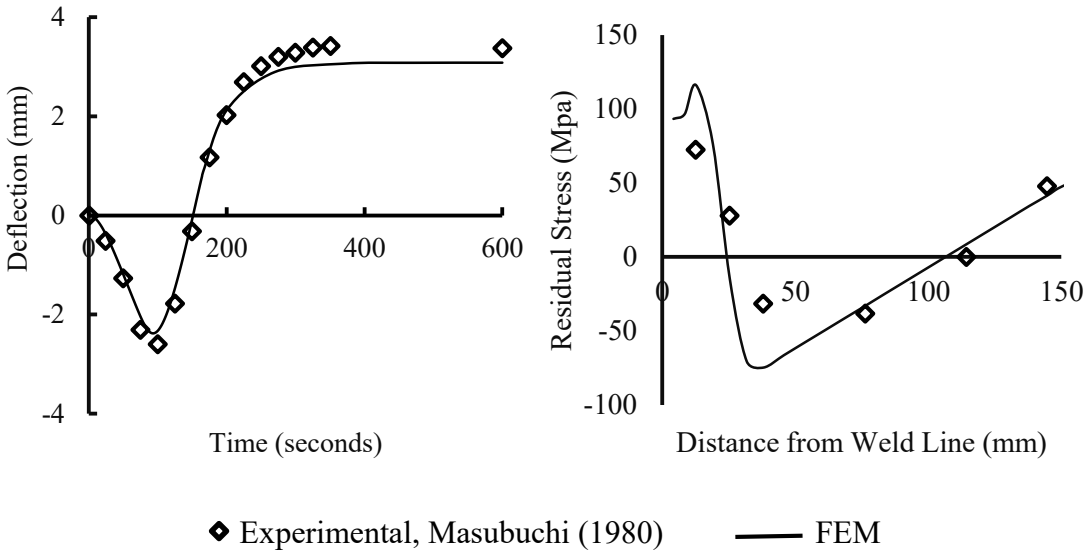

Figure 5.7 Comparison of transient vertical deflection and longitudinal residual stress at the middle of the plate

Experimental results obtained by Deng *et al.* (2007a) were for flat-bar stiffened plates made of SM400A steel. The plate was 500x500 mm and the stiffener was 500x300

mm, both having a thickness of 9 mm. Figure 5.8 shows the temperature time-history calculated by the developed model and the experimental results for points A and B located at the mid-span of the specimen. Figure 5.9 compares the vertical deflection of the plate at the mid-span of the specimen. Reasonably good agreement was observed in both figures. The residual stress distribution was not reported in the experimental study.

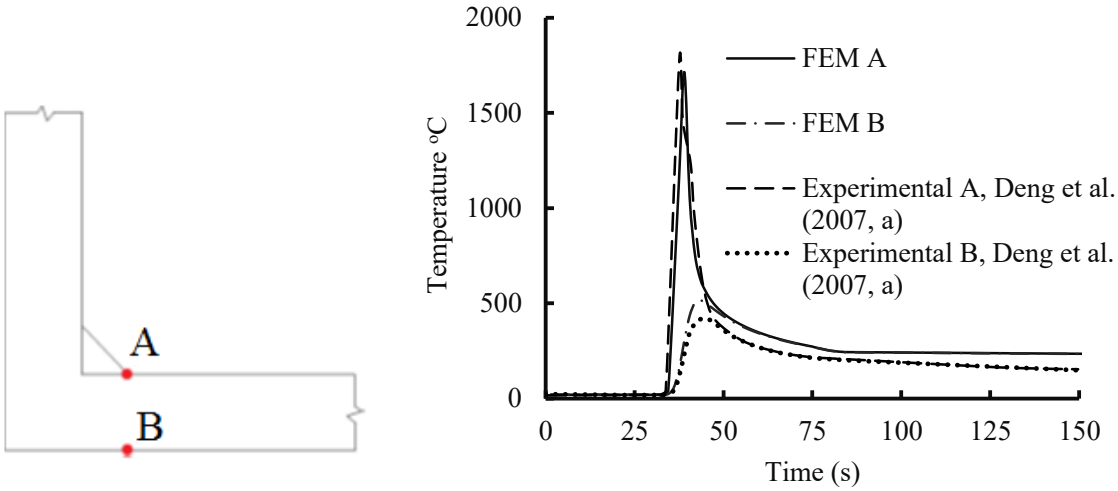

Figure 5.8 Comparison of finite element and experimental results on temperature time history

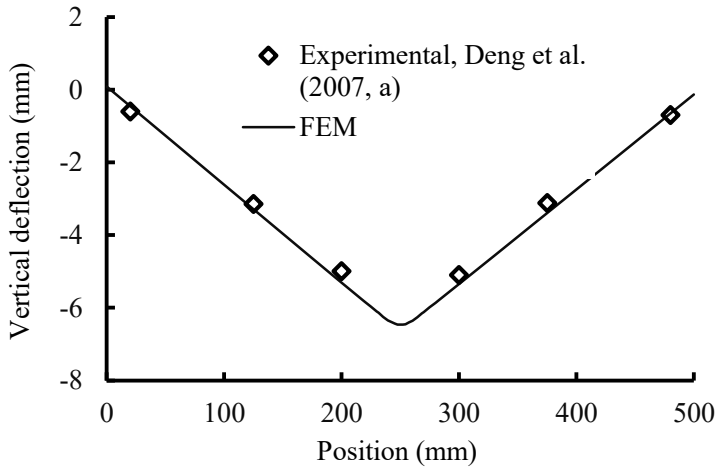

Figure 5.9 Comparison of finite element and experimental results on the vertical deflection at mid-span of the specimen

Both comparisons demonstrate that when time-dependent material properties for aluminum is implemented, the model is capable of simulating the welding of aluminum stiffened plates.

5.5 Parametric study

A parametric study was conducted to study the load vs. shortening behaviour of tee-bar stiffened aluminum plates under compressive axial loading. The welding-induced residual stress and distortion as well as the heat affected zone as described in the previous sections were considered. The load vs. shortening curves for each model were obtained using a displacement controlled analysis where an axial displacement at the centroid of one end of the stiffened plate was applied and the reaction at the centroid of the opposite end was calculated for each increment in displacement. Several stiffened plate geometries were

selected to cover a range of plate configurations. The non-dimensional geometric parameters of the plate to be varied were the plate slenderness β and column slenderness λ, given in Eqn (5.4) and (5.5) respectively:

$$\beta = \frac{b}{t}\sqrt{\sigma_y / E} \tag{5.4}$$

$$\lambda = \frac{a}{\pi r}\sqrt{\sigma_y / E} \tag{5.5}$$

where b, a, t, and r are the width, length, thickness and radius of gyration of the stiffened plate. σ_y, and E are the yield stress and the Young's modulus of the material respectively, which were taken as 215 MPa and 70 GPa for AA5083-H116. Four values of β (1.558, 2.078, 2.493, 3.325) were chosen to include a relatively wide range of plate slenderness, and for each β value, three values of λ were studied for short, intermediate and long column slenderness. Table 5.2 lists geometries of models with symbols defined in Figure 5.10. Fillet welds of 6 mm were used for the welding of the models. The welding current/voltage and speed used were in accordance with the American Welding Society's Guide for Aluminum Hull Welding (AWS D3.7, 2004).

Table 5.2 Details of tee-bar aluminum stiffened plate models (all dimensions in mm)

ID	*a*	*b*	t_p	h_w	t_w	b_f	t_f	t_t	β	λ
1	1000	225	8	100	6	45	8	8	1.558	0.441
2	1000	225	8	70	4	45	6	8	1.558	0.671
3	1000	225	8	50	4	45	6	8	1.558	0.916
4	1000	225	6	100	6	45	8	8	2.078	0.423
5	1000	225	6	70	4	45	6	8	2.078	0.631
6	1000	225	6	50	4	45	6	8	2.078	0.860
7	1000	225	5	100	6	45	8	8	2.493	0.415
8	1000	225	5	70	4	45	6	8	2.493	0.609
9	1000	225	5	50	4	45	6	8	2.493	0.829
10	1000	300	5	100	6	45	8	8	3.325	0.433
11	1000	300	5	80	4	45	6	8	3.325	0.574
12	1000	300	5	50	4	45	6	8	3.325	0.895

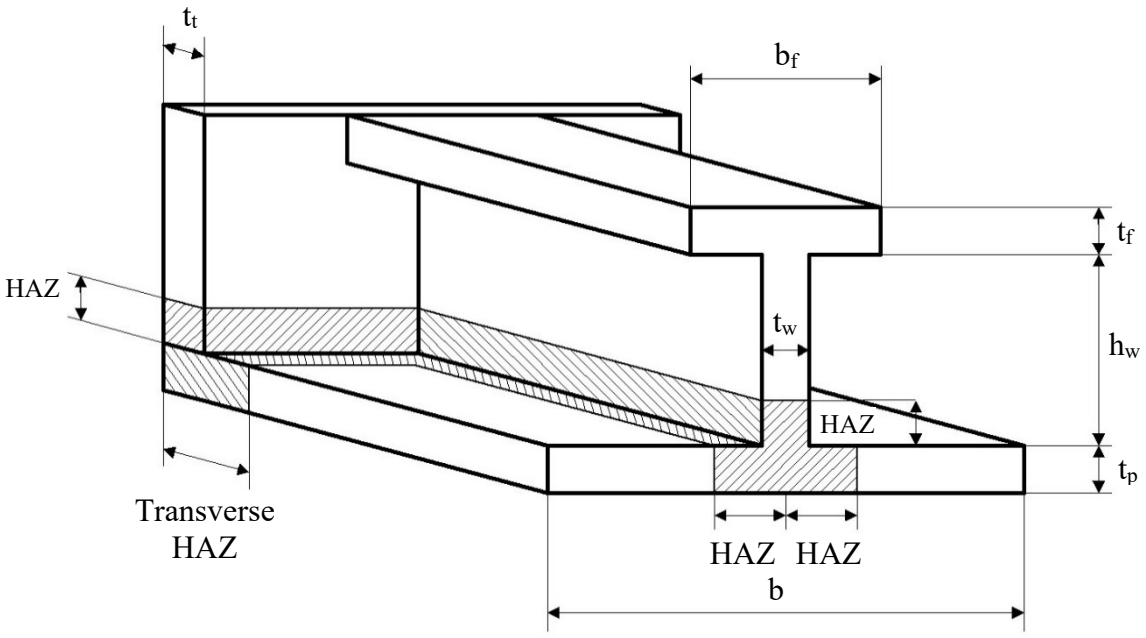

Figure 5.10 Tee-bar stiffened plate dimensions

5.6 Welding induced residual stress and HAZ

It is commonly known that the transverse residual stress is considerably smaller than the longitudinal residual stress and thus the latter is considered more influential in design. Welding induced longitudinal residual stresses obtained at the mid-thickness in the mid-length of the models are shown in Figure 5.11 for the plate and in Figure 5.12 for the stiffener. Table 5.3 summarises the maximum residual stress values shown in the figures.

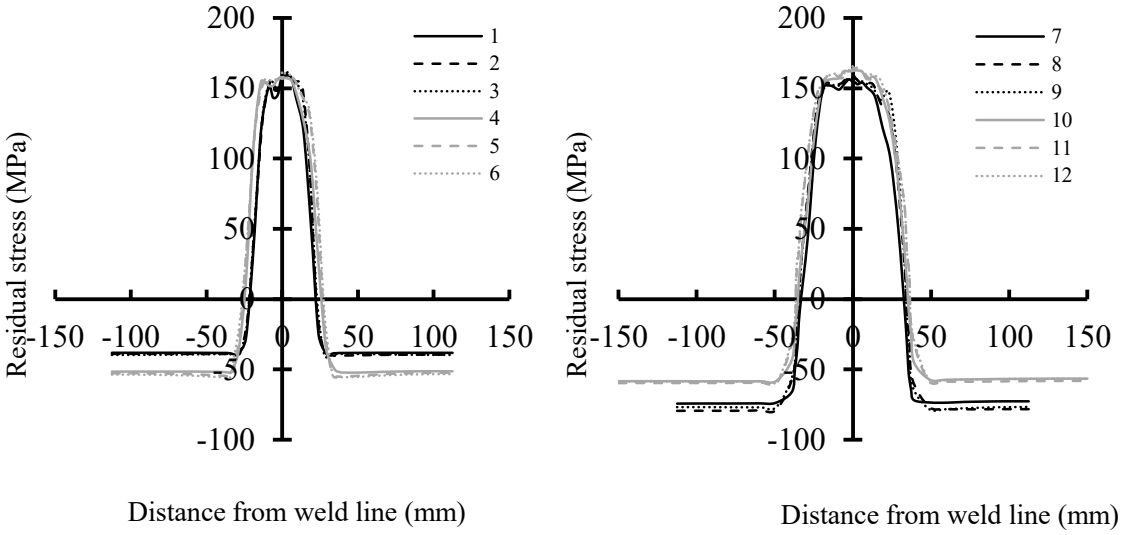

Figure 5.11 Longitudinal residual stress at the mid-thickness of the plate

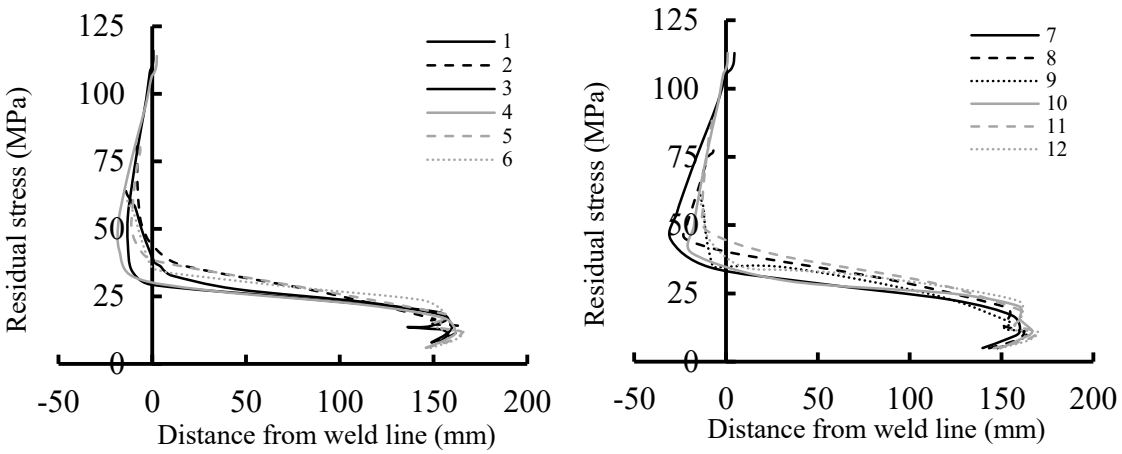

(a) (b)

Figure 5.12 Longitudinal residual stress at the mid-thickness of the stiffener

Table 5.3 Summary of finite element results for plates and stiffeners

ID	β	λ	Plate					Stiffener		
			Max. tensile stress (MPa)	Max. comp. stress (MPa)	Tensile zone width (mm)	Longit. HAZ width (mm)	Trans. HAZ width (mm)	Max. tensile stress (MPa)	Max. comp. stress (MPa)	HAZ height (mm)
1	1.558	0.441	159	39	44	14	24	180	13	11
2	1.558	0.671	162	40	46	13	24	180	9	16
3	1.558	0.916	160	40	48	13	24	181	14	18
4	2.078	0.423	157	52	54	19	24	180	18	16
5	2.078	0.631	158	55	54	18	24	179	11	22
6	2.078	0.860	162	56	54	18	24	182	14	22
7	2.493	0.415	156	74	66	24	24	177	30	17
8	2.493	0.609	158	79	68	23	24	184	22	24
9	2.493	0.829	157	78	68	23	24	181	14	24
10	3.325	0.433	163	58	70	24	24	183	18	20
11	3.325	0.574	164	59	74	28	24	188	12	24
12	3.325	0.895	166	59	74	28	24	188	15	23

Overall, numerical results show that tensile residual stresses with a maximum value ranging from 156 to 166 MPa, equal to 72 to 77% of the yield stress, were present in the plate and they acted over a width ranging from 22 to 37 mm on either side of the weld line. There was a rapid transition in the residual stress from tension to compression. The magnitude of the plate compressive residual stress in all models ranged from 39 to 79 MPa, which were 18 to 36% of the yield stress. The results of this study is consistent with the "average" level of tensile residual stress values suggested by Paik et al. (2007).

Figure 5.11 shows that neither the plate slenderness β nor the column slenderness λ had any significant effect on the maximum tensile residual stresses in the plate. The maximum tensile residual stress averaged at 160 MPa with an overall CV of 2%. The effect of λ on the maximum compressive residual stress and the tensile stress width remained minimal. However, as the plate thickness decreased from 8 to 5 mm and the resulting plate slenderness β increased from 1.558 to 2.493, the increases in the maximum compressive residual stress and the tensile stress width were 72% and 61% respectively. For a given weld size and heat input, a thinner plate experiences high temperature during welding in a wider area around the weld line than a thicker plate. This results in a wider region for tensile residual stress which in turn would result in higher magnitude of the compressive residual stress to maintain the stress equilibrium. The comparison of model group 7, 8, 9 and group 10, 11, 12 suggests that the plate slenderness increase as a result of decrease in the plate thickness had more pronounced effect on the compressive residual stress than that due to the increase in the plate width.

The predicted residual stresses in the stiffener as plotted in Figure 5.12 indicate that, in general, the magnitude of the tensile residual stress developed in the stiffeners was higher than that of the plate. The magnitude of the tensile residual stresses varied from 177 to 188 MPa for all models which were about 82 to 87% of the yield stress of the AA5083-H116 material. However, the magnitude of the peak compressive residual stress, ranging from 9 to 30 MPa, was significantly lower than that of the plate.

The width of the predicted longitudinal HAZ where material experienced temperature above 300 ^{o}C during welding in the stiffeners and plates are also shown in Table 5.3. Note that as shown in Figure 5.10, the longitudinal HAZ width for the plate presented in the table is half the total width, measured from the weld line to the extent of HAZ on either side of the weld whereas the HAZ width for the stiffener is the total width. Both HAZs are in the longitudinal direction as a result of welding longitudinal stiffeners. For a given plate slenderness, the effect of column slenderness on HAZ width was negligible. However, as the plate slenderness β increased from 1.558 to 3.325, the HAZ width also showed a marked increase, from 13 to 28 mm. In particular, the HAZ width ranged from 18 to 28 mm in models having a plate thickness of 5 or 6 mm and for models having a plate thickness of 8 mm the HAZ width was about 13 to 14 mm. It should be pointed out that the HAZ also formed in the transverse direction since the model included transverse frames welded to the plate. The total HAZ width in the transverse direction was determined to be 24 mm measured from the edge of the transverse platefor all models.

It is noted that some existing studies adopt a constant value for HAZ width in plates measured from the weld line on either side of the weld. For example, Mazzolani (1995)

suggested a value of 25 mm whereas Specifications of BS8118 (1999) and Eurocode 9 (1999) suggested a value of 18 and 30 mm respectively for the aluminum plates with 6 mm thickness. Paik et al. (2007) suggested a value of 23 mm, for the "average" level of HAZ, regardless of the plate geometry. However, the results obtained in this study show that the HAZ width is dependent on the plate slenderness and for plates with a thickness of 6 mm and above, the value suggested by Paik et al. (2007) overestimates the HAZ width. For plate with a thickness of 5 mm, the above mentioned studies provide more or less reasonable estimates.

5.7 Welding induced distortion

Figure 5.13 shows the welding induced vertical distortion in the transverse direction in the mid-length of the stiffened plate. All models exhibited a "hungry horse" shape distortion which is typical of welded ship structures. For a given plate slenderness, an increase in the column slenderness resulted in an increase in the vertical distortion as seen in the comparison within each model group with a constant β. For a given column slenderness, the thinner the plates, the larger the distortion, as shown in the comparison of models 1, 4 and 7. It is also observed that for a given plate thickness, increasing the plate width decreased the vertical distortion of the plate as can be seen in the comparison of models 7 and 10. Overall, the maximum value of the vertical distortion at the mid-width of the plate was 2.5 mm and occurred in model 9. The maximum relative distortion between the mid-width of the plate and its edge was 1.4 mm and occurred in model 10.

Figure 5.14(a) shows the vertical distortion in the longitudinal direction at the mid-width of the stiffened plate. They showed a half-sine wave pattern for all models, which

was similar to experimental results for steel stiffened plates (Dow, 1991). A thin and long plate attained a greater distortion than its thicker and shorter counterparts. The maximum value of longitudinal distortion was around 2.5 mm. The welding induced lateral distortion measured at the top of the web of the stiffener for models 4 to 6 and 10 to 12 in the longitudinal direction of the plate are shown in Figure 5.14(b). All stiffeners exhibited a more or less sinusoidal distortion pattern and the magnitude of the distortion was negligible. The maximum lateral distortion of the stiffener occurred in the mid-length of model 11 which was less than 0.5 mm. For models 1 to 3 and 7 to 9, a similar trend was observed and thus were not plotted for clarity.

The Ship Structure Committee (SSC-460, 2011) assumed 2 mm of deflection for both the plate and stiffener regardless of the stiffened plate geometry in the finite element simulation of tee-bar aluminum stiffened plates. Results of this study show that the SSC-460 value is reasonable for the plates but conservative for the stiffeners. Paik et al. (2007) suggested a value of $0.0018a$ for the "average" level of the magnitude of maximum vertical deflection in the plate mid-width and a relative distortion of $0.096\beta^2 t$ for the "average" level of the magnitude of the relative deflection between the plate mid-width and the plate edge. For the geometries considered in this study, these would result in a maximum distortion of 1.8 mm for the plate mid-width, and a maximum relative distortion of 2 to 5 mm between the plate mid-thickness and its edge. They also suggested a magnitude of 0.001a for the "average" level of maximum sideways distortion of stiffeners which results in 1 mm of deflection. When compared with results from this study, the value for the maximum vertical deflection in the plate mid-width suggested by Paik et al. (2007) is in agreement while those suggested for the relative distortion of the plate and the sideway

distortion of the stiffener would be conservative. This might be a result of the different boundary conditions used in this study and the study of Paik et al. (2007). In this study the boundary conditions of the ship hull were simulated at the longitudinal edges, whereas the longitudinal edges in the study by Paik et al. (2007) were considered to be free.

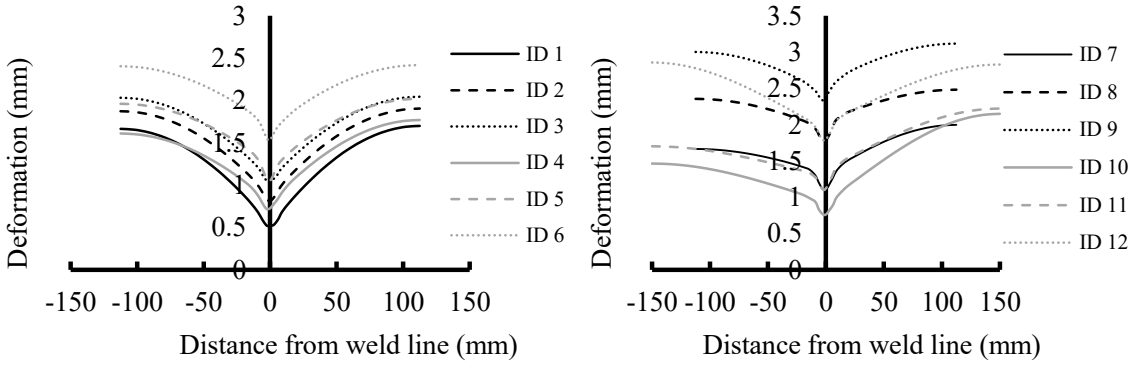

Figure 5.13 Vertical distortion of plate at mid-span

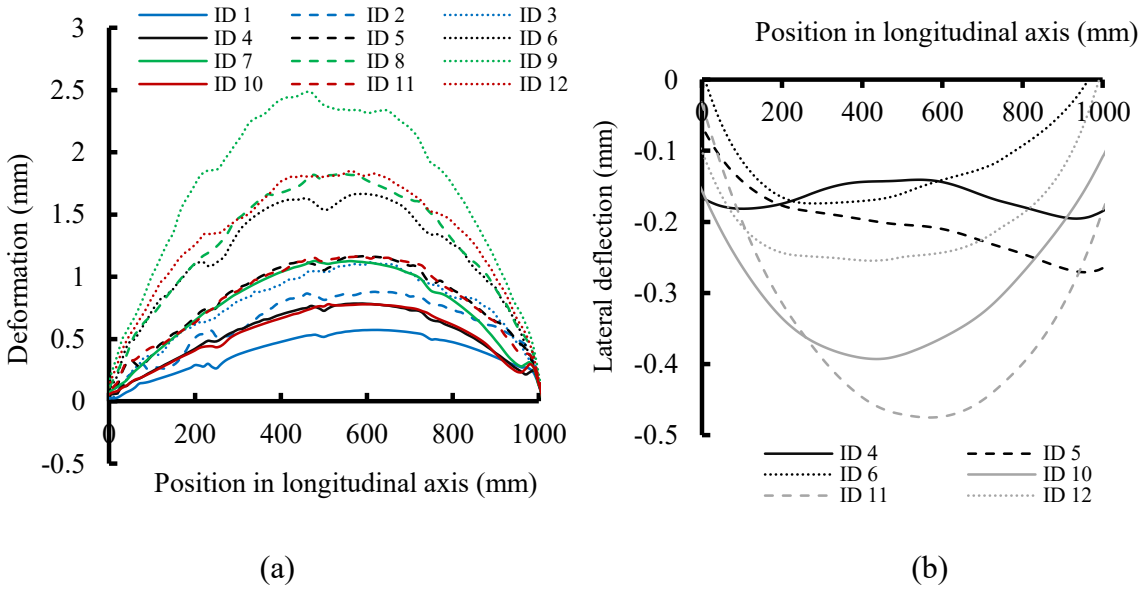

Figure 5.14 Distortions (a) stiffened plate vertical distortion along the longitudinal axis (b) lateral distortion of top of stiffener

5.8 Behaviour under compressive loading

The behaviour of aluminum stiffened plates under compressive loading was studied through load vs. shortening curves. Models were analyzed in three categories: [1] models with residual stresses and HAZ incorporated; [2] models without the HAZ but with residual stresses; and [3] models without residual stresses but with the HAZ. Note that the HAZ in these cases included both longitudinal and transverse HAZ. Table 5.4 provides the results for the ultimate strength and the buckling mode of each model analyzed in three categories. Also included in the table are the ultimate strength predicted using the analytical method provided by DNV Rules for Classification of High Speed, Light Craft and Naval Surface Craft (2013) and empirical formula (Eqn (5.1)) for aluminum stiffened plates suggested by Paik et al. (2007). In the case of DNV Rules [9] the ultimate strength was calculated once by using the yield stress of the base material and again by using the yield stress of the HAZ.

Table 5.4 Ultimate strength predictions and buckling modes

ID	β	λ	Normalized ultimate strength			Coll. mode	DNV with HAZ material [9]	DNV with base material [9]	Eqn. (1) Paik et al. [5]
			[1] With RS and HAZ	[2] With RS but without HAZ	[3] With HAZ but without RS				
1	1.558	0.441	0.845	0.848 (0.4%)	0.864 (2.2%)	IV	0.646 (-23%)	0.947 (+12%)	0.665 (-21%)
2	1.558	0.672	0.918	0.930 (1.3%)	0.940 (2.4%)	II	0.593 (-35%)	0.830 (-10%)	0.573 (-37%)
3	1.558	0.916	0.791	0.816 (3.2%)	0.795 (0.5%)	I	0.588 (-26%)	0.818 (+3%)	0.473 (-40%)
4	2.078	0.423	0.805	0.854 (6%)	0.889 (10.5%)	III	0.643 (-20%)	0.943 (+17%)	0.631 (-21%)
5	2.078	0.631	0.769	0.783 (2%)	0.871 (13.2%)	II	0.535 (-30%)	0.699 (-9%)	0.570 (-26%)
6	2.078	0.860	0.704	0.738 (4.7%)	0.767 (8.8%)	II	0.533 (-24%)	0.699 (-0.7%)	0.491 (-30%)
7	2.494	0.415	0.757	0.835 (10.2%)	0.837 (10.5%)	III	0.644 (-15%)	0.944 (+24%)	0.598 (-21%)
8	2.494	0.609	0.676	0.735 (8.7%)	0.786 (16.3%)	II	0.475 (-30%)	0.568 (-16%)	0.557 (-17%)
9	2.494	0.829	0.600	0.618 (3%)	0.687 (14.3%)	II	0.476 (-21%)	0.568 (-5%)	0.493 (-18%)
10	3.325	0.433	0.632	0.696 (10%)	0.628 (-0.5%)	III	0.644 (+2%)	0.944 (+49%)	0.530 (-16%)
11	3.325	0.574	0.571	0.625 (9.5%)	0.583 (2%)	II	0.325 (-43%)	0.325 (-43%)	0.517 (-9%)
12	3.325	0.895	0.480	0.503 (5%)	0.520 (8.5%)	II	0.324 (-32%)	0.326 (-32%)	0.463 (-3%)

Note: Values in the bracket were percentage increase/decrease compared with category [1] values

5.8.1 Failure mode

Four buckling modes were observed in the models. These were: I) beam-column type buckling; II) plate buckling; III) stiffener induced collapse by web buckling; and IV) stiffener induced collapse by tripping. As shown in Table 5.4, most models failed in the plate buckling mode (mode II) and stiffener induced collapse by web buckling (mode III). Examples of these buckling modes are shown in Figure 5.15. Models with greater stiffener height exhibited a stiffener induced collapse by the stiffener web buckling mode (mode III). This was usually accompanied by the buckling of the plate immediately after. As the stiffener height decreased, and consequently column slenderness λ increased, the models tended to fail in a plate buckling mode (mode II). Models 1 to 3 have the lowest plate

slenderness (< 2) but with stiffener geometries comparable to the other models. They exhibited failure modes that were not observed in models 4-12. Model 1 with the greatest stiffener height and lowest column slenderness λ among the three, failed by stiffener tripping, which is the least desirable due to its abrupt reduction in resistance beyond the ultimate load. As the column slenderness λ increased, the failure mode shifted to plate buckling as in model 2. A further increase in the column slenderness resulted in a failure mode change to beam-column buckling as in model 3.

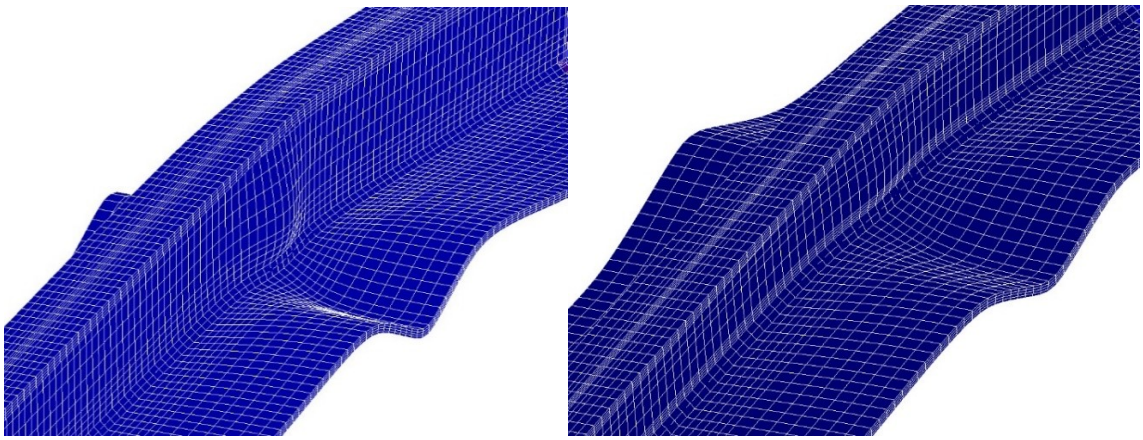

(a) (b)

Figure 5.15 Post ultimate deformed shapes (a) buckling mode III (Model 4); (b) buckling mode II (Model 5)

5.8.2 Ultimate strength

Figure 5.16 shows the finite element ultimate strength versus the plate slenderness, β. For category [1] models with both residual stress and HAZ incorporated, the ultimate strength decreased by as much as 47% as the plate slenderness increased from 1.558 to 3.325. It also shows that for a given plate slenderness, an increase in the column slenderness λ from 0.423 to 0.860 resulted in an average strength reduction of as high as 40%.

When compared with category [1] models, category [2] models where residual stress is incorporated but HAZ is ignored, show the overestimation in ultimate strength varying from 1 to 10% (shown in the bracket in Table 5.4) with the maximum averaged overestimation (8.2%) occurred in models with plate slenderness of 3.325. For category [3] models where the residual stress is ignored but HAZ is incorporated, the overestimation is around 0 to 16% with the maximum averaged overestimation (13.7%) occurred in models with plate slenderness of 2.493. It is also observed in both Table 5.4 and Figure 5.16 that when the plate slenderness is low (1.558), the effect of both HAZ and residual stress on the ultimate strength was small and as the plate slenderness increased, their effect on the ultimate strength reduction increased and reaching the maximum effect at slenderness of 3.325 and 2.493 respectively. The magnitude of the ultimate strength reduction as a result of HAZ is dependent on the width of the HAZ developed by each model. An increase in the plate slenderness resulted in an increase in the plate HAZ width which reached a maximum value at a plate slenderness of 3.325. Thus the maximum reduction in the ultimate strength occurred in the model group with a plate slenderness of 3.325. Table 5.4 shows that the magnitude of the reduction was also affected by the column

slenderness and the buckling mode. For a given plate slenderness, the model with the lowest column slenderness and failing by stiffener induced web buckling (mode III), had the highest reduction in ultimate strength due to the presence of the HAZ. In terms of the residual stress effect on the ultimate strength reduction, the magnitude of the residual compressive stress is believed to be a main contributor. The magnitude of the compressive residual stress reached a maximum at a plate slenderness of 2.494 where the highest reduction in the ultimate strength in the order of 10.5 to 16.5% was observed. This is consistent with the findings of Faulkner (1975) and Gannon et al. (2011) on steel stiffened plates where the effect of residual stress on the ultimate strength was found to reach a maximum at a certain plate slenderness. In those studies, the maximum ultimate strength reduction due to residual stress was observed to occur for plate slenderness of 2.5 and 1.9, respectively.

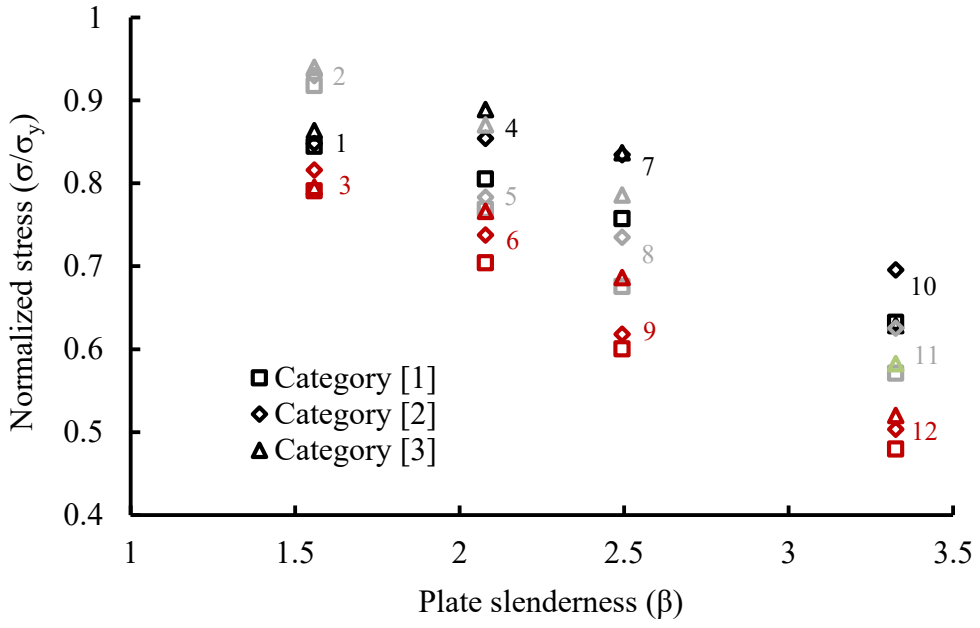

Figure 5.16 Variation in ultimate strength with plate slenderness

It is noted that both longitudinal and transverse HAZs were present in the model and thus both contributed to finite element strength values presented in the table. To investigate the effect of transverse HAZ on the ultimate strength of the aluminum stiffened plates, models 4, 7 and 10 were analyzed again with the residual stress and longitudinal HAZ but without transverse HAZ. The obtained results revealed that the transverse HAZ at the location of transverse frames was a primary contributor of the reduction in the ultimate strength. For models 4, 7, and 10, percentages of the total reduction caused by the transverse HAZ were 40, 85 and 87% respectively. It suggests that the higher the plate slenderness, the higher contribution of the transverse HAZ to the overall reduction due to HAZ.

The comparison of ultimate strength obtained using DNV Rules for Classification of High Speed, Light Craft and Naval Surface Craft (2013) for the presented failure mode and the finite element results of category [1] models shows that overall, when the HAZ material yield stress was used in the calculations, DNV underestimates the ultimate strength of the aluminum stiffened plates in the range of 15 to 43% (in bracket) with a mean of 27%. However, when the base material yield stress was used in the DNV calculations the results underestimated and overestimated the ultimate strength obtained by finite element analysis by as much as 43% and 49%, respectively, with an absolute average of 18%. The formula (Eqn (5.1)) for the ultimate strength developed by Paik et al. (2007) was shown to underestimate the finite element results in the range of 3 to 40% with a mean of 21%. It should be pointed out that this formula resulted in similar discrepancies in comparison with the experimental ultimate strength results obtained by Paik et al. (2007).

The underestimation of the ultimate strength calculated by DNV (2013) was mentioned by The Ship Structure Committee (SSC-460, 2011) and it was attributed to the approach in this design code regarding the consideration of the presence of HAZ where a blanket strength reduction is applied to the allowable stresses. The Ship Structure Committee (SSC-460, 2011) indicates that while this approach makes the design much simpler, the penalty is presumably a heavier more conservative structure. The discrepancies between the results of experimental and numerical methods and the results calculated by design codes were also observed by other researchers. Aalberg et al. (2001) compared their experimental results for the ultimate strength of aluminum stiffened plates with the results obtained from Eurocode 9 (1998). The results indicated that for "L" shaped aluminum stiffened plates with 1 m length, Eurocode 9 (1998) underestimates the ultimate strength by 35%. Zha and Moan (2001) also compared their numerical results with the results obtained by DNV (2013) and noted that "DNV gives very scattered values".

5.8.3 Load vs. shortening curves

The effect of HAZ on the load vs. shortening curves is examined by comparing category [1] and [2] models as shown in Figure 5.17 and the effect of residual stress is examined by comparing category [1] and [3] models as shown in Figure 5.18. In both figures, models 7 to 9 are used as examples.

Figure 5.17 shows that load vs. shortening responses were not significantly affected by the HAZ prior to buckling. Its effect was shown in the ultimate load and post-buckling region where a reduction as high as 10% and a considerably lower strength in the post buckling region were observed. A similar trend was observed for other models but with

different degrees of reduction. It should be pointed out that the obtained results are in line with the overall magnitude of the reduction in the ultimate strength due to the presence of HAZ recommended by SSC460 (2011) on the aluminum stiffened plates. However, this study provided more detailed results on the variation of reduction with respect to the plate slenderness and column slenderness of the stiffened plates.

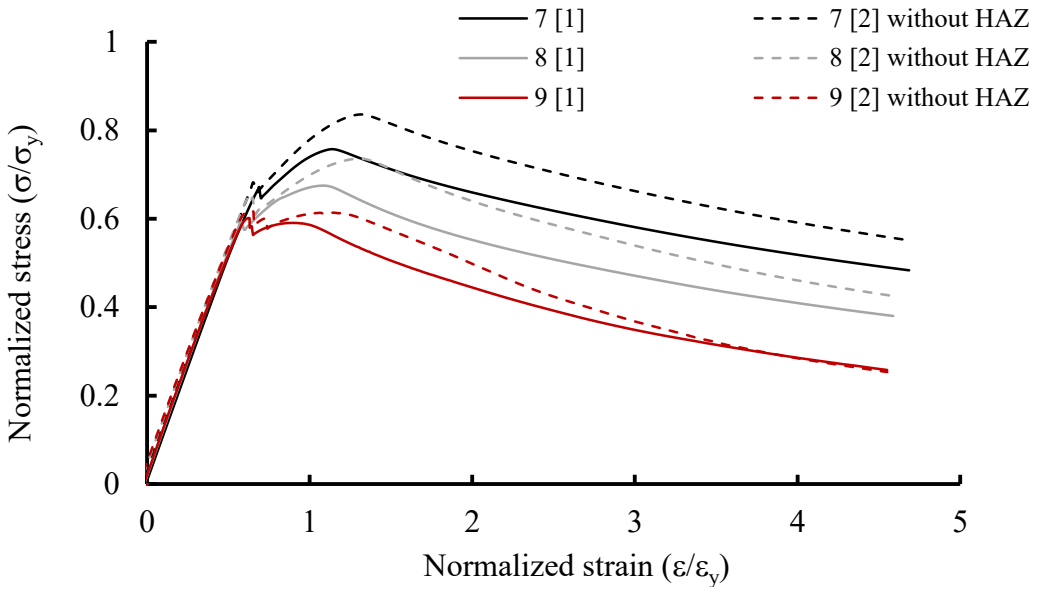

Figure 5.17 Comparing of load vs. shortening curves of category [1] and [2] models 7 through 9

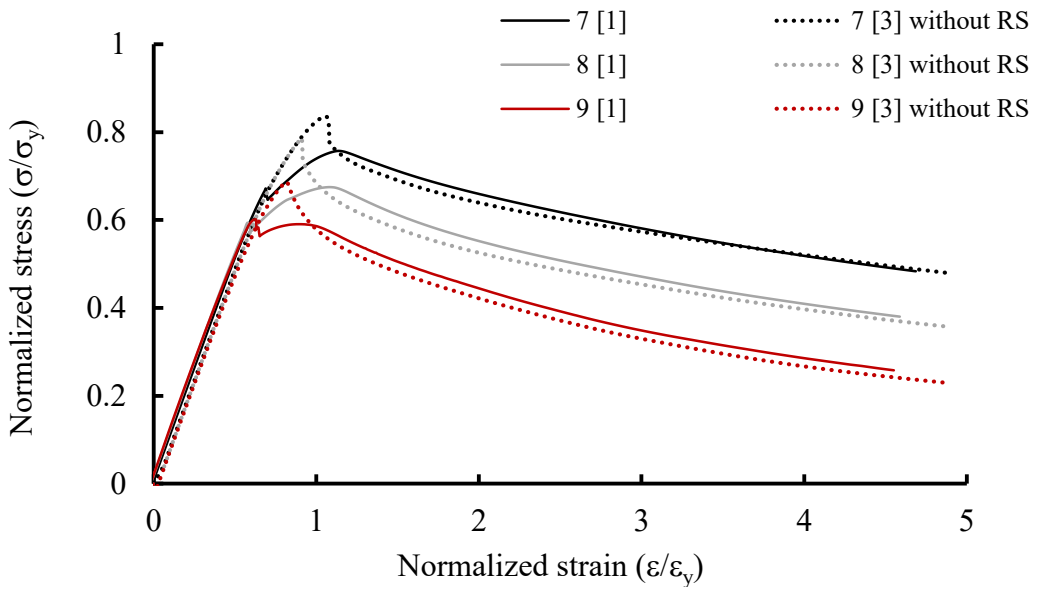

Figure 5.18 Comparing of load vs. shortening curves of category [1] and [3] models 7 through 9

In terms of the effect of residual stress, the load vs. shortening curves show that the presence of residual stresses caused a slight plateau in the curves near the ultimate load followed by a more gradual unloading portion compared with those models that did not include residual stresses. Those stiffened plates with no residual stress exhibited a more sudden and sharper drop in the load-carrying capacity after the ultimate strength was reached. The welding induced residual stresses only influenced the pre-buckling behaviour of the stiffened panels near the ultimate load. In the post-buckling part of the analysis, most models showed little difference whether or not residual stresses were included. These results are consistent with the behaviour of steel stiffened plates observed by Gordo and Guedes Soares (1993) and Gannon et al. (2012).

In contrast with other studies where the presence of the HAZ was assumed to be the main factor in the reduction of ultimate strength and the effect of residual stress was

negligible, the results of this study demonstrated that in several cases the influence of welding induced residual stress on the ultimate strength of aluminum stiffened plates can be more severe than that of the presence of HAZ. In addition, the magnitude of reduction due to the residual stress obtained in this study was significantly higher than that suggested by other studies (Zha and Moan 2001, Rigo et al. 2003).

5.9 Conclusions

A three-dimensional, two-step thermo-structural nonlinear finite element analysis was conducted to simulate the welding induced residual stress and distortion, and heat affected zone in tee-bar aluminum stiffened plates. The welding of the longitudinal stiffeners to the plate using metal inert gas welding as well as the welding of the transverse plates to the plate were simulated. Twelve tee-bar aluminum stiffened plates with various plate slenderness and column slenderness were considered in this study. The ultimate strength, buckling mode, post-buckling behaviour as affected by geometric properties as well as the welding induced residual stress, distortion and HAZ were studied. Some conclusions stemming from the study are as follows:

1. Maximum tensile residual stress developed in the plate due to welding ranged between 72 to 77% of the base metal yield stress while the compressive residual stresses ranged between 18 to 36% of the base metal yield stress. When compared with the column slenderness, the plate slenderness was shown to have a more significant influence on the distribution and magnitude of residual stress and HAZ. An increase in the plate slenderness resulted in an increase in residual stress and

the tensile stress width. The magnitude of the tensile residual stress developed in the stiffeners was higher than that of the plate. However, the magnitude of the peak compressive residual stress was significantly lower than that of the plate.

2. The total width of the HAZ of the plate in various models ranged between 26 to 56 mm depending on the thickness of the plate, with thinner plates having larger HAZ width. The height of the HAZ in the stiffeners was observed between 11 and 24 mm.
3. All models exhibited a “hungry horse” shape distortion in the transverse direction and the longitudinal distortions showed a half-sine wave pattern. For a given plate slenderness, an increase in the column slenderness resulted in an increase in the vertical distortion. For a given column slenderness, the thinner the plates, the larger the distortion. Overall, the maximum value of the vertical distortion of all models at the mid-width was around 2.5 mm.
4. For all geometries of tee-bar aluminum stiffened plates considered, the ultimate strength decreased due to the presence of the longitudinal and transverse HAZ by as much as 10%. The ultimate strength reduction due to the presence of the residual stresses was as much as 16.5%.
5. The comparison with the existing analytical methods shows that the DNV Rules (2013), on average, underestimated the ultimate strength of aluminum stiffened plates by as much as 48% with a mean of 27%, whereas the method developed by Paik et al. (2007) underestimated the finite element results in the range of 3 to 40% with a mean of 21%.

Chapter 6 - **Effect of clamping area and welding speed on the friction stir welding induced residual stresses**

Vahid Farajkhah [a], and Yi Liu [b,*]

Submitted for publication in: Ships and Offshore Structures,

[a] Ph.D candidate, Dalhousie University, Department of Civil and Resource Engineering, 1360 Barrington St., Halifax, NS, Canada B3J 1Z1., Email: vahid@dal.ca

[b, *] Corresponding author. Professor, Dalhousie University, Department of Civil and Resource Engineering, 1360 Barrington St., Halifax, NS, Canada B3J 1Z1, Email: yi.liu@dal.ca

6.1 Abstract

Effects of clamping area and welding speed on the development of residual stress fields in aluminum plates joined by the friction stir welding process were investigated in this paper. Friction stir welding on two aluminum alloy 6061-T6 plates was simulated in a three-dimensional, two-step thermo-mechanical analysis using the finite element program ANSYS. In the simulation, effects of welding tool plunging force, formation of heat affected zone and clamping fixture release were considered. The finite element results revealed that the clamping area plays a significant role on the formation and magnitude of friction welding induced residual stresses. The models with greater clamping areas showed a 40% lower maximum tensile residual stress in comparison with models with small clamping areas. Furthermore, for models with small clamping area, the effect of speed on the magnitude of residual stress was negligible. For models with large clamping area, the magnitude of maximum tensile residual stress was increased up to about 50% with an increase of welding speed.

6.2 Introduction

In recent years friction stir welding has gained an increasing popularity as an alternative to the conventional fusion welding processes, especially for materials sensitive to fusion welding such as aluminum alloys. Friction stir welding is an innovative solid-state joining process introduced by The Welding Institute (TWI) in the early nineties (Thomas et al., 1991). In a typical friction stir welding process, the workpieces are clamped firmly to a backing-plate to prevent the lateral movement during the joining process, and then a rotating cylindrical tool with a pin extending from its shoulder is slowly plunged into the conjunction of the workpieces until the shoulder is in contact with their top surfaces. The generated heat due to the friction between the tool and workpiece surface causes the workpiece to soften into a plasticized state without reaching the melting temperature of the material. As the tool progresses along the joining line, the plasticized material is stirred and forged to the other materials in the vicinity resulting in a solid state joint between the two workpieces. Since the friction stir welding takes place in the temperature below the material melting point, it reduces defects related to melting and re-solidification of the materials which are common in fusion welding and thus yields a fine microstructure, absence of cracking, and no loss of alloying elements (Zhu and Chao, 2004). In turn, the process is expected to result in a significantly lower residual stress and distortion.

One key characteristic of welding in aluminum plates is the formation of the heat affected zone (HAZ) around the weld line where the heat treated strength of aluminum is reduced to a significant degree. For 6000 series aluminum alloys, all the effects of heat treatment will be lost if the temperature reaches about 300 ^{o}C for only a short time (Davis,

1993; Beaulieu, 2006). After the cooling down period, the strength regained is minimal. Other values of the temperature for formation of HAZ on 6000 series aluminum alloys have been reported by Sato et al. (1999) and Terasaki and Akiyama (2003) which were 350°C and 325°C respectively. In addition to HAZ, some researchers further defined a semi-HAZ zone where the aluminum strength can be assumed somewhere in between the strength of HAZ and base material. Terasaki and Akiyama (2003) defined that the semi-HAZ formed in the areas that experienced a maximum temperature between 240°C and 325°C. Chao and Qi (1998) defined a semi-HAZ area where the material reached a temperature between 200°C and 300°C.

It is well known that the residual stresses due to welding can have a significant effect on the behaviour and integrity of the welded structure (Gannon et al., 2012) and this is also true for the friction stir welding. However, different values have been reported for the friction stir welding induced residual stresses. Some experimental studies showed that the tensile residual stress due to friction stir welding was about the yield stress of the base metal (Steuwer et al., 2006; Wang et al., 2000), while others showed that the residual stresses were substantially lower than the material yield stress (Dalle Donne, 2001; Webster, 2001; Sutton, 2002). Finite element modeling has also been used to simulate the friction stir welding process. Chao and Qi (1998, 1999) were among the first to conduct the finite element modeling of FSW. They developed a moving heat source model for FSW of 6061-T6 aluminum plates based on a reverse engineering method and studied the residual stresses caused by thermal effects. However, tooling geometry and plunging force from the welding tool to the workpieces were not modeled. Zhu and Chao (2004) developed a 3-D nonlinear thermo-mechanical finite element model to simulate the FSW

of 304L stainless steel plate taking into account the changes in the material strength of HAZ in the finite element simulation. However the plunging force was ignored in the simulation. Khandkar et al. (2004) used a coupled thermo-mechanical finite element model to simulate the transient temperature and residual stress in the FSW of aluminum alloys. Some general findings from the previous mentioned studies showed that the longitudinal residual stress is the predominant stress and the transverse residual stress is considerably smaller. The maximum longitudinal residual stress due to welding can range from 50% to full yield strength of the base material in aluminum plates. However, the development of HAZ as well as the plunging force were not considered in most previous studies. This was believed to attribute to the discrepancies reported in these studies between the finite element and experimental results.

This study was conducted to provide more information on the residual stress distribution in aluminum plates due to friction stir welding incorporating the effect of HAZ, mechanical force between the welding tool and the workpiece and clamp fixture release. Finite element modeling encoded using ANSYS software was used in this study. The modeling was carried out in a two-step thermal-structural coupled analysis to obtain the temperature history and residual stress distribution in AA6061-T6 aluminum plates. Two varying parameters selected in this study were the clamp area and welding tool traveling speed. They were selected since they can be easily adjusted in practice, and thus knowledge of their combined effect on residual stress can be of great value in an effort to optimize the FSW process with respect to residual stresses. Although there are several studies on the effect of welding speed on residual stress distribution (Riahi and Nazari, 2011; Feng et al, 2004; Lombard et al., 2009; Bastier et al, 2008), these studies only

considered the welding speed as an independent varying parameter. To the authors' best knowledge, there is no available literature examining the effect of clamping area in combination of welding speed on the residual stresses caused by FSW.

6.3 Numerical simulation

The finite element simulation of FSW process was completed in a two-step procedure using ANSYS. First, a thermal analysis was performed to obtain the transient temperature field during the welding. Secondly, the calculated temperature field as well as the tool plunging force were applied as a series of loads to the model, where each load step represented an increment in the position of the welding tool. A structural analysis was then performed to provide the residual stress distribution.

The same meshing patterns were used for both the thermal and structural analysis. For the thermal analysis SOLID70 thermal element was used, which is an eight-node element with temperature as the only one degree of freedom at each node. In the structural analysis SOLID185 structural element was used. This element has eight nodes with three degrees of freedom at each node: translations in the nodal x, y, and z directions. Temperature dependent thermal and mechanical material properties for AA6061-T6 were adopted from Riahi & Nazari (2011) and the temperature dependent heat transfer coefficient was adopted from Moraitis and Labeas (2008). These properties are shown in shown in Figure 6.1.

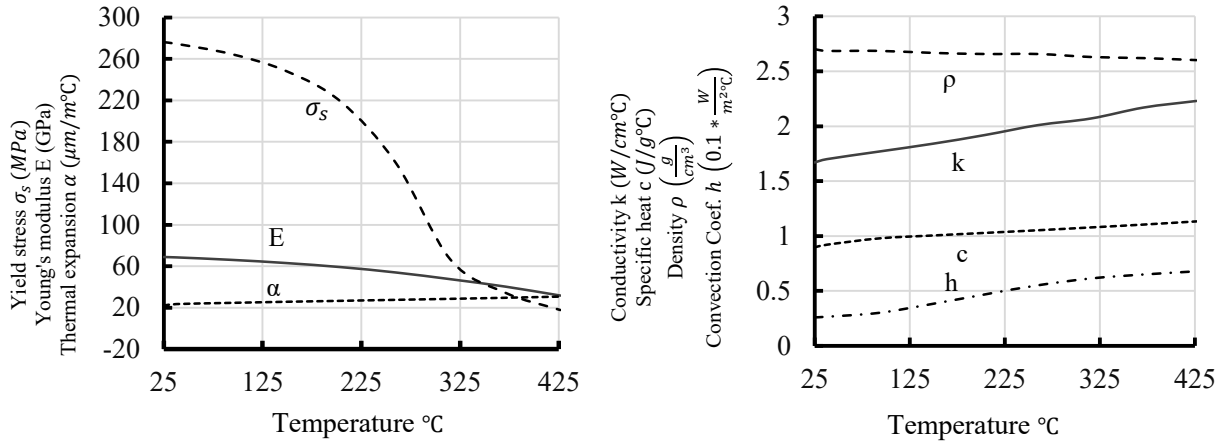

Figure 6.1 Temperature dependent material properties for aluminum alloy 6061-T6

A typical finite element meshing is shown in Figure 6.2. The highlighted areas (CW) in the figure represent the areas that were clamped down during the welding. After the welding was completed and the workpieces were cooled down to the ambient temperature, the clamps were released gradually allowing the redistribution of the residual stresses. The release of the clamps was considered in the last step of the structural analysis.

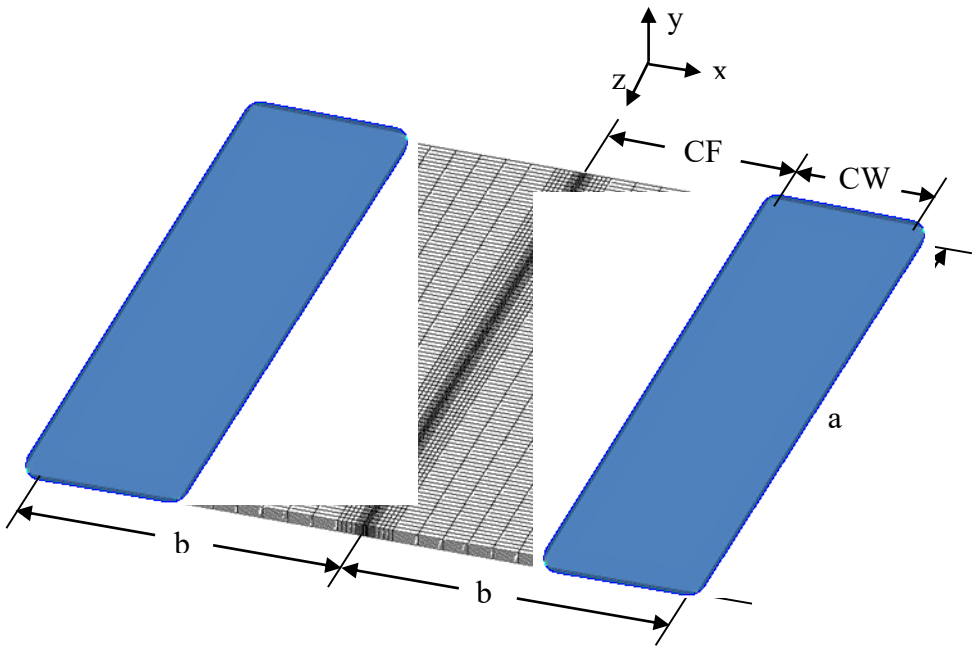

Figure 6.2 FSW finite element model mesh and boundary conditions

A key component of friction stir welding simulation is the modeling of heat generation. In this study it is assumed that the heat generated during welding is based on the contact conditions between the rotating tool and the workpiece surfaces using the method provided by Schmidt et al. (2004). In their method, the heat was assumed to be generated at three interfaces including the heat generated at the interface of the tool shoulder and the workpiece, $Q_{shoulder,}$, the heat generated by the side surface of the pin, $Q_{pin,side}$,, and heat generated by the tip of the pin, $Q_{pin,tip}$. The expressions of them are as follows:

$$Q_{shoulder} = \int_0^{2\pi} \int_{R_{pin}}^{R_{shoulder}} \omega \tau_{contact} r^2 (1 + \tan \alpha) dr d\theta \tag{6.1}$$

$$Q_{pin,side} = \int_0^{2\pi} \int_0^{h_{pin}} \omega \tau_{contact} R_{pin}{}^2 dz d\theta \tag{6.2}$$

$$Q_{pin,tip} = \int_0^{2\pi} \int_0^{r_{pin}} \omega \tau_{contact} r^2 dr d\theta \tag{6.3}$$

where ω is the angular velocity, r is the radius of shoulder, $\tau_{contact}$ is the shear stress in the surface, and α is the shoulder cone angle. Hence, the total heat generated in watts (W) by the friction stir welding Q_f, is the combination of the heat generated by the tool shoulder and tool pin:

$$Q_f = Q_{shoulder} + Q_{pin,side} + Q_{pin,tip} \tag{6.4}$$

This total generated heat was modeled as heat fluxes in the corresponding interface areas, moving with the welding speed. The heat distribution was assumed to be linear with respect to r, the distance between the tool centerline to the edge of the shoulder based on the assumption that the plunging force applied a uniform pressure to the workpiece. The heat fluxes were applied to the materials under the tool with a distribution given by Chao et al. (2003):

$$q(r) = \frac{3Q_f r}{2\pi R_{shoulder}^3} \tag{6.5}$$

where $R_{shoulder}$ is the outside radius of the shoulder of the tool and Q_f is the total heat input calculated using Eqn (6.4).

Heat loss from the free surfaces of the workpiece due to combined effects of convection and radiation was considered using a temperature dependent film coefficient

(Figure 6.1) on free surfaces of the workpiece (Moraitis and Labeas, 2008). The heat loss can be evaluated as:

$$q_s = \beta(T - T_0) + \varepsilon B(T^4 - T_0^4) \tag{6.6}$$

where T_0 is the room temperature, ε is the emissivity of the plate surface and B is the Stefan-Boltzmann constant which equals to $5.67 \times 10^{-8} Wm^{-2}k^{-4}$, and β is the heat transfer coefficient as given in Figure 6.1.

Since the bottom surface of the aluminum plates are in contact with the backing plate a higher convection coefficient is required. In the present study, the bottom surface of aluminum which is in contact with the backing plate is modeled as a convection condition with a higher convection coefficient and it is evaluated as:

$$Q_b = \beta_b(T - T_0) \tag{6.7}$$

where β_b is the convection coefficient between the workpiece surface and the backing plate and it is assumed to be $350\, W/m^2K$ based on the work of Chao et al. (2003).

The developed finite element model for thermal analysis was verified with experimental results of Guo et al. (2014) where a 6 mm thick AA6061 plate was welded to a 6 mm thick AA7075 plate using friction stir welding. The welding parameters including the tool geometry, rotational and travel speed, and the plunging force were provided by the authors so the heat input can be calculated using Eqn (6.4). Figure 6.3 shows the comparison of finite element and experimental temperature history at a location 10 mm away from the welded joint.

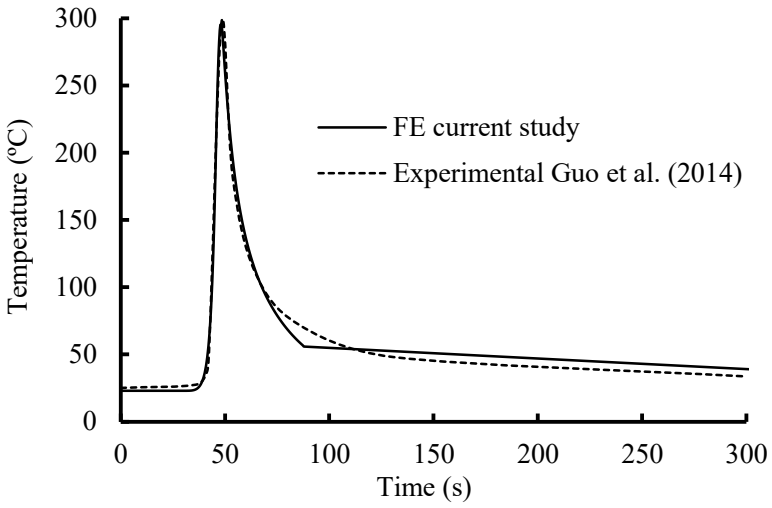

Figure 6.3 Comparison of temperature history profile at 10 mm away from the weld line

The thermal finite element model was also validated using the experimental results of Zhu and Chao (2004). The test setup of Zhu and Chao (2004) consisted of 3.18 mm thick plates of 304L stainless steel welded by FSW. The welding heat input was provided by Zhu and Chao (2004). Figure 6.4 compares the finite element and experimental results for the temperature distribution along the transverse direction of the workpiece.

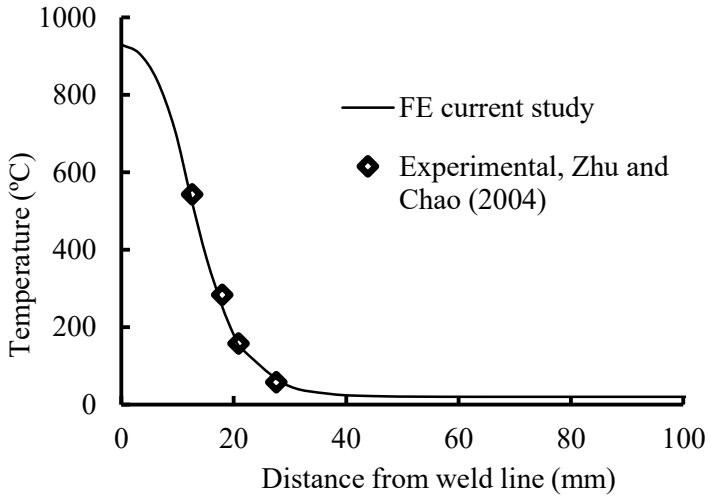

Figure 6.4 Comparison of temperature distribution along the transverse direction

A good agreement between the finite element and experimental results is obtained in both comparisons, indicating that the finite element is capable of simulating the temperature history and distribution with accuracy.

In the structural analysis, the material strength reduction due to formation of HAZ was simulated based on the maximum temperature the material experienced during the welding. This study adopted a similar approach by Chao and Qi (1998) to define three zones for material strength, i.e., HAZ, semi-HAZ, and base metal zone. The HAZ was defined as the region where the temperature exceeded 300^0C during welding and it was assigned to have 60% of the yield stress of the base metal. The semi-HAZ was identified as the region that reached a temperature between 200^0C and 300^0C and was assigned to have 80% yield stress of the base metal. Finally, the based metal zone was identified as the region with temperature below 200^0C and thus was assigned to have 100% yield stress of the base metal. In the finite element modeling of the welding process, as welding

progressed the average temperature of elements were queried and the material properties of those elements whose temperature had increased above 300^0C and 200^0C were changed to the material properties of HAZ and semi-HAZ respectively, simulating the formation of HAZ. Those whose temperature remained below 200^0C still assumed the properties of base metal.

In the mechanical modeling, two types of loading were assumed and they were the transient temperature history calculated in the thermal analysis step and the plunging force applied to the workpiece by the welding tool. As the welding progressed, a user-defined subroutine was used to apply the loads from the thermal analysis at the corresponding time, accompanied with the welding tool plunging force. This subroutine applied the loads to the model as a series of load steps where each load step represented an increment in the welding tool position. The plunging force, *P,* applied to the workpiece by the tool shoulder was modeled as a uniform pressure moving forward with the speed of welding and it is expressed as follows:

$$P = \frac{F}{A_{shoulder}} \tag{6.8}$$

where $A_{shoulder}$ is the area at the interface of the tool shoulder and the workpiece.

The structural analysis of the finite element model was verified again with the experimental results of Zhu & Chao (2004). The thermal results were compared in the last section. Figure 6.5 shows the longitudinal residual stresses on the cross-section in the mid-length of the workpiece obtained by the finite element model, before and after the release of the clamps. Note that the experimental results for the residual stresses before the clamps

release were not obtained. Also, the finite element simulation results obtained by Zhu & Chao (2004) are shown in the figure. The finite element developed in this study produced results comparable to those by Zhu & Chao (2004) but noticeably closer to the experimental results. It also shows that the welding induced residual stresses decrease significantly by the release of the clamps. It is concluded that the finite element model developed in this study can accurately simulate the residual stresses caused by the friction stir welding process.

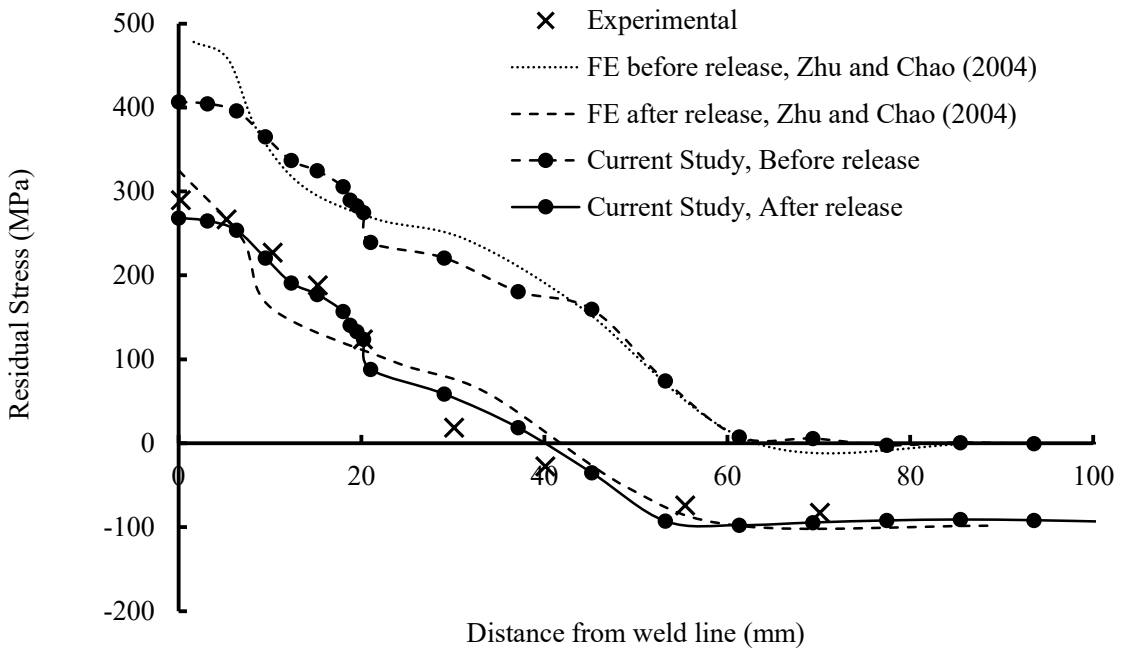

Figure 6.5 Longitudinal residual stress along the cross-section

6.4 Parametric study

Models of two plates being joined together by friction stir welding process were developed and the results on the temperature and residual stress distribution were compared for different clamping area and welding speed. The plates used were 6061-T6 aluminum alloy with 6 mm of thickness. Meshing and dimension symbols of the models are as shown in Figure 6.2. The plates were assumed to be supported on a backing plate and clamped down along their length. The clamped width is indicated by CW, and the unclamped width is indicated by CF as shown in the figure. A convergence study showed that four elements were necessary through the plate thickness. In the vicinity of the welding a relatively dense meshing was used in order to accurately represent the temperature and strain gradients. In the region away from the location of the weld, the temperature gradient was significantly lower and the mesh was then made less dense to reduce the number of nodes and thus the time required for solution.

The welding process details used in this study were adopted from the experimental tests of Guo et al. (2014) where 6 mm thick aluminum plates were joined together by friction stir welding with the following welding input parameters. The welding tool had a shoulder diameter of 15 mm and a pin diameter of 5 mm. The tool rotational speed was 1200 rpm with a plunging force of 6 kN. These welding parameters are considered as standard practice for friction stir welding on aluminum plates. Table 6.1 summarizes the models used in this study. Four values of CF, i.e., 50, 70, 90 and 125 mm were considered in the 250x500 mm plates, resulting CF/b ratios ranging from 0.2 to 0.5. The effect of plate width was considered using 100x500 mm plates (model 7 and 8) and in this case, one value of CF of 50 mm with CF/b =0.5 was considered. Two welding speeds of 5 and 10 mm/s

were considered in the 250x500 mm plates with CF values of 50 and 125 mm as well as the 100x500 mm model.

Table 6.1 Details of finite element models and friction stir welding parameters

Model No.	a (mm)	b (mm)	Welding Speed (mm/s)	CW (mm)	CF (mm)	CF/b
1	500	250	5	125	125	0.5
2	500	250	10	125	125	0.5
3	500	250	5	160	90	0.36
4	500	250	5	180	70	0.28
5	500	250	5	200	50	0.2
6	500	250	10	200	50	0.2
7	500	100	5	50	50	0.5
8	500	100	10	50	50	0.5

6.4.1 Thermal results

Figure 6.6 presents the simulated temperature distribution caused by FSW in the top surface of the cross-section at the mid-length of the plate for the 100x500 mm and 250x500 mm models. As can be seen, for a given weld speed, there is no noticeable difference in temperature distribution between the results of the 100x500 mm and 250x500 mm models when they were welded with the same welding parameters. For the speed of 5 mm/s the maximum temperature reached was about 477^0C and it was located at weld line in the top surface of the workpiece. This temperature value was about 130^0C less than the

melting temperature of aluminum alloy 6061-T6 and were within an acceptable range for FSW process (Chao and Qi, 1998; Riahi and Nazari, 2011). Figure 6.6 also shows that the area with a peak temperature of 300^0C or higher extended up to 9 mm away from the weld line. This area is considered as the HAZ formed by the FSW process. The figure also shows that increasing the welding speed decreased the maximum temperature and the HAZ width. The maximum temperature with a welding speed of 10 mm/s was 392^0C as opposed to 477^0C and the extent of the HAZ also decreased from 9 to 6 mm.

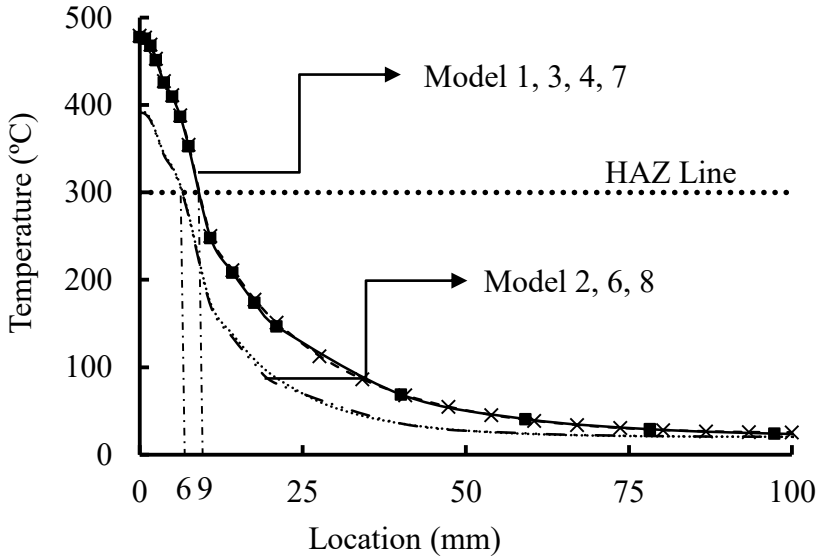

Figure 6.6 Temperature distributions along the transverse direction

6.4.2 Residual stress results

6.4.2.1 Effect of release of clamping fixture

After the welding was done and the workpieces were cooled down to the room temperature, the clamps were released. This resulted in the relaxation and redistribution of

the residual stresses. Figure 6.7 shows the longitudinal residual stress distribution at the mid-length of the workpiece before and after the release of the clamps for models 1, 5 and 7. It can be seen that there is a marked reduction in residual stresses after the release of the fixture and the degree of this reduction is associated with the extent of the clamping. The closer the clamping to the weld centerline, the more significant the reduction. For example, model 1 with a CF of 125 mm (CF/b = 0.5) showed a 10% reduction in the magnitude of residual stress in the welding centerline after the release of the clamping, and this reduction was about 36% for model 5 with a CF of 50 mm (CF/b= 0.2). For model 7 whose CF is 50 mm (CF/b = 0.5) but with a narrow plate width of 100mm, this reduction was about 22%. The comparison between model 1 and 7 shows that the CF extent rather than CF/b ratio is the deciding factor on the residual stress distribution. The reduction in the residual stress of the models with smaller CF extent can be attributed to the fact that clamping prevents the materials in the clamped area from undergoing deformation during the welding, and after the release of the clamps the strain energy stored in the area releases which leads to the relaxation of the material. The closer the clamps to the weld line, the more deformation being restrained during welding, and thus higher energy release and higher relaxation. The discrepancy between reduction rate of models 5 and 7 suggests that in addition to CF, plate width also plays an important role. For a constant CF, a shorter plate (model 7) resulted in less total area being restrained, which corresponded to less energy stored and thus less relaxation of the residual stresses. The above discussion shows that the fixture release in the friction stir welding must be considered in the numerical simulation of residual stress. For the following section, the friction stir welding induced residual stresses were reported after the models cooled down to the room temperature and the fixtures were released.

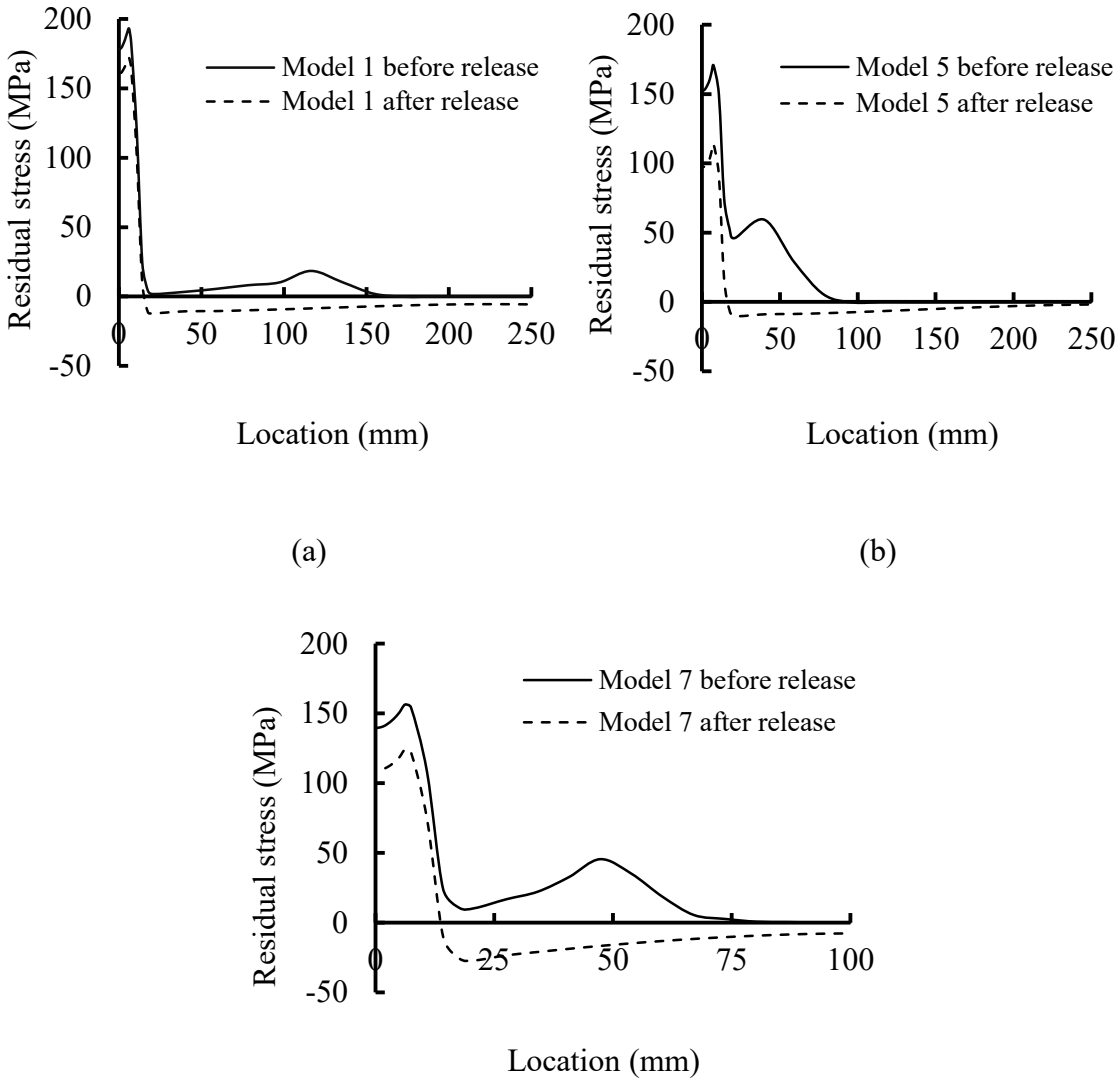

Figure 6.7 FSW induced longitudinal residual stress at mid-length cross section before and after the fixture release

6.4.2.2 Effect of clamping area

Figure 6.8 shows the variation of the longitudinal residual stresses obtained at the mid-thickness in the mid-length cross-section within 100 mm around the weld line. All models in this comparison have a constant welding speed but with varying clamping areas. As can be seen, the tensile residual stress zone for all models shows a double peak "M"

shape. For model 1, the developed tensile residual stress at the weld centerline was 160 MPa, which was about the yield stress of the material in the HAZ, and increased to 172 MPa at 7.5 mm away from the weld centerline. It should be pointed out that the two peaks were located almost on the edge of the welding tool shoulder, which also corresponded to the HAZ extent in this case. The double peak "M" shape of the longitudinal stress and also the location of the peaks are in line with other studies (Lombard et al., 2009; Bastier et al, 2008; Buffa et al., 2008). The tensile residual stresses were balanced with the compressive residual stresses away from the weld line. The maximum compressive residual stress in model 1 was 12 MPa at about 20 mm away from the weld line, and decreased to 5 MPa at the edges of the plate.

As shown in Figure 6.8, increasing the clamping extent significantly decreases the developed tensile residual stresses in the vicinity of the weld line. It seems that the largest values of tensile residual stress were obtained for the model with the largest CF and thus smallest clamping width. For the clamping extent studied, the reduction in the maximum tensile stresses was about 40%. The variation of maximum residual stress magnitude versus CF extent is further illustrated in Figure 6.9. It shows that the relationship between the CF extent and the maximum tensile residual stress is not linear. As the CF extent increased from 50 to 90 mm, the increase in the maximum residual stress was about 48% while a further increase in CF extent to 125 mm, the increase in the maximum residual stress was about 3%. It suggests that a further increase in CF extent may not result in significant increase in the residual stress. The variation in residual stress due to clamping extent can be contributed to the restraint that clamping exerts on the material. As discussed earlier, as the clamping area increases, the expansion and contraction of the materials due

to welding heat input is prevented in a wider area and thus the misfit between the expanded and contracted materials is reduced. Hence the materials exhibit lower residual stress before the release of the clamping, and after the clamping release the material experiences a higher residual stress reduction as shown in the previous section. The combined effect results in lower remaining residual stresses than that with smaller clamping area. It should be noted though that as seen in Figure 6.8, the clamping area does not have significant effect on the width of the tensile residual stress and the magnitude of compressive residual stress.

The effect of plate width on the developed residual stresses is shown through the comparison of model 5 (b = 250 mm) and 7 (b =100 mm) in both Figure 6.8 and Figure 6.9. Both models with CF=50 mm but with different plate width. The results revealed that a decrease in the plate width from 250 mm to 100 mm resulted in a 10% increase in the maximum residual stresses from 113 to 124 MPa as well as a significant increase in the maximum compressive residual stress from 10 to 26 MPa. Comparison of the model 1 and 7 in both figures shows much higher residual tensile stress for the former than the latter. Noting that both models have same CF/b of 0.5 but different CF extents, this again indicates that CF extent, rather than the ratio of CF/b is the important factor affecting the tensile residual stress.

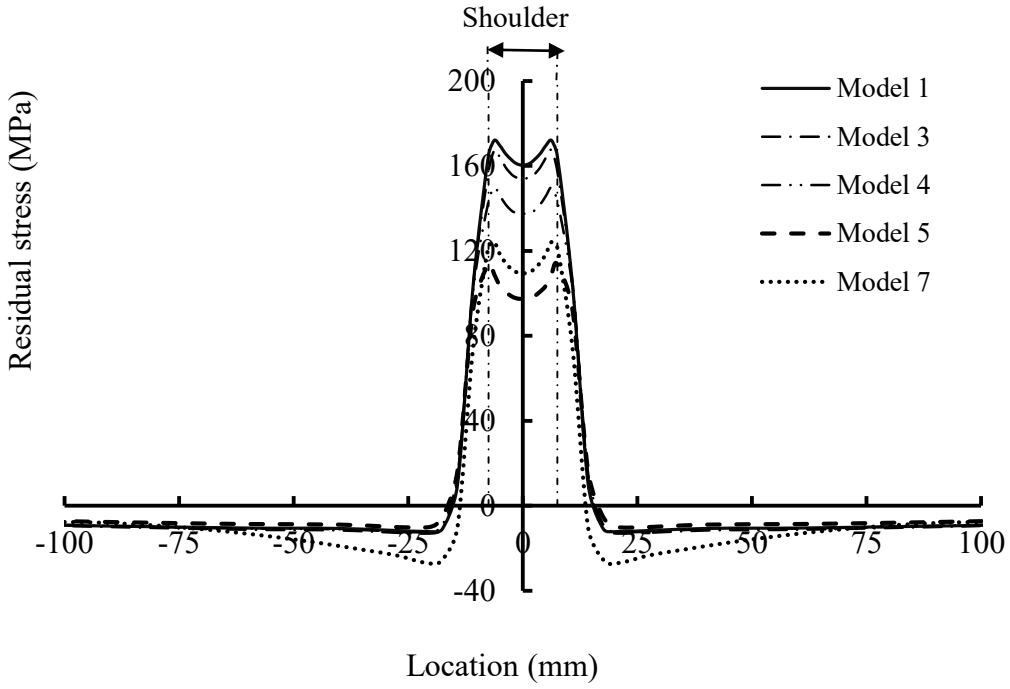

Figure 6.8 Effect of clamping and plate width on the FSW induced longitudinal residual stress

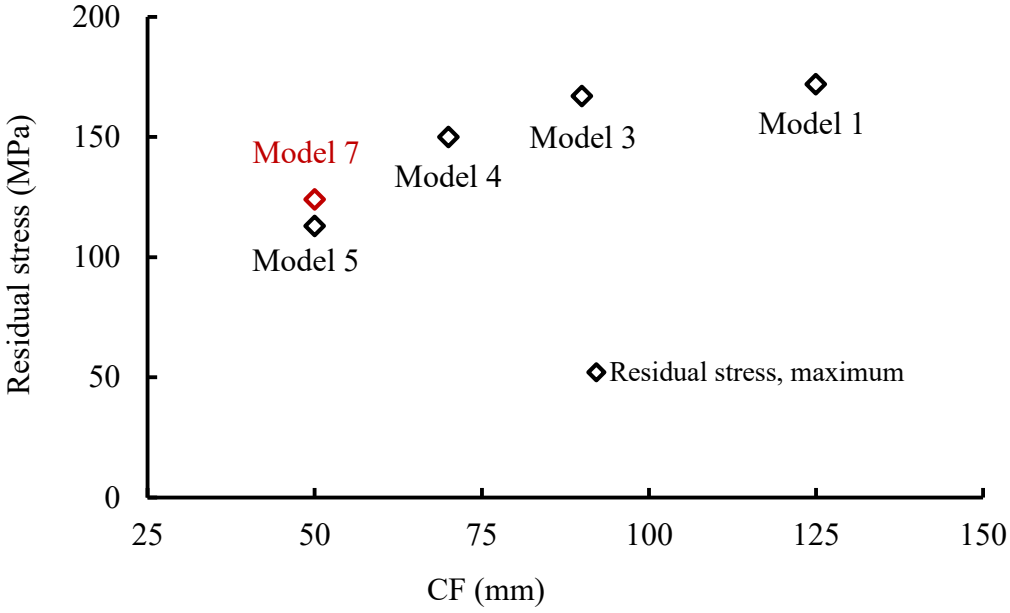

Figure 6.9 The CF extent versus maximum tensile residual stress

6.4.2.3 Effect of welding speed

Figure 6.10 shows the effect of welding speed on the residual stress in models with different plate width and clamping area. It shows that the effect of welding speed on the residual stress is dependent on the clamping area. In the case of Figure 6.10(a) where two models are of same plate width and CF of 125 mm, an increase in welding speed did not result in a significant change in the magnitude of the maximum tensile stress except that the tensile residual stress was distributed in a narrower region. In the case of Figure 6.10(b) and 6.10(c) where two models are of same plate width and CF of 50 mm, an increase in the welding speed resulted in a significant increase in the maximum tensile residual stresses, reaching the yield strength of the material in the HAZ and the distribution of the tensile stress was also in a narrower region. It can be concluded that regardless of the plate width, welding speed shows more pronounced effect on models with large clamping area than those with small clamping area. This is believed to be attributed to the difference in the resulted temperature distribution associated with the welding speed. It has been shown in Section 3.1 where the low welding speed resulted in a wider HAZ around the weld line than high welding speed. In the case of low welding speed, materials further away from the weld line experienced temperature increase which resulted in a greater softening area around the weld line and thus an increase in the width of the HAZ. Hence, in the cooling stage, the thermal contraction mismatch between the HAZ and adjacent material is reduced, resulting in an overall reduction in magnitude of the longitudinal residual stress but a wider tensile stress zone. On the other hand, high welding speed resulted in a narrower HAZ around the weld line, which led to greater difference in temperature between the HAZ and adjacent material and thus greater restraint exerted by the adjacent

material to the HAZ. This ultimately resulted in greater residual stress. In the case of comparison of model 1 and 2, the tensile residual stress already reached the yield stress of the material in HAZ, and therefore increasing the welding speed had no significant impact in the magnitude of the residual stresses. However, because of the fact that a narrower area experienced the high temperature gradient, the tensile residual stresses formed in a narrower area.

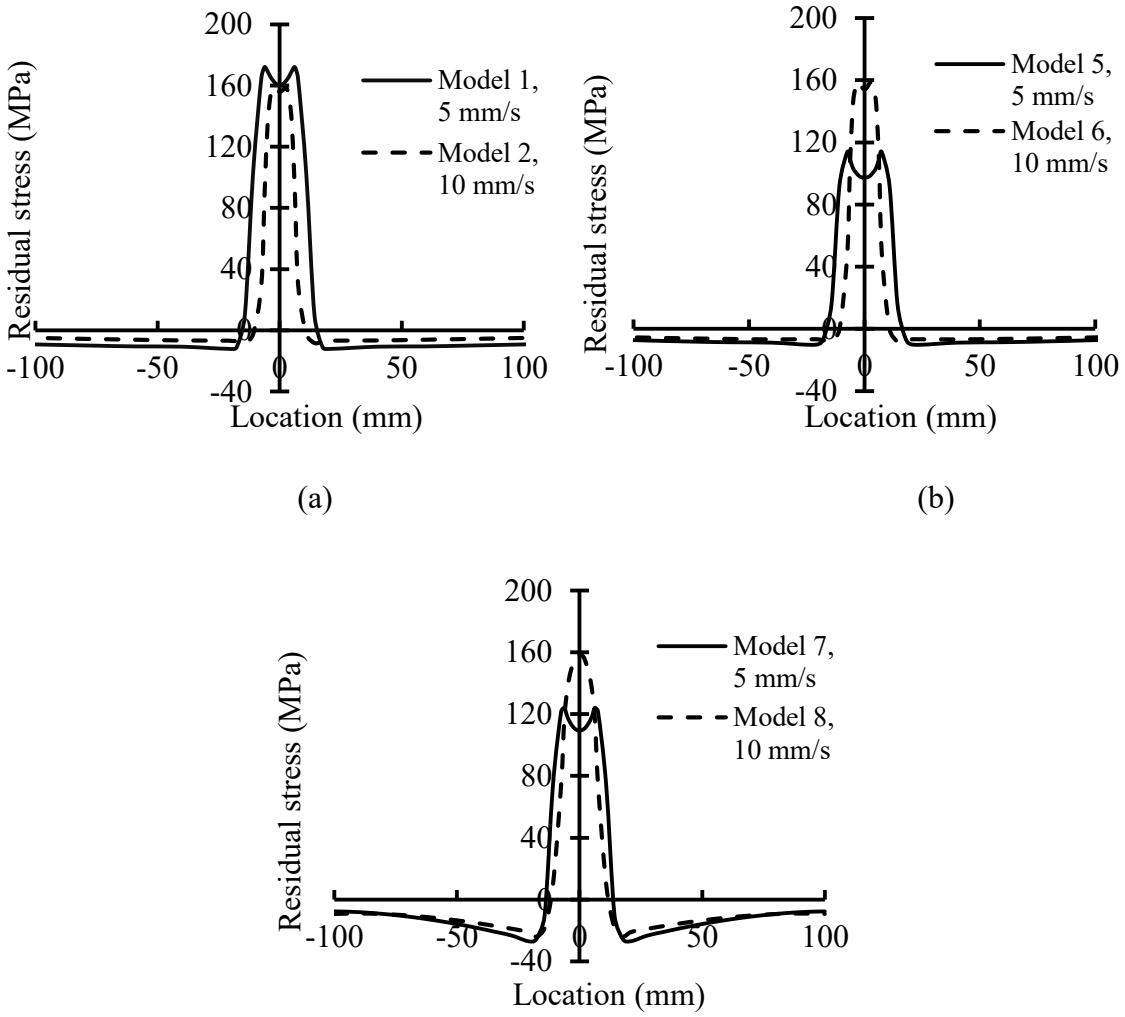

Figure 6.10 Effect of welding speed on the FSW induced longitudinal residual stress for varying clamping area

6.5 Conclusions

A three-dimensional, two-step thermo-mechanical model was developed to simulate the friction stir welding process. The model was verified with the experimental results on transient temperature and residual stress. The finite element simulation was then used to examine and compare the temperature fields, heat affected zone and residual stress generated during friction stir welding of two aluminum alloy 6061-T6 plates with different welding speed, and clamping area. Some conclusions stemming from the study are as follows:

The thermal results indicated that when the welding speed increased from 5 mm/s to 10 mm/s, the maximum temperature around the weld line decreased from 477^0C to 392^0C and the width of HAZ decreased from 9 to 6 mm, which was a 33% reduction.

The structural results revealed that for all models studied, tensile residual stress zone had a double peak "M" shape and the maximum welding induced tensile residual stress was about the yield stress of the material in HAZ. However, increasing the clamping area was shown to reduce the magnitude of this stress and the maximum reduction observed in this study was about 40% when the clamping area to plate width ratio increased from 0.5 to 0.8.

In the case of the effect of welding speed, the results indicated that welding speed had more pronounced effect on models with large clamping area than those with small clamping area. For models with large clamping areas, an increase in the welding speed resulted in as much as 60% increase in the tensile residual stress and the tensile residual stress distributed in a narrower region. For models with small clamping area which had a

tensile residual stress about the yield stress of HAZ, an increases in welding speed did not result in significant change in the magnitude of the tensile residual stress.

In summary, to reduce the residual stresses due to the friction stir welding, it is recommended to increase the clamping area and avoid using welding speeds higher than 5 mm/s.

Acknowledgements

The authors wish to recognize the contribution of financial assistance by the Natural Sciences and Engineering Research Council of Canada.

Chapter 7 - **Finite element study on the ultimate strength of extruded aluminum stiffened plates joined by either friction stir welding or metal inert gas welding**

Vahid Farajkhah [a], and Yi Liu [b,*]

Under revision in: Thin-Walled Structures,

[a] Ph.D candidate, Dalhousie University, Department of Civil and Resource Engineering, 1360 Barrington St., Halifax, NS, Canada B3J 1Z1., Email: vahid@dal.ca

[b, *] Corresponding author. Professor, Dalhousie University, Department of Civil and Resource Engineering, 1360 Barrington St., Halifax, NS, Canada B3J 1Z1, Email: yi.liu@dal.ca

7.1 Abstract

Effects of metal inert gas (MIG) welding and friction stir welding (FSW) on the welding induced initial imperfections and buckling behaviour of extruded stiffened aluminum plates were investigated. The MIG and FSW butt welding process of two extruded tee-bar stiffened plates made of aluminum alloy 6082-T6 were simulated in a two-step, thermo-structural analysis using the finite element code ANSYS. The load vs. shortening responses of extruded stiffened plates subjected to compressive loading were obtained incorporating the welding induced imperfections. Results revealed that when compared with MIG welding, the FSW resulted in about 70% less tensile and 82% less compressive residual stresses in the plate field, and the welding induced distortions of FSW models were considered negligible. The load vs. shortening curves showed that in the case of models with low plate slenderness, the FSW increased the ultimate strength by as much as 9%, while in the models with high plate slenderness, FSW decreased the ultimate strength by 3% in comparison with models joined by MIG welding.

7.2 Introduction

Due to their light weight and corrosion resistant property, aluminum plates have been increasingly used in high-speed ship building in the marine industry. Aluminum stiffened panels, constructed through welding, are traditionally used as ship hull girders. The stiffened panels usually consist of a plate with equally spaced stiffeners welded on one side, often in combination with intermediate transverse stiffeners or bulkheads. The stiffeners can be various shapes with flat bar, T-bar and angle bar being a few commonly used cross-sections. However, recent developments in extrusion technology have provided attractive alternative for fabricating aluminum stiffened plates. Panels fabricated from extruded aluminium elements can then be welded together to form the hull girders. Along with using extruded aluminum elements, new and improved welding methods have also been developed, which has shown to lead to significant improvements in geometric tolerances, increased structural efficiency and reduced costs (Aalberg et al. 2001). One of the new methods of joining which is gaining increasing popularity is friction stir welding (FSW). FSW is a solid-state joining technology invented by The Welding Institute (TWI) in 1991. The solid-state nature of FSW results in a weld with fine microstructure, absence of cracking and solidification defects (Zhu and Chao, 2004), and inherently produce a weld with less welding induced imperfections in comparison with conventional fusion welding.

One key characteristic of welding in aluminum stiffened plates, either joined by FSW or conventional fusion welding, is the formation of the heat affected zone (HAZ) around the weld line where the heat treated strength of aluminum is reduced by as much as 60%. For 6000 series aluminum alloys, all the effects of heat treatment will be lost if

the temperature reaches about 300 °C for only a short time (Davis, 1993; Beaulieu, 2006). The strength regained after the cooling down period is minimal. Other values of the temperature for formation of HAZ on 6000 series aluminum alloys have been reported by Sato et al. (1999) and Terasaki and Akiyama (2003) which were 350 °C and 325 °C respectively. In addition to HAZ, some researchers further defined a semi-HAZ zone where the aluminum strength can be assumed somewhere in between the strength of HAZ and base material. Terasaki and Akiyama (2003) defined that the semi-HAZ formed in the areas that experienced a maximum temperature between 240 °C and 325 °C. Chao and Qi (1998) defined a semi-HAZ area where the material reached a temperature between 200 °C and 300 °C.

The design of the stiffened plates are mainly based on their ultimate strength and behaviour subjected to compressive loading. Previous studies have shown that the welding induced imperfections such as residual stress, distortions and material strength reduction in HAZ had marked effect on the ultimate strength of aluminum stiffened plates. Zha and Moan (2001) studied the effects of metal inert gas (MIG) welding on the ultimate strength of welded flat-bar aluminum stiffened plates using the experimental tests and finite element analysis. They found that there was a 10 to 15% reduction in the ultimate strength of the aluminum stiffened plates due to the presence of the HAZ but the effect of residual stresses on the ultimate strength was negligible. Rigo et al. (2004) conducted a finite element study on the effect of MIG welding induced imperfections on the ultimate strength of the angle-bar aluminum stiffened plates, including the extruded stiffened plates. The results revealed that in the case of the extruded stiffened plates, the presence of the welding induced residual stress increased the ultimate strength. Paik et al (2007) used experimental and

numerical study to investigate the behaviour of aluminum stiffened plates under compressive loading. Seventy-eight prototype aluminum stiffened plates, with stiffeners welded to the plates using MIG welding, were tested. The results were used to characterize the residual stress and distortion as well as HAZ into three categories of imperfections as "light", "average", and "severe". In all aforementioned numerical studies, welding was not directly modelled, and simple idealization for residual stress and distortion distribution and heat affected zone was assumed and used in the modelling.

The literature survey yielded limited technical information on the effect of friction stir welding process on the behaviour of aluminum stiffened plates under compressive loading, especially for marine applications. Murphy et al. (2007) used finite element modeling to study the effect of friction stir welding on the static strength of stiffened panels typical of aircraft structures. Results indicated that initial skin buckling was predominantly influenced by the welding induced imperfections while the ultimate collapse performance was less sensitive to the welding imperfections. However, the friction stir welding process was not directly simulated and the welding induced imperfections were assumed and applied to the structure. Paulo et al. (2014) studied the influence of friction stir welding induced residual stresses on the strength of aluminum plates subjected to compressive loading using finite element simulation. A prescribed HAZ width was assumed in the modeling. The residual stresses were measured in an experimental test using the counter method and the obtained results were mapped in the finite element model. Three different values of initial deflection were considered. They concluded that the plate behaviour and collapse load were significantly affected by the residual stress and distortions.

Overall, the research on the effect of welding induced imperfections either by FSW or MIG welding on the aluminum stiffened plates is limited and the modelling technique used in previous numerical studies were simplified and thus may not be able to accurately capture the effect of welding induced imperfections. In light of growing popularity of FSW and a general lack of technical information on the effect of welding induced imperfections, a thorough study on the effect of welding induced imperfections by FSW and conventional MIG welding on the ultimate strength of aluminum stiffened plates is needed. In this study both the FSW and MIG butt welding process of AA6082-T6 extruded stiffened plates typical of ship structures were simulated using finite element code ANSYS. The models for both FSW and MIG welding were subsequently validated using the experimental results available in the literature. Following the simulation of welding processes, compressive loading was applied to the extruded aluminum stiffened plates fabricated using either methods to obtain the load vs. shortening curves. A parametric study was then carried out to investigate and compare the effect of the fabrication methods on the welding induced imperfections as well as buckling behaviour and ultimate strength of the stiffened plates under compressive loading. To the best knowledge of the authors, this is the first time that the FSW process was simulated and the welding induced residual stress, HAZ and distortions were directly used in the structural analysis of the structures fabricated by this welding method.

7.3 Numerical simulation

The model consisted of two extruded tee-bar aluminum plates weld-connected at their longitudinal edges by either FSW or MIG. The plates were made of AA6082-T6, which is widely used in the construction of aluminum high speed vessels. The simulation of both the FSW and MIG processes were carried out in a two-step thermo-mechanical nonlinear analysis using ANSYS. In the first step, the moving thermal loads caused by the FSW and MIG processes were simulated and applied to the model and a nonlinear transient thermal analysis was performed to determine the temperature field history. The HAZ was then determined based on the temperature gradient for the welded plates. In the second step, the obtained temperature distribution history was applied to the model as a series of load steps, where each load step represents an increment in the position of the welding tool. Note that in the second step of FSW process, both the temperature distribution history and the plunging force from the rotating tool were applied to the model. The structural analysis of the model provided the residual stresses and distortions induced by the welding heat source. The same meshing patterns were used for both the thermal and structural analysis but with different elements. The SOLID70 eight node thermal element was used in the thermal model whereas its equivalent structural element SOLID185 was used in the structural model. A typical finite element mesh is shown in Figure 7.1 for both MIG and FSW models. As can be seen, a relatively dense meshing were used in the vicinity of the weld line. In the regions away from the weld line the density of the mesh is reduced to decrease the number of degrees of freedom and thus the time required for the analysis.

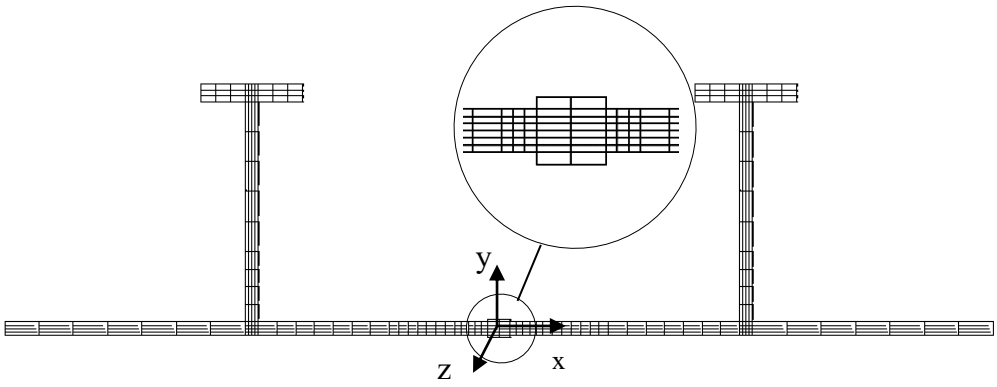

(a)

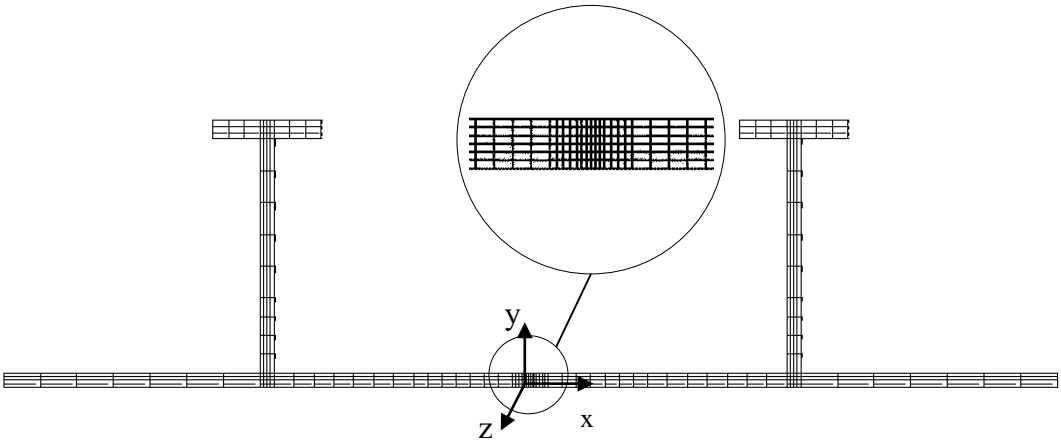

(b)

Figure 7.1 Typical meshing pattern of (a) MIG and (b) FSW finite element models

Temperature dependent thermal and mechanical material properties were incorporated in the model. The thermal material properties required were density, specific heat and thermal conductivity, and the mechanical material properties included Young's modulus, yield stress and thermal expansion coefficient. A constant value of 0.33 for the Poisson's ratio was considered over the temperature history. Except for the material yield stress, all of the temperature dependent thermal and mechanical material properties for

6000 series of aluminum were adopted from Riahi & Nazari (2011). The yield stress variation over the temperature history for AA6082-T6 was adopted from Eurocode 9 (1998). The temperature dependent heat transfer coefficient for 6000 series of aluminum alloys was adopted from Moraitis and Labeas (2008). These properties are shown in shown in Figure 7.2.

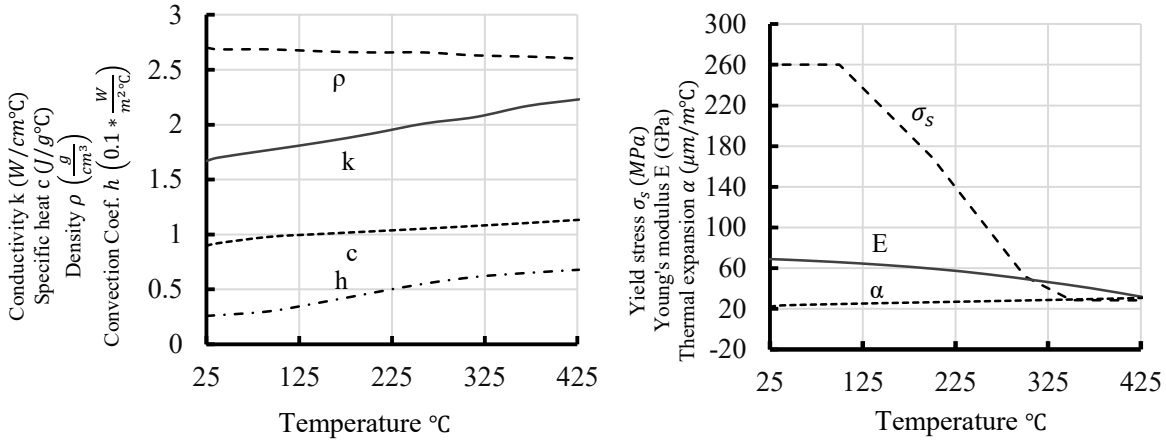

(a) (b)

Figure 7.2 Temperature dependent material properties for aluminum alloy 6061-T6 (a) thermal properties (b) mechanical properties

The material model used was Ramberg-Osgood model of the non-linear stress-strain relationship for the AA6082-T6 as defined in the following:

$$\varepsilon = \frac{\sigma}{E} + 0.002\left(\frac{\sigma}{\sigma_{0.2}}\right)^{n} \tag{7.1}$$

Based on the experimental work of Zha and Moan (2001) on the AA6082-T6, the 0.2% proof stress, $\sigma_{0.2}$, was taken as 260 MPa and the exponent, *n*, was taken as 46.

In the finite element simulation, the material strength reduction in the HAZ was simulated based on the peak temperature the material experienced during the welding. Similar to concepts used by Chao and Qi (1998), it was assumed in this study that the weld area was divided into three zones, i.e., HAZ, semi-HAZ, and base metal zone. In the finite element analysis of both the FSW and MIG welding processes, as welding progressed the average temperature of elements were queried and the material properties of those elements were changed corresponding to the maximum temperature according to Table 7.1.

Table 7.1 Material strength with respect to temperature

	Temperature T	% of yield stress of base metal
HAZ	$T \geq 300$ ºC	53
Semi-HAZ	200 ºC $\leq T <$ 300 ºC	77
Base metal zone	$T <$ 200 ºC	100

7.3.1 Finite element simulation of MIG welding

The simulation of the MIG welding process was carried out in a two-step thermal-structural nonlinear analysis. In the thermal analysis, the moving heat source was developed where the 60% of the total heat input of welding was assumed to be transferred to the workpiece via the molten metal droplets. This was simulated by applying a volumetric heat generation rate to the weld elements. The remaining 40% was assumed to be transferred via the surface heat flux. A Gaussian distribution with an arc radius of 5 mm was considered for the heat flux. The total heat input of the welding can be calculated as:

$$Q = \eta VI \tag{7.2}$$

where V is the arc voltage, I is the arc current, and η is the arc efficiency factor which is 0.85 for CO_2 gas metal arc welding. User-defined macros were developed using ANSYS parametric design language (APDL) to model the movement of the heat source and the deposition of the molten metal droplets on the workpiece. Heat loss due to the combined effects of convection and radiation was accounted for by applying a temperature dependent heat transfer coefficient (Figure 7.2) on the free surfaces of the work piece.

In the structural analysis, the temperature field history calculated in the thermal analysis were applied as a series of thermal loads where each load step represented an increment in the weld deposition. The deposition of the weld droplets on the workpiece was simulated using the ANSYS element birth and death feature. In the beginning of the analysis all of the weld elements were deactivated (killed). As the welding torch progressed a user defined subroutine was implemented to apply the calculated temperature field in the corresponding time and to query the average temperature of the deposited weld elements after the weld torch. Those elements whose temperature fell below the solidification temperature were activated again, representing the deposition of the weld elements on the workpiece. The solidification temperature for AA6082-T6 was set as 555 $^{\circ}$C. The weld elements were activated with no strain history and their reference temperature was set equal to the solidification temperature to calculate the thermal strains.

To check the validity of the developed model for MIG welding process, the experimental results of Masubuchi (1980) were used. The geometry and welding configuration of the test are shown in Figure 7.3. The welding parameters and material properties were given by Masubuchi (1980). The plate was 12.5 mm thick and made of

AA5052-H32. The plate was simply supported in both ends and the upper longitudinal edge of the plate was welded by MIG welding.

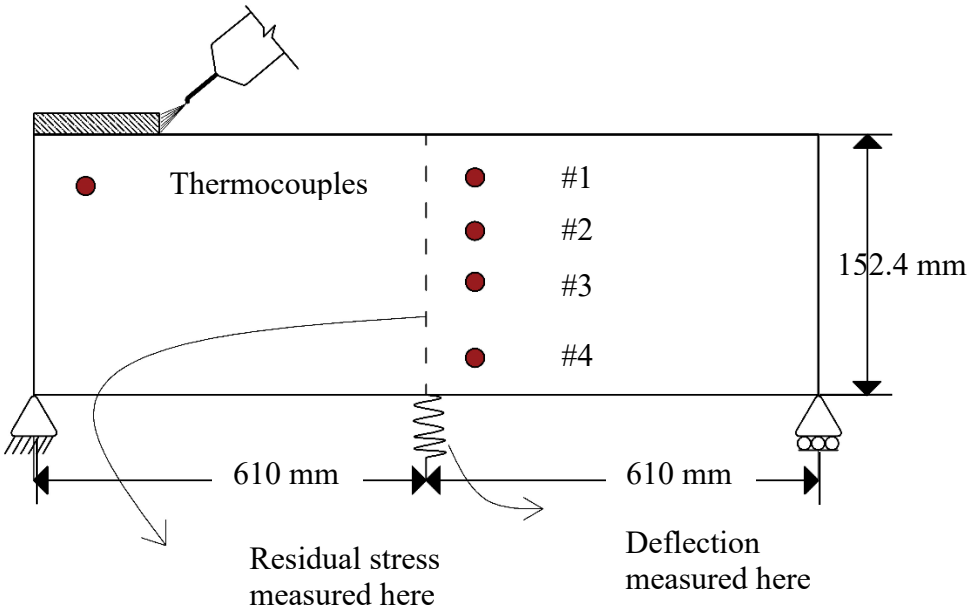

Figure 7.3 Test setup of Masubuchi (1980)

The calculated results for the temperature history is compared to the experimental results in Figure 7.4. Furthermore, the obtained structural results for the vertical deflection at the mid-point of the plate as well as the longitudinal residual stresses in the middle cross-section of the plate are compared to the experimental results in Figure 7.5. The figures show that the results obtained by the developed finite element model compare well with the experimental test results, and the finite element model can simulate both the temperature distribution and the resulting deformation and residual stress with reasonable accuracy.

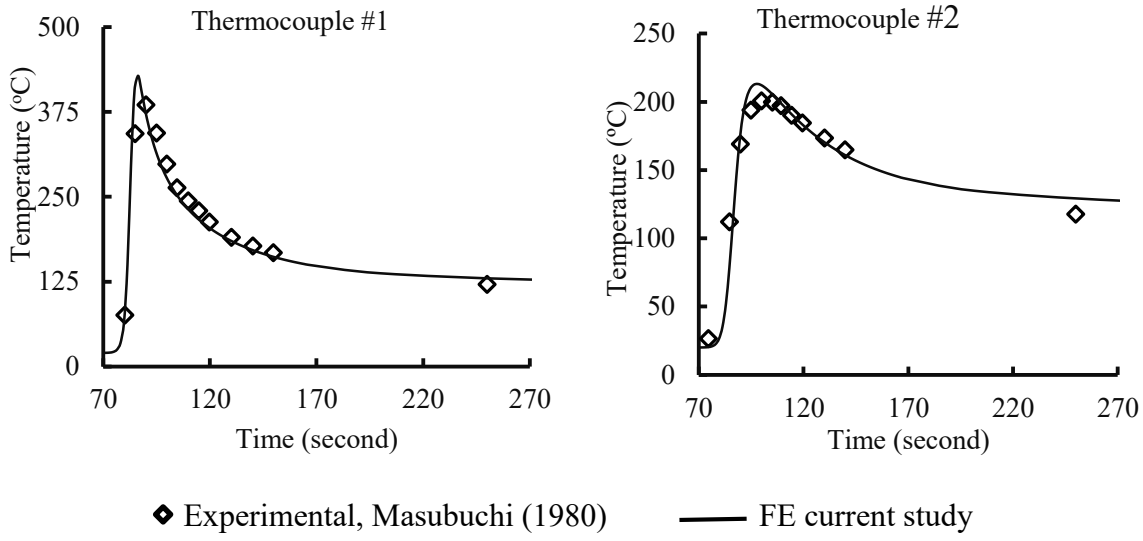

Figure 7.4 Comparison of temperature history at thermocouples

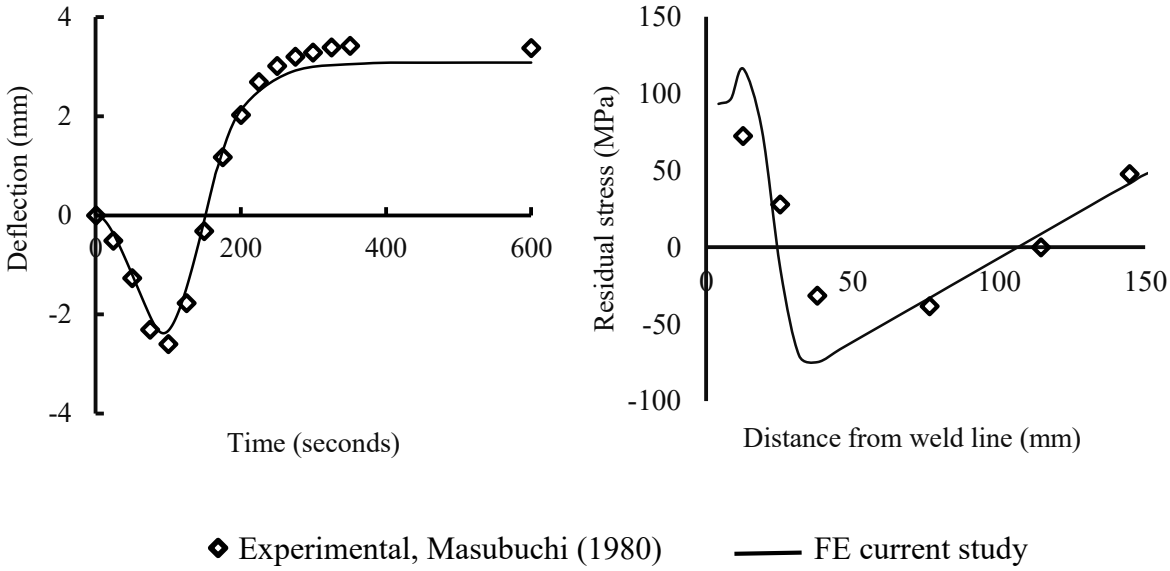

Figure 7.5 Comparison of transient vertical deflection and longitudinal residual stress at the middle of the plate

7.3.2 Finite element simulation of FSW

The key component in the simulation of the FSW process is the modeling of heat generation. In this study it was assumed that the heat was generated during the process based on the contact condition between the rotating welding tool and the workpiece using the method provided by Schmidt et al. (2004). The heat was assumed to be generated at three interfaces. These were the heat generated at the interface of the tool shoulder and the workpiece, $Q_{shoulder}$; the heat generated at the interface of the pin side surface and the workpiece, $Q_{pin,side}$, as well as at the tip of the pin and workpiece, $Q_{pin,tip}$. The expressions for each of them were given by Schmidt et al. (2004) as:

$$Q_{shoulder} = \int_0^{2\pi} \int_{R_{pin}}^{R_{shoulder}} \omega \tau_{contact} r^2 (1 + \tan \alpha) dr d\theta \tag{7.3}$$

$$Q_{pin,side} = \int_0^{2\pi} \int_0^{h_{pin}} \omega \tau_{contact} {R_{pin}}^2 dz d\theta \tag{7.4}$$

$$Q_{pin,tip} = \int_0^{2\pi} \int_0^{r_{pin}} \omega \tau_{contact} r^2 dr d\theta \tag{7.5}$$

where ω is the angular velocity, r is the radius of shoulder, $\tau_{contact}$ is the shear stress in the surface, and α is the shoulder cone angle. Consequently, the total heat generated in Watts (W) by the FSW process Q_f, is the summation of the heats generated in each interface of the welding tool and workpiece:

$$Q_f = Q_{shoulder} + Q_{pin,side} + Q_{pin,tip} \tag{7.6}$$

The generated heat was modeled as the heat fluxes applied to the interface of the welding tool and workpiece, moving forward by the speed of the welding. A linear

distribution with respect to *r*, the distance between the tool centerline to the edge of the shoulder, was considered for the generated heat, based on the assumption that the welding tool applies a uniform plunging force to the workpiece. The expression for the heat distribution was given by Chao et al. (2003) as follows:

$$q(r) = \frac{3Q_f r}{2\pi R_{shoulder}^3} \tag{7.7}$$

where $R_{shoulder}$ is the outside radius of the shoulder of the tool and Q_f is the total heat input calculated using Eqn (7.6).

Heat loss from the free surfaces of the workpiece due to the combined effects of convection and radiation was accounted for by applying a temperature dependant convection coefficient to all free surfaces of the workpiece. It can be evaluated as:

$$q_s = \beta(T - T_0) + \varepsilon B(T^4 - T_0^4) \tag{7.8}$$

where T_0 is the room temperature, ε is the emissivity of the plate surface and B is the Stefan-Boltzmann constant which equals to $5.67\times10^{-8} Wm^{-2}k^{-4}$, and β is the heat transfer coefficient as given in Figure 7.2. As the bottom surface of the workpiece was in direct contact with the backing plate a higher convection coefficient was assumed for modeling the heat loss from the bottom surface with an expression as:

$$Q_b = \beta_b (T - T_0) \tag{7.9}$$

where β_b is the convection coefficient between the workpiece surface and the backing plate and it was assumed to be $350\, W/m^2 K$ based on the work of Chao et al. (2003).

In the structural analysis, two types of loading were considered. One was the temperature field history calculated in the thermal analysis, and the other was the plunging force applied to the workpiece by the welding tool. A user defined sub-routine was developed to apply the temperature field from the thermal analysis accompanied with the plunging force in the corresponding times as a series of load steps, where each load step represented an increment in the location of the welding tool. The pressure, *P,* due to the plunging force applied to the workpiece by the tool shoulder was modeled as a uniform pressure moving forward with the speed of welding and it is expressed as follows:

$$P = \frac{F}{A_{shoulder}} \tag{7.10}$$

where $A_{shoulder}$ is the area at the interface of the tool shoulder and the workpiece.

For the verification of the FSW finite element model, the thermal results were compared with the experimental results of Guo et al. (2014) where a 6 mm thick AA6061 plate was welded to a 6 mm thick AA7075 plate using friction stir welding. The welding parameters including the plunging force, welding tool rotation and traveling speed as well as the geometry and temperature dependant material properties were provided in the referenced paper. Figure 7.6 shows the comparison of temperature history measured at 10 mm away from the weld line where a good agreement between the finite element model and the test results was obtained.

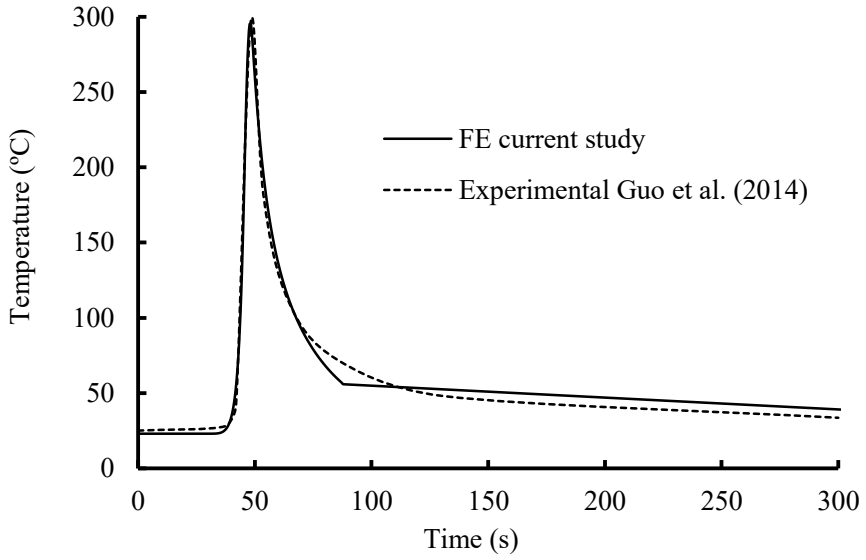

Figure 7.6 Comparison of temperature history profile at 10 mm away from the joint

Furthermore, the models were also verified using the experimental test results of Zhu and Chao (2004) where 3.18 mm thick plates of 304L stainless steel were welded together by FSW. The welding heat input was provided by Zhu and Chao (2004). Figure 7.7 shows the longitudinal residual stresses on the cross-section in the mid-length of the workpiece obtained by the experimental tests and the developed finite element model after the release of the clamps. Note that no experimental results were available for the residual stress distribution before the release of the clamps. The finite element residual stresses before the release of the clamps were also shown. Also included in the figure are the numerical results of Zhu and Chao (2004). The figure shows that the finite element model developed in this study provided reasonably accurate results of welding induced residual stresses after the clamp release. Although the experimental results of residual stress distribution before the clamp release was not available, judging from the fact that

the model developed in this study also compared well with that developed by Zhu and Chao (2003), it is reasonable to deduce that the model developed herein is capable of accurate simulation of the FSW process. It is also noted that the residual stresses reduced significantly after the release of the clamps.

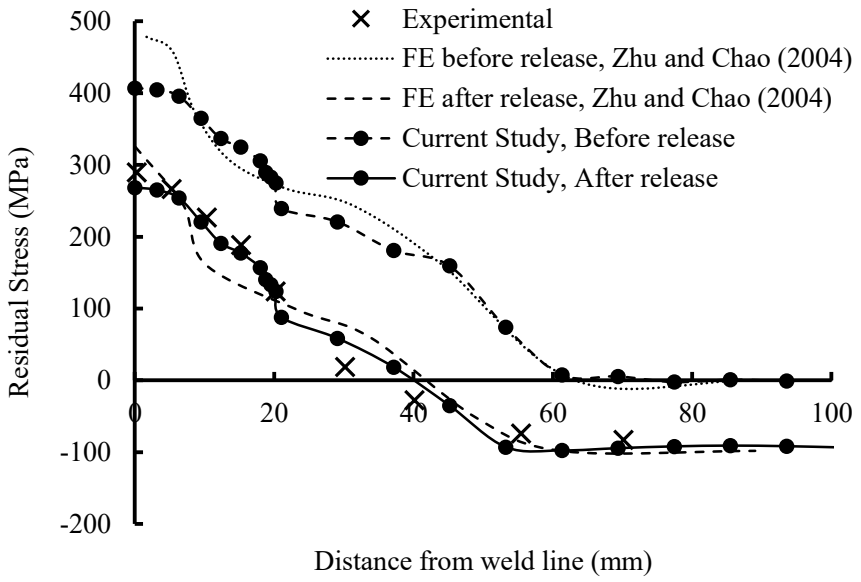

Figure 7.7 Longitudinal residual stress along the cross-section

7.4 Comparison study on FSW and MIG welding

A comparative study on the FSW and MIG welding processes was conducted on two extruded tee-bar aluminum stiffened plates joined together by either welding process. The study included two comparative aspects where welding induced HAZ, residual stress and distortion fields as well as load-shortening curves, ultimate strength, and post-buckling

behaviour of models from both welding methods were studied and compared. The stiffened plates considered were made of AA6082-T6 with a 6 mm thickness. The meshing of the models can be referred to as in Figure 7.1. The welding process of the MIG models were carried out in both sides of the plate. After the MIG welding of the first side was finished the model was allowed to cool down for half an hour, and after the welding of the other side the models were allowed to cool down to the room temperature. The MIG welding parameters, voltage, current and welding speed were adopted from JF Lincoln Arc Welding Foundation (2000). The FSW process parameters were adopted from the test results of Guo et al. (2014) where standard values of welding tool rotational speed of 1200 rpm with a traveling speed of 5 mm/s were suggested.

The plate geometry was varied through the plate slenderness β and the beam-column slenderness λ as given in Eqn (7.11) and (7.12) respectively.

$$\beta = \frac{b}{t}\sqrt{\sigma_y / E} \tag{7.11}$$

$$\lambda = \frac{a}{\pi r}\sqrt{\sigma_y / E} \tag{7.12}$$

where *b, a*, and *t* are the width, length, and thickness of one plate; and *r* is the radius of gyration of the plate. For AA6082-T6, the yield stress, σ_y, and Young's modulus, E, are taken as 260 MPa and 70 GPa, respectively. Geometric details of finite element models are listed in Table 7.2 with key dimensions illustrated in Figure 7.8. The dimension were chosen to include a range of plate slenderness and beam-column slenderness that would be encountered in practice.

Table 7.2 Tee-bar aluminum stiffened plate model dimensions (all dimensions in mm)

Model	alloy	a	b	t_p	h_w	t_w	b_f	t_f	β	λ
ID1	6082	1000	225	6	100	6	40	8	2.285	0.423
ID2	6082	1000	225	6	55	4	40	6	2.285	0.867
ID3	6082	1000	300	6	100	6	40	8	3.047	0.490
ID4	6082	1000	300	6	60	4	40	6	3.047	0.869

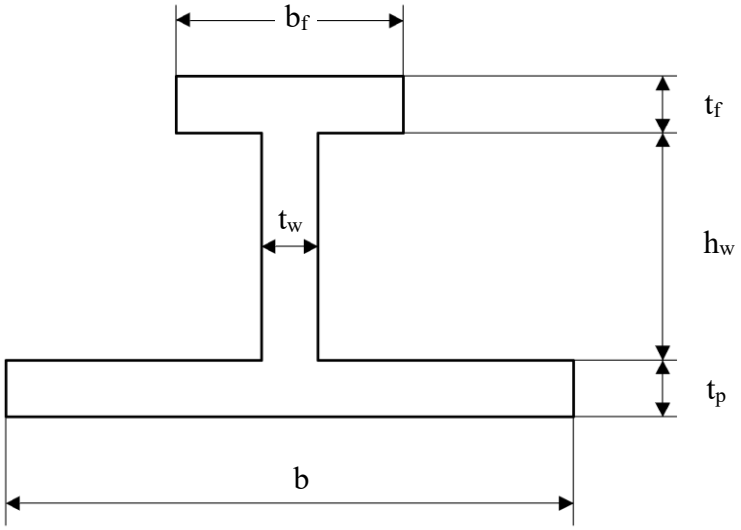

Figure 7.8 Tee-bar stiffened plate dimensions

Boundary conditions representative of the level of the restraints applied to stiffened plates in ship hull girders were considered. Simple support conditions were applied to both ends of the extruded stiffened plates. The centroid of each extruded stiffened plate at one end was restrained for displacements in all three directions and the centroid at the other end was restrained against the displacements in transverse and vertical direction. The longitudinal edges of the plates were restrained to remain straight when moving in the

plane of the plating and free to move out of the plane of the plating as suggested by Dow et al. (1981). This was achieved by restraining the rotation of the longitudinal edges about the longitudinal and vertical axis (Gannon et al., 2012).

7.4.1 Thermal results and HAZ

Figure 7.9 shows the distribution of the temperature field obtained at both the mid-thickness and top surface of the mid-length cross-section of the plate for model 1 when the welding tool reached the cross-section. Note that the remaining three models showed practically the same temperature field history in their respective FSW and MIG welding method, and thus for clarity they are not included in the figure. As can be seen, the maximum temperature during the FSW process reached 480 ºC and it was located at the top surface of the workpiece. This temperature was about 75 ºC less than the melting point of AA6082-T6 and was within an acceptable range for the FSW process (Chao and Qi, 1998; Riahi and Nazari, 2011). Furthermore, the heat affected zone where the temperature reached 300 ºC and higher extended about 9 mm from the weld line as shown in Figure 7.9. In comparison, the figure shows that during the MIG welding process the maximum temperature reached about 1687 ºC which was 1132 ºC higher than the melting point of AA6082-T6. The HAZ due to the MIG welding process extended about 15 mm from the weld line, which was 1.6 times the HAZ caused by FSW process.

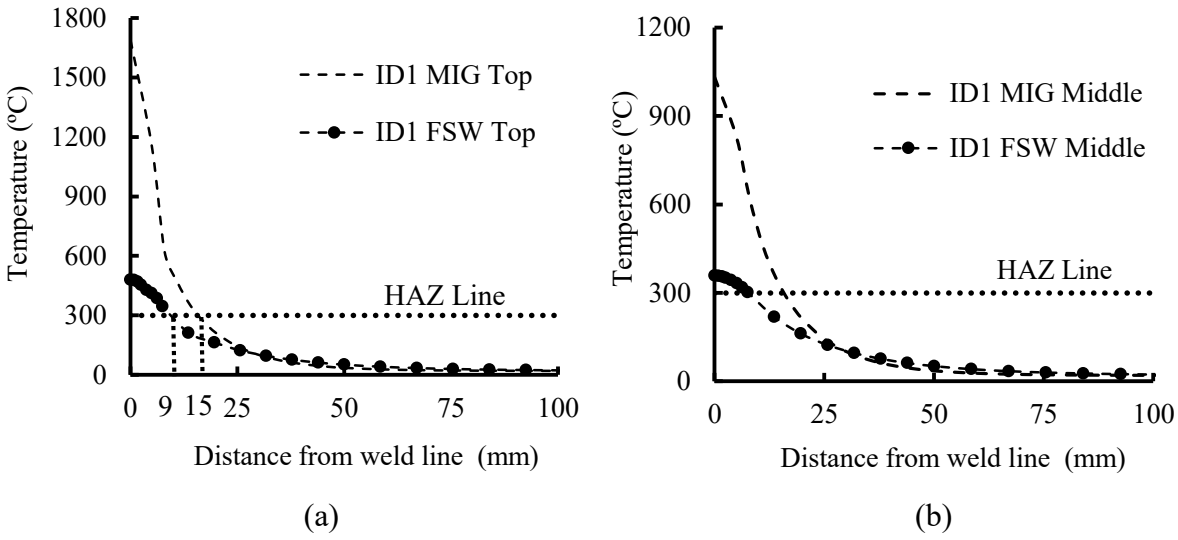

Figure 7.9 Temperature distributions along the transverse direction

7.4.2 Residual stress and distortions

Although the welding induced residual stress is three dimensional, the longitudinal component of the residual stress is considered to be the largest in value and to have the greatest impact on the ultimate strength and buckling of stiffened plates. In the FSW models the stiffened plates were assumed to be clamped to backing plates where clamping was applied to the top surface of the plates untill 50 mm from the weld line in each direction. After the FSW was complete and the workpiece was cooled to room temperature, the clamps were released. As discussed earlier, the residual stress reduced significantly after the release of the clamps. Hence in this study the residual stresses shown were obtained after the release of the clamps.

Figure 7.10 and Figure 7.11 show the variation of the longitudinal residual stresses in plates and stiffeners obtained at the mid-thickness in the mid-length cross-section for FSW and MIG models respectively. As can be seen in Figure 7.10(a), in the FSW models

the tensile residual stress developed in the weld centerline ranged from 40 to 43 MPa and the maximum tensile residual stress was about 67 MPa located about 7.5 mm away from the weld centerline. Both magnitudes were relatively small, representing about 16% and 25% of the yield strength of AA60802-T6 base material. The variation in either plate slenderness or column slenderness did not result in any marked variation in the residual stress magnitude or distribution. The width of the tensile residual stress zone was about 38 mm for all FSW models. Small compressive residual stresses were present away from the weld line to balance the tensile residual stress with the maximum magnitude ranging from only 5 to 7 MPa. Figure 7.10(b) shows that the residual stresses developed in the stiffeners were also small and can be considered negligible. The maximum tensile and compressive residual stresses in the stiffeners were less than 1 and 4 MPa respectively.

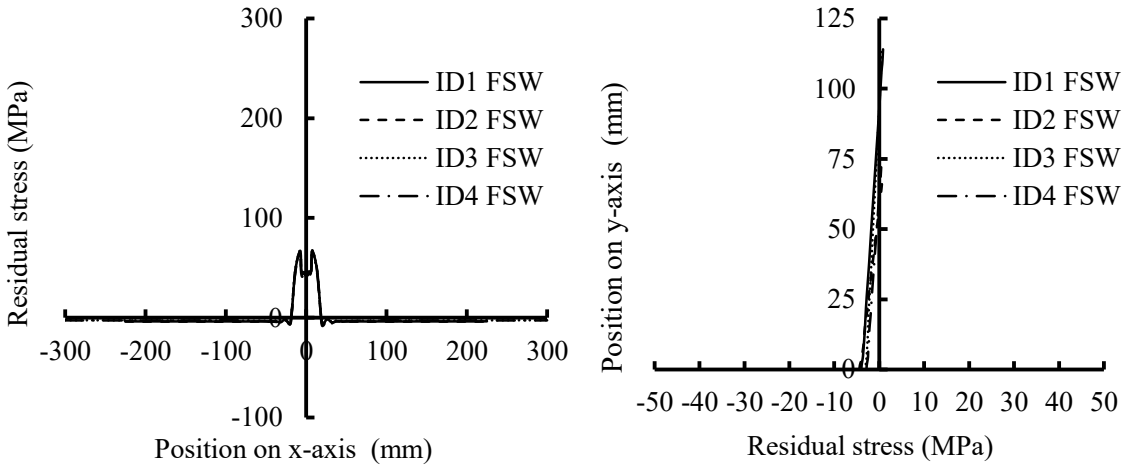

Figure 7.10 FSW induced longitudinal residual stress at mid-length cross-section (a) plate (b) stiffener

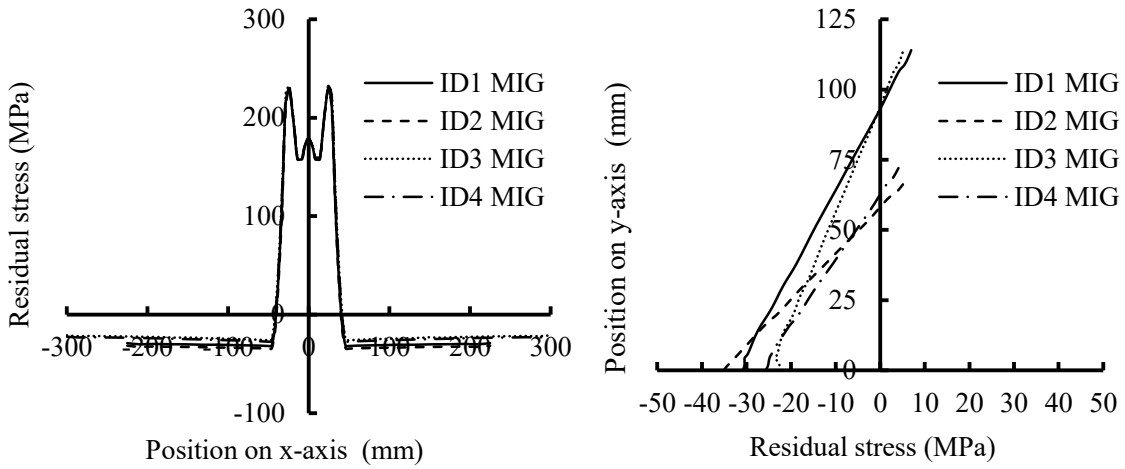

(a) (b)

Figure 7.11 MIG welding induced longitudinal residual stress at mid-length cross-section (a) plate (b) stiffener

In comparison, Figure 7.11(a) shows that in MIG models the tensile residual stress was about 179 MPa in the weld centerline which was about 68% of the base material yield stress. The maximum tensile residual stress was located about 25 mm away from the weld line with a magnitude ranging from 229 to 232 MPa, about 88% of the base material yield stress. The width of the tensile residual stress zone was about 80 mm for all MIG models. The results also show that compressive residual stresses developed ranging from 21 to 33 MPa in the plate of MIG models. The maximum compressive residual stress in the stiffeners were developed in the conjunction of the plate and stiffeners with a range between 22 and 35 MPa in all models with varying plate and column slenderness. It is noted that the plate slenderness and column slenderness did result in magnitude and distribution variation in residual stresses for MIG models. However, the variation is still considered insignificant.

In summary, AA6082-T6 extruded stiffened plates welded by FSW resulted in respectively 70% and 82% lower maximum tensile and compressive stresses in the plate than those developed due to MIG welding. The width of tensile residual stress region showed around 53% reduction. Also in contrast with the MIG models, in FSW models negligible residual stresses were developed in the stiffeners.

Figure 7.12 shows the vertical deflection in the transverse direction at the mid-length as well as in the longitudinal direction along the weld line of the FSW models. In both cases, the magnitude of deflections was relatively small. The maximum deflection in the mid-length occurred in model 2 with the lowest plate slenderness and stiffener height, and the magnitudes were only about 0.15 mm. The low level of deflections in these models can be attributed to the low level of temperature the models experienced during welding, as well as the restraining effects applied by the clamps to the plates. On the other hand, the results of MIG models are shown in Figure 7.13 where significantly higher deflections are observed. Again the maximum vertical deflection in the transverse direction at the mid-length occurred in model 2 which was 1.2 mm and the maximum vertical deflection in the longitudinal direction along the weld line occurred in model 3, which was about 5 mm at one end of the plate.

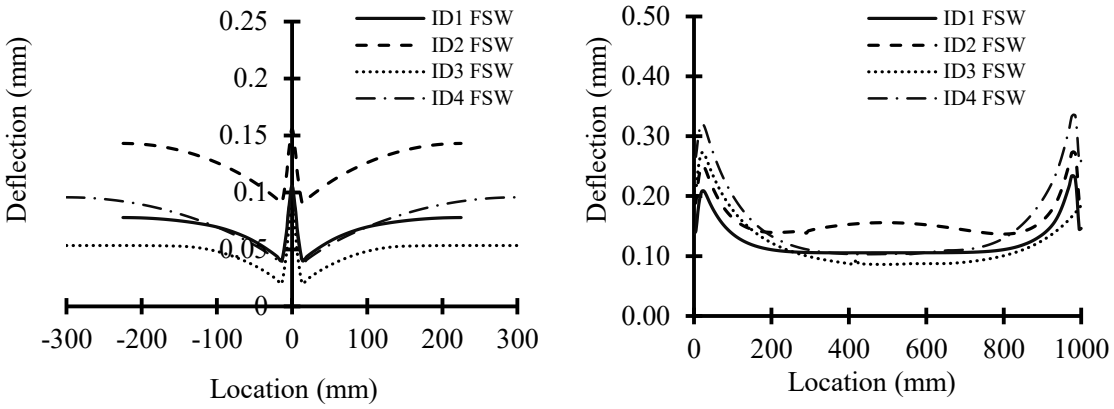

Figure 7.12 Vertical deflections in mid-length cross-section and along the weld line of FSW models

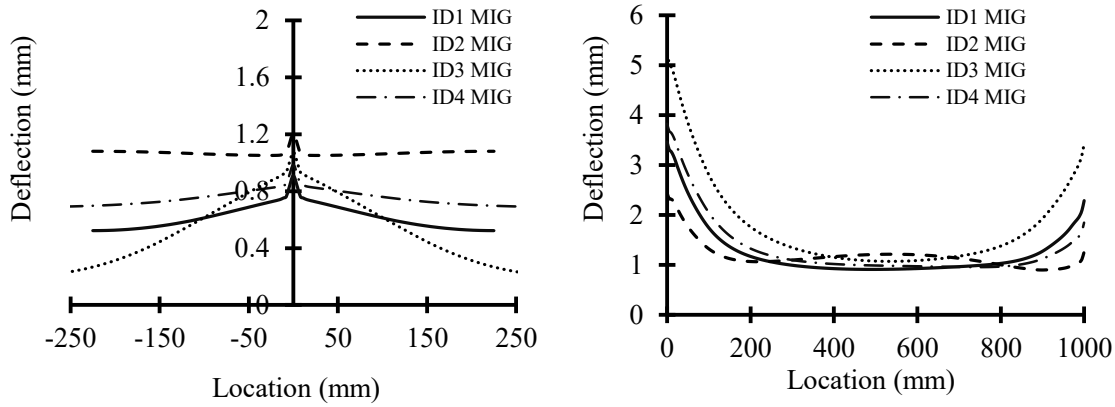

Figure 7.13 Vertical deflections in mid-length cross-section and along the weld line of MIG models

7.4.3 Behaviour under compressive loading

Following the simulation of the welding process, the behaviour of the extruded aluminum stiffened plates joined by either the FSW or MIG welding process under compressive loading was studied. This behaviour can be described using load vs. shortening curves. To obtain these curves, a displacement controlled analysis was performed where axial displacements were applied to the centroidal node of each extruded aluminum stiffened plate at one end where only in-plane translations were restrained. The prescribed displacement resulted in a force at the centroidal node of the other end which was restrained against displacements in all directions. The axial displacements, instead of forces, were used so that the post-buckling behaviour of the model can be obtained. In order to ensure that the compressive loading was uniformly distributed over the entire cross-section and the cross-sections would remain plane during the ultimate strength analysis, beam elements with high bending and axial stiffness were used to connect all nodes at each end cross-section of the stiffened plates to the centroidal nodes of the end cross-section. These elements were inactive during the welding simulation and then activated for the ultimate strength analysis using the ANSYS element birth and death feature.

Figure 7.14 and Figure 7.15 show the obtained load vs. shortening curves for plate slenderness β of 2.285 and 3.047 respectively. The figures show that welding methods did not have any significant influence on the pre- or post-buckling behaviour where for a given plate slenderness, the initial stiffness and response prior to buckling as well as the response after buckling of all models were practically identical. The only evident difference was on the buckling load. Table 7.3 summarizes the results of ultimate strength and buckling

modes. It shows that for a plate slenderness of β=2.285, the extruded elements joined together using the FSW attained higher ultimate strength by as much as 9% than using the MIG welding process. However, for a plate slenderness of β=3.047, the opposite trend was observed where using the FSW resulted in a lower ultimate strength (around 3%) than using MIG welding process. Noting that the tensile residual stresses had greater magnitude and wider distribution range in MIG models than FSW models, this suggests that the high tensile residual stress may have a beneficial effect on the ultimate strength for extruded stiffen plates with certain geometric characteristics. This is attributed to the fact that when the extruded stiffened plates are subjected to compression, the presence of tensile residual stress can cancel, to some degree, the effect of the compressive stresses and thus delay the buckling. This is in line with a previous study on the extruded aluminum stiffened plates conducted by Rigo et al. (2003) which showed that tensile residual stresses in the middle of the plate field had a beneficial effect on the ultimate strength. As the plate slenderness increases, the plates are more susceptible to buckling, hence, the beneficial effect of higher tensile residual stresses due to MIG welding becomes more pronounced in improving the ultimate strength.

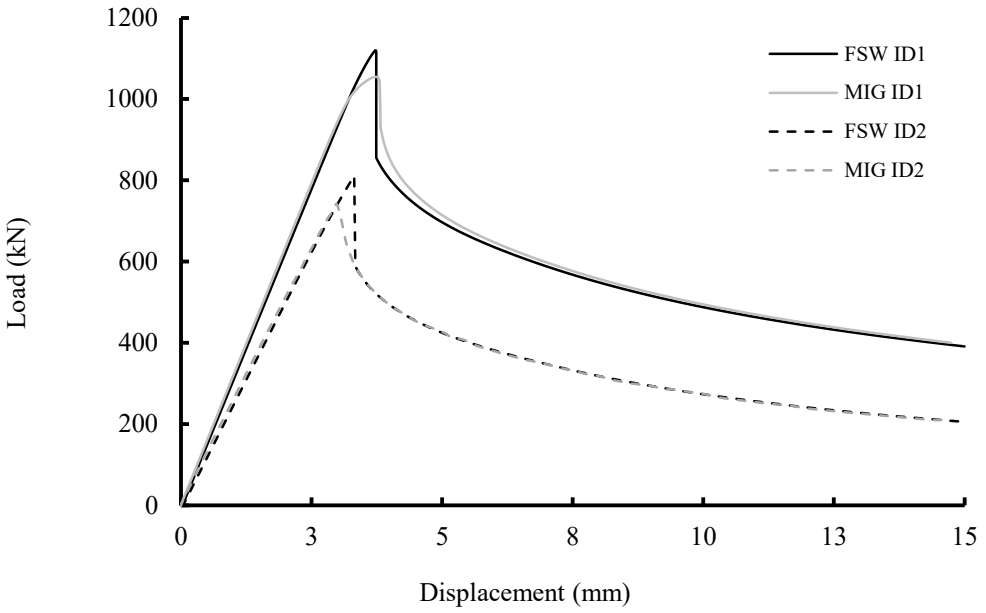

Figure 7.14 Load vs. shortening curves for models with β=2.285

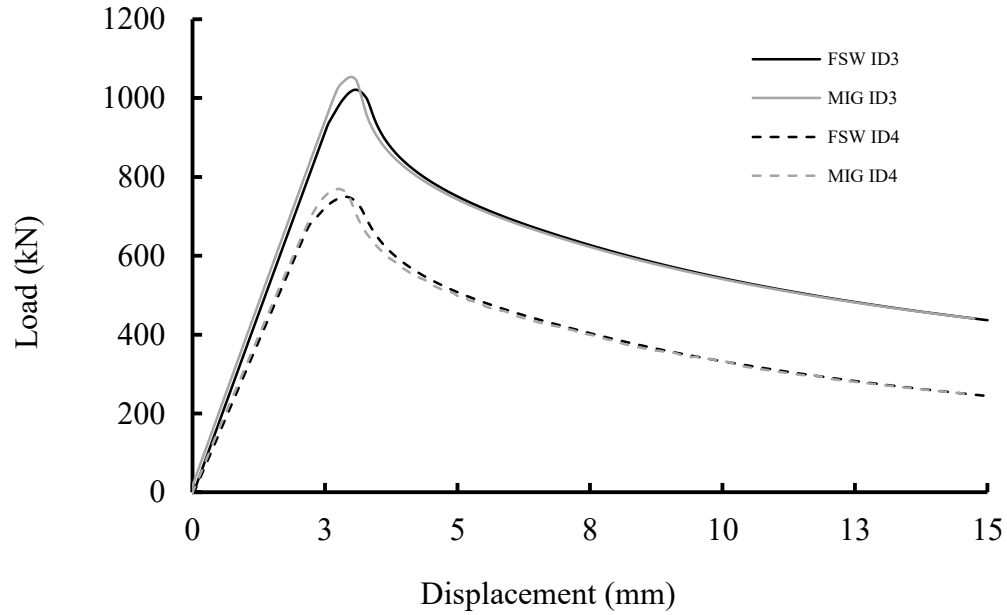

Figure 7.15 Load vs. shortening curves for models with β=3.047

Table 7.3 Tee-bar aluminum stiffened plate model dimensions (all dimensions in mm)

Model	β	λ	Ultimate strength		% Difference between FSW & MIG	Buckling mode
			FSW (kN)	MIG (kN)		
ID1	2.285	0.423	1120	1054	6.3	II
ID2	2.285	0.867	810	741	9.3	I
ID3	3.047	0.490	1020	1053	-3.1	II
ID4	3.047	0.869	748	769	-2.7	I

Table 7.3 shows that models failed either by plate buckling mode (mode I) or stiffener induced collapse by web buckling (mode II). Models 1 and 3 with higher stiffener height failed by the stiffener induced collapse by web buckling while model 2 and 4 with lower stiffener height failed by the plate buckling mode. Examples of both failure modes are shown in Figure 7.16. In stiffener web buckling mode, stiffener buckling was accompanied by the buckling of the plate immediately after. The finite element results also revealed that welding process did not have any effect on the failure mode and the models welded by either welding processes experienced the same buckling mode.

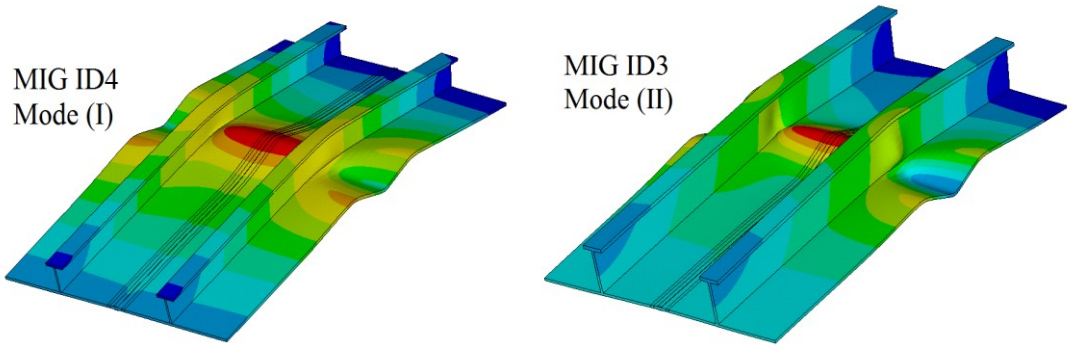

Figure 7.16 Buckling deformed shapes

7.5 Conclusions

A two-step, thermo-structural nonlinear finite element model was developed to simulate both the friction stir welding and metal inert gas welding joining process of two tee-bar extruded aluminum stiffened plates made of AA6082-T6. The developed model was verified with the available experimental data. The welding induced initial imperfections as well as the load vs. shortening behaviour under compressive loading as affected by both welding methods were studied and discussed. Some conclusions stemming from the study are as follows:

The thermal analysis of both welding methods revealed that in the FSW process, the maximum temperature reached about 85% of the melting temperature of AA6082-T6 while in the MIG welding process, the maximum temperature the material experienced was 1000 ^{o}C more than the melting point. The heat affected zone due to FSW extended 9 mm from the weld center-line in each direction and this width was 15 mm for the MIG welding.

In the case of the welding induced residual stress, the FSW process resulted in a maximum tensile residual stress of about 25% of the AA6082-T6 yield stress and a negligible compressive residual stress in the plate field. On the other hand, MIG welding caused a maximum tensile residual stress of about 88% of the yield stress and a compressive residual stress of about 10% of the yield stress. In the case of welding induced distortion, the results indicated that MIG welding resulted in a considerable level of distortion in both transverse and longitudinal directions. In comparison, the distortions due to FSW process were almost negligible.

The load vs. shortening results revealed that joining the extruded aluminum stiffened plates using either FSW or MIG welding did not have significant effect on the strength of the models before and after the buckling point . Their effect was observed in the ultimate strength. In the case of the models with relatively small plate slenderness, using the FSW increased the ultimate strength by as much as 9% in comparison with models welded by MIG welding. For the models with greater plate slenderness, using the MIG welding, however, increased the ultimate strength by as much as 3%. This can be related to higher tensile residual stress caused by the MIG welding in the middle of the plate field, which can postpone the buckling of the model under compressive loading.

Acknowledgements

The authors wish to recognize the contribution of financial assistance by the Natural Sciences and Engineering Research Council of Canada.

Chapter 8 - **Effect of fabrication methods on the ultimate strength of aluminum hull girders**

Vahid Farajkhah [a], Yi Liu [b,*]

Published in: Ocean Engineering,

DOI: 10.1016/j.oceaneng.2016.01.029

[a] Ph.D candidate, Dalhousie University, Department of Civil and Resource Engineering, 1360 Barrington St., Halifax, NS, Canada B3J 1Z1., Email: vahid@dal.ca

[b, *] Corresponding author. Professor, Dalhousie University, Department of Civil and Resource Engineering, 1360 Barrington St., Halifax, NS, Canada B3J 1Z1, Email: yi.liu@dal.ca

8.1 Abstract

A three-dimensional nonlinear finite element model was developed to simulate the welding process of extruded and non-extruded aluminum tee-bar stiffened plates joined together by friction stir welding (FSW), metal inert gas (MIG) butt and MIG fillet welding. The three-dimensional residual stress and distortion fields as well as the heat affected zones (HAZ) for all three welding methods were obtained and compared. The load-shortening curves for stiffened plates and the ultimate moment capacity of a hull girder made up of the stiffened plates were analyzed. The results showed that MIG welding resulted in tensile and compressive residual stress of as much as 88% and 30% of the material yield strength, and a considerable level of distortion while residual stresses and distortions formed in the friction stir welding model were negligible. The load-shortening responses showed that extruded stiffened plates joined by FSW attained a 26% higher buckling load than the non-extruded stiffened plates joined by MIG fillet welding, which in turn resulted in a 28% higher ultimate moment capacity of the hull girder fabricated using FSW on extruded elements. The results also indicated that the presence of the residual stress and HAZ had the most significant effect on hull girders fabricated by MIG fillet welding on non-extruded plates where respective reductions of 10.5% and 7.5% in the ultimate moment capacity of the hull girders as a result of residual stresses and HAZ were observed.

8.2 Introduction

Accurate evaluation of the ultimate bending capacity of a hull structure is one of the critical aspects of ship design to guard against structural failure due to bending caused by hogging and sagging. One of the first methods for computing the ultimate longitudinal bending capacity of the ship hull girder was suggested by Caldwell (1965). In that method, the hull girder was divided into panels and the collapse load of each panel was calculated incorporating strength reduction factor due to buckling for compressive loading. However this method did not take into account the post-buckling strength of the panels which was little known at the time. With the development of understanding of post-buckling strength, Smith (1977) proposed a method where both the progressive failure and the post-buckling behaviour of the stiffened plates were considered in the ultimate capacity analysis. In this method, the hull girder structure was divided into a number of stiffened plates. The behaviour of these plates under compressive load can be characterized through so-called load-shortening curves. The moment vs. curvature relationship for the entire hull girder cross-section can then be determined by incrementally increasing the curvature and calculating resulting strains and stresses in the stiffened plates making up the cross-section using the predefined load-shortening curves.

Based on the general approach of Smith's method, several analytical models were proposed for determination of load-shortening curves of beam-column elements (Billingsley 1980; Dow et al. 1981; Adamchak 1984). Ueda et al. (1982, 1984) developed the Idealized Structural Unit Method (ISUM) which is similar to the Smith's beam-column method with the difference being that each ISUM element consisted of a large portion of the hull girder plating with multiple stiffeners. In the ISUM method the distribution of

residual stresses was often idealized in order to be included in the specific finite element formulas employed in the method. Consequently, the beam-column method is better suited to include the exact distribution of residual stress and distortion fields in the hull girder ultimate strength analysis (Gannon, 2011). These analytical methods for calculating ultimate bending capacity of ship hull girders have been shown to be effective provided that the load-shortening curves for an individual stiffened plate is accurate and influential factors affecting the response are taken into account properly. Given the fact that stiffened panels, either made of steel or aluminum, are constructed through welding, it is thus critical to include welding induced imperfections such as residual stresses and distortions in the development of the load-shortening curves. Yao and Nikolov (1991, 1992) developed a method for calculation of load-shortening curves of steel stiffened plate where the residual stresses and initial deflections of plate as well as the stiffener were considered. In the second paper, they improved the method further and included the combined torsional-flexural behaviour of the steel beam-columns. In a benchmark study, Ohtsubo and Sumi (2000) investigated the behaviour of steel stiffened plates and ultimate bending capacity of hull girders using different analytical methods. The results indicated that different assumptions and idealizations regarding the welding induced residual stresses and distortions contributed to differences in calculated stiffness and ultimate strength of stiffened plates. Gannon et al. (2012) investigated the effect of welding induced residual stresses and distortions on the load-shortening behaviour of steel tee-bar stiffened plates and the ultimate strength of a box girder. The results revealed that the residual stress reduced the ultimate strength of the stiffened plate by 11% and subsequently the ultimate moment capacity of the box girder by 3.3%.

The development in extrusion technology has made extruded aluminum stiffened plates an attractive alternative in the construction of aluminum hull girders. Aluminum plates with various cross-section shapes, made with extrusion technology in a single piece, can significantly reduce the number of welds, which will lead to less welding induced imperfections (Caseiro et al., 2013). In addition, a new fabrication method, friction stir welding (FSW), has become increasingly popular in welding of aluminum extrusions. A solid-state joining technology primarily used on aluminum, FSW has been shown to result in less welding induced residual stresses, heat affected zone (HAZ) and distortions in comparison with the metal inert gas welding, and consequently is expected to be beneficial to the ultimate strength of the hull girder. The combination of extrusion and FSW has then been increasingly used in construction of aluminum ship hull structures. However, there is little scientific information on the structural performance of hull girders built with extruded panels welded by FSW. In fact, available research on the structural performance of aluminum hull girders fabricated using either metal inert gas (MIG) welding or FSW on either extruded or non-extruded stiffened panels is limited. Several studies were reported on the effect of MIG welding induced residual stress and HAZ on the load-shortening behaviour of aluminum stiffened plates (Zha and Moan 2001, Rigo et al. 2003, SSC-460 2011). They showed that the effect of HAZ on the buckling load of stiffened plates was more predominant than that of residual stresses. However, the extents of effect differed in these studies. In the case of FSW on aluminum plates, finite element studies (Murphy et al. 2007, Yoon et al. 2009, Paulo et al. 2014) also showed that presence of HAZ and residual stress affected the ultimate strength of aluminum plates welded using FSW. However, the models they used were all simplified where the welding process was not

simulated. For example, Murphy et al. (2007) and Yoon et al. (2009) used shell elements and the effect of welding was assumed whereas Paulo et al. (2014) assumed the width of HAZ and distortions. Further to the limited research on the load-shortening behaviour of aluminum stiffened plates fabricated using FSW, no research has been conducted to investigate the effect of this fabrication method on the global hull girder strength.

In view of the above discussion, this study was thus motivated to investigate the effect of MIG welding and FSW on the ultimate strength of aluminum hull girders using either extruded or non-extruded elements. In this study, three fabrication methods were considered including 1) two extruded tee-bar aluminum stiffened plates joined together by FSW butt welding (FSW); 2) two extruded tee-bar aluminum stiffened plates joined together by metal inert gas butt welding (MIG butt) and 3) non-extruded aluminum tee-bar stiffened plates where two stiffeners are joined to the plates by the metal inert gas fillet welding (MIG Fillet). The welding process of either MIG or FSW was simulated using a three-dimensional, two-step sequential thermo-mechanical analysis to obtain the welding induced residual stresses, HAZ and distortions. Following the welding simulation, load-shortening curves of stiffened plates fabricated with three methods were generated under compressive loading incorporating the welding induced imperfections. Finally, the moment vs. curvature relationship of a box hull girder was determined using the Smith's method and the ultimate bending capacity of the girder as affected by the fabrication methods was examined.

8.3 Hull girder model

The hull girder cross-section used in this study is shown in Figure 8.1. It was selected to represent a large stiffened-panel structure representative of a typical high speed vessel. All stiffened plates were made of aluminum alloy 6082-T6, which is widely used in high speed vessels. The girder was divided into 44 sub-elements, of which 40 were composed of two stiffeners with the associated plating and remaining 4 were the corners of the hull girder. The dimensions of the sub-element stiffened plates are shown in Figure 8.2. The length of the stiffened plates was considered to be 1 m. For each stiffener and the associated plating, the resulting plate slenderness β is 2.285 and the column slenderness λ is 0.867, which is typical to aluminum ship structures. Three fabrication methods considered for the stiffened plates are reflected in Figure 8.3. Model "FSW" and "MIG butt" all consisted of two extruded tee-bar stiffened plates, each consisting of one stiffener and the associated plating, welded together in the longitudinal edges by either FSW or MIG butt weld. Model "MIG fillet" consisted of two tee-bar stiffeners attached to the plating by MIG fillet welds on both sides of the stiffeners.

The setup of FSW process used in this study was adopted from Guo et al. (2014). The plates were supported on a backing plate, and were clamped down along their length during welding. After the FSW process was complete and the model was cooled down to the room temperature, the clamps were released. The MIG butt welding input parameters including voltage/current and welding speed, were adopted from Lincoln Arc Welding Foundation (2000). Both sides of the plates were welded together in a single pass on each side. The plates were allowed to cool for 30 minutes after the welding of the upper side, and were cooled to 20 ºC following the welding of the lower side. The MIG fillet welding

parameters including welding current/voltage and the speed were in accordance with the American Welding Society Guide for Aluminum Hull Welding (AWS D3.7, 2004). The sequence of welding is indicated in Figure 8.3. After each of the weld lines, the model was allowed to cool down for 30 minutes and after the welding of all the weld lines, the model was allowed to cool down to room temperature.

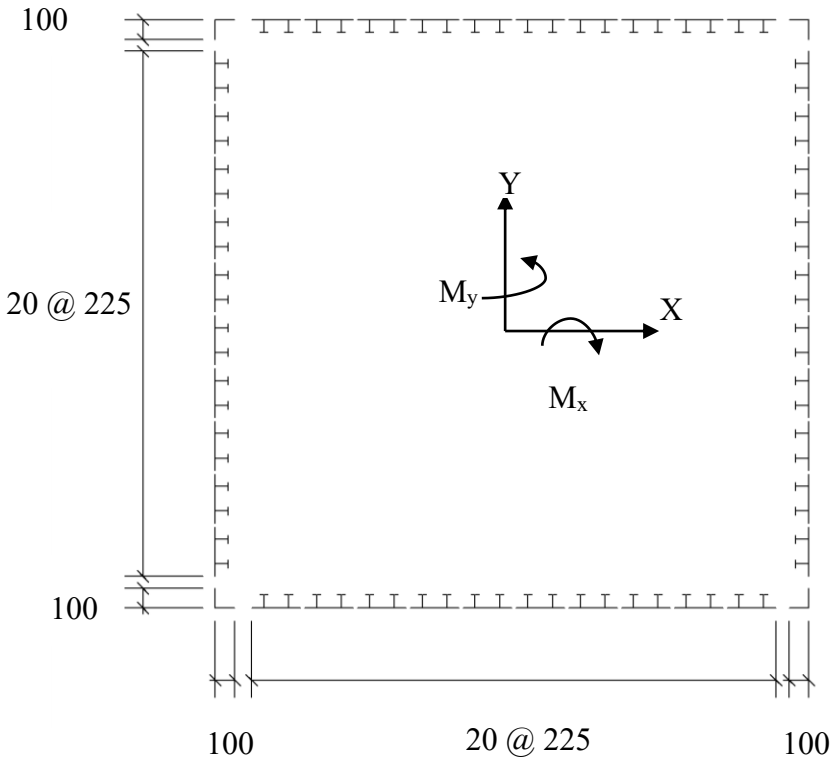

Figure 8.1 Hull girder cross-section (mm)

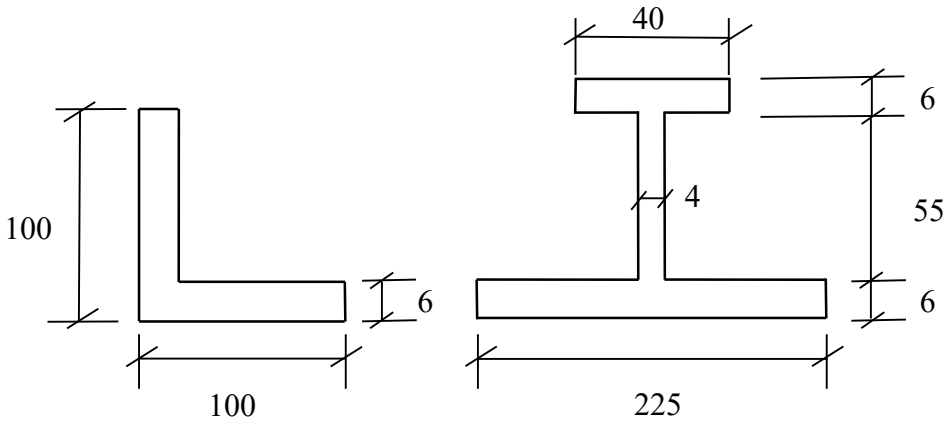

Figure 8.2 Units dimensions (mm)

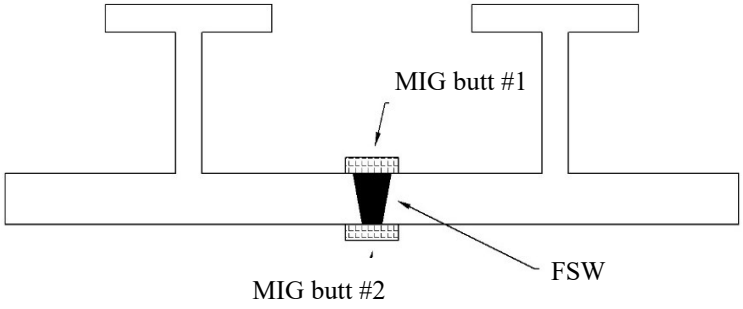

(a)

(b)

Figure 8.3 Weld lines (a) FSW and MIG butt welding (b) MIG fillet

8.4 Finite element simulation

8.4.1 General

A two-step thermal-mechanical procedure was used for the simulation of both FSW and MIG welding using ANSYS. In the first step of analysis, the thermal loads due to FSW and MIG welding were simulated and applied to the model and a nonlinear transient thermal analysis was performed to determine the time-dependent temperature distribution. In the second step, the temperature field history calculated from the thermal analysis, and also the plunging force in the case of FSW were applied to the structural model as a series of loads, where each load step represented an increment in the position of the traveling welding tool. A structural analysis was then performed to provide the residual stresses and distortions induced by the welding. The meshing patterns for both of the thermal and structural model were the same but with different element types. The SOLID70 thermal element was used in the thermal model whereas its equivalent structural element SOLID185 was used in the structural model.

Except for the material yield stress, all of the temperature dependent thermal and mechanical material properties for 6000 series of aluminum were adopted from from Riahi and Nazari (2011). The temperature dependent material yield stress was adopted from Eurocode 9 (1998). The temperature dependent heat transfer coefficient was adopted from Moraitis and Labeas (2008). A constant value of 0.33 was assumed for the Poisson's ratio through the temperature history. The temperature dependent thermal and mechanical material properties are shown in Figure 8.4.

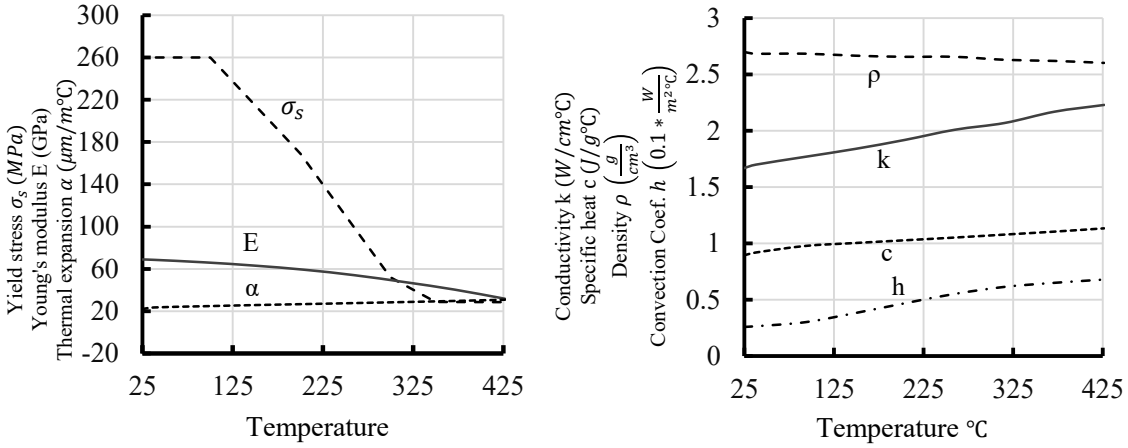

Figure 8.4 Temperature dependent material properties for aluminum alloy 6082-T6

A non-linear stress-strain relationship based on Ramberg-Osgood relation was used to model the AA6082-T6 material as shown in Eqn (8.1). Based on experimental data presented by Zha and Moan (2001), the 0.2% proof stress, σ_{02}, was taken as 260 MPa and the exponent, n, was taken as 46.

$$\varepsilon = \frac{\sigma}{E} + 0.002\left(\frac{\sigma}{\sigma_{0.2}}\right)^{n} \tag{8.1}$$

The development of HAZ due to the welding heat input was simulated based on the maximum temperature the elements experienced during the welding process. Three zones with different material strengths were defined, i.e., HAZ, semi-HAZ, and base metal zone. The correlation between the strength in these zones and temperature is summarized in Table 8.1. In the finite element analysis of both FSW and MIG welding processes, as welding progressed the average temperature of elements were queried and the material properties of those elements were changed corresponding to maximum temperature

according to Table 8.1 (DNV, 2013). This method is consistent with the finding of Sato et al. (1999) and Terasaki and Akiyama (2003) where it was shown that the aluminum reached its minimum hardness in the areas that experienced a temperatures above the 300 ^{o}C to 325 ^{o}C during the welding, and the areas that experienced a temperature between 200 ^{o}C and 300 ^{o}C obtained a hardness in between of the minimum hardness and the base metal hardness.

Table 8.1 Material strength with respect to temperature

	Temperature T	% of yield stress of base metal
HAZ	$T \geq 300\ ^{o}C$	53
Semi-HAZ	$200\ ^{o}C \leq T < 300\ ^{o}C$	76
Base metal zone	$T < 200\ ^{o}C$	100

The boundary conditions applied to the longitudinal edges of the plate were representative of the level of restraint in stiffened panels in ship hull girders. The longitudinal edges of all models were restrained to remain straight when moving in the plane, and free to move out of plane of the plating. (Dow et al. 1981, Gannon et al. 2012). In the transverse edges, simply supported boundary conditions were applied. The centroid of the each stiffener and the associated plating were restrained against displacements in all three direction in one end cross-section, and restrained against vertical and transverse direction in the other end cross-section.

8.4.2 Finite element simulation of MIG welding

The finite element meshing for the MIG butt model and fillet model is shown in Figure 8.5 and Figure 8.6 respectively. In both cases, a relatively dense meshing was used in the vicinity of the welding in order to accurately capture the temperature gradient and hence the thermal stresses and strains. In the areas away from the weld lines the number of the elements were decreased to increase the computing efficiency. It was also assumed that 60% of the total MIG welding heat input was transferred to the workpiece via the molten metal droplets and the remaining 40% via the surface heat fluxes (Pardo and Wekman 1989). For the surface heat source model, the angle of the torch was assumed to be normal to the surface of the weld. The total heat input of welding can be calculated using Eqn (8.2) as follows:

$$Q = \eta VI \tag{8.2}$$

where V is the arc voltage, I is the arc current, and η is the arc efficiency which is assumed to be 0.85 for CO_2 gas metal arc welding (Michaleris et al. 1997).

The heat of the molten metal droplets was described by a volumetric heat generation rate with uniform density. A Gaussian distribution relative to the coordinate system of the traveling heat source was assumed for the surface heat fluxes with the following expression:

$$q(x,\xi) = \frac{3Q}{\pi c^2} e^{-3x^2/c^2} e^{-3\xi^2/c^2} \tag{8.3}$$

where c is the radius of the welding arc. A user-defined macro was developed using ANSYS parametric design language (APDL) to simulate the moving of the heat source and the deposition of the molten metal droplets on the workpiece. The heat loss due to the combined effects of convection and radiation was taken into account by applying temperature dependent heat transfer coefficient (Figure 8.4) on the free surfaces of the work piece (Moraitis and Labeas 2008).

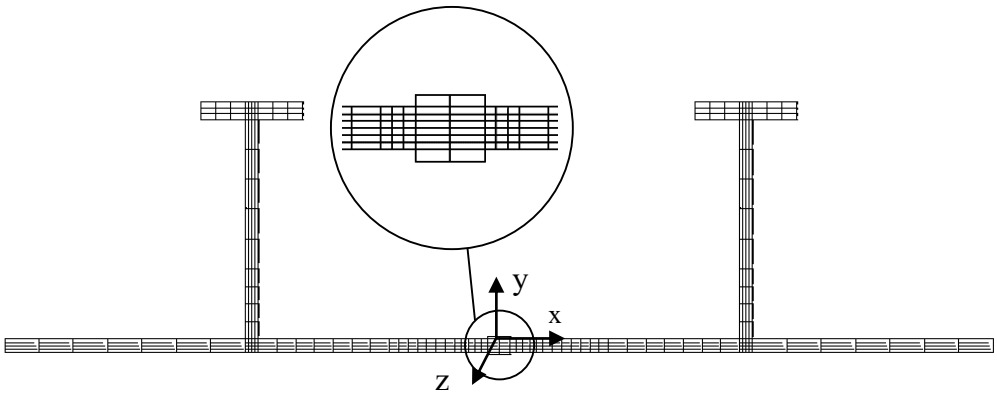

Figure 8.5 Finite element meshing of the model MIG butt

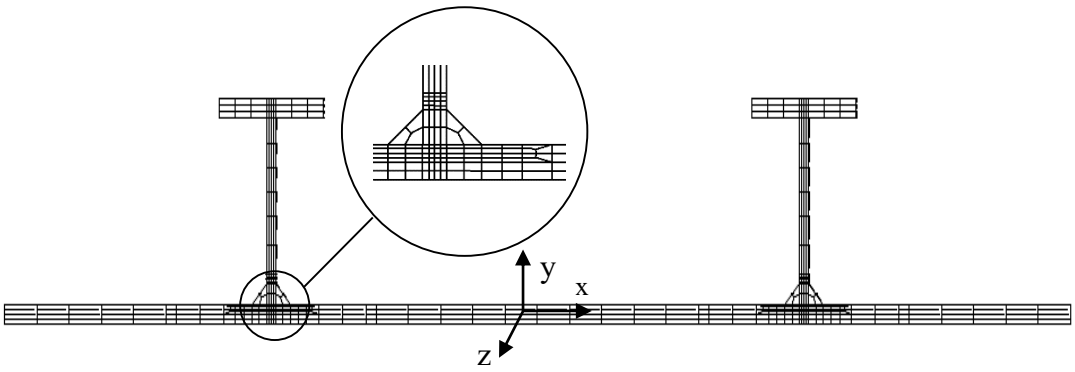

Figure 8.6 Finite element meshing of the model MIG fillet

In the structural analysis, the ANSYS element birth/death feature was implemented for accurately simulating the deposition of the molten metal droplets on the workpiece. In the beginning of the analysis all of the weld elements were deactivated (killed). As the welding torch progressed a user defined subroutine was used to apply the temperature field from the thermal analysis in the corresponding time. The average temperature of the deposited weld elements after the pass of weld torch was calculated and those whose temperature had fallen below the solidification temperature, which is 555 ^{o}C for aluminum alloy 6082-T6, were activated to simulate the deposition of the molten weld metal droplets on the workpiece. In the case of MIG fillet models, spring elements were assigned at the interface of the stiffeners and the plate to allow the separation and sliding of the stiffener on the plate surface before deposition of the weld metals. The rest of the process remained the same for both MIG butt and fillet models as described above.

The MIG model was verified using experimental test results of Masubuchi (1980). The geometry and boundary condition of the test is shown in Figure 8.7. The plate was made of aluminum alloy 5052-H32 and the upper edge of the plate was welded by MIG welding. The welding parameters were given by Masubuchi (1980).

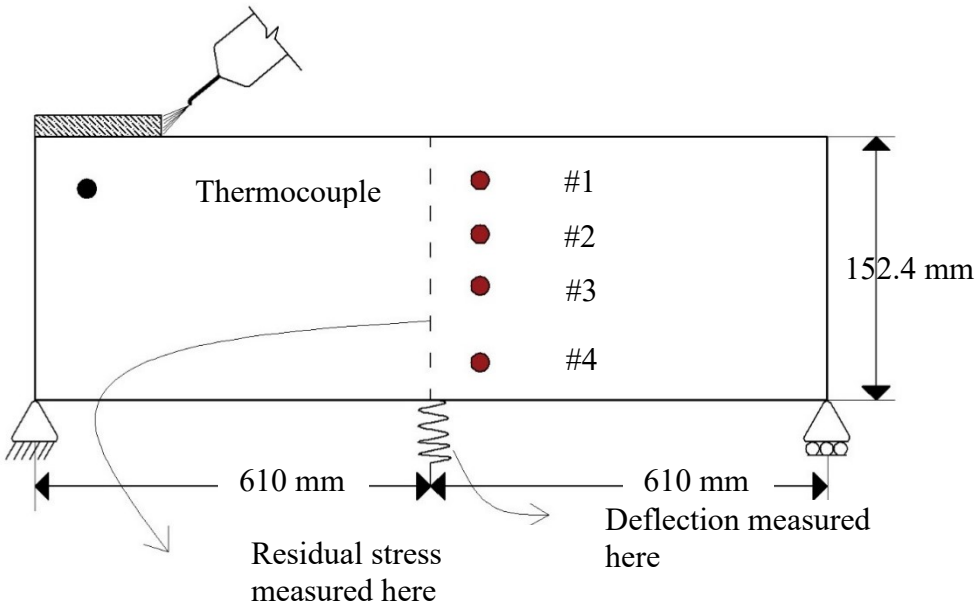

Figure 8.7 Test setup of Masubuchi (1980)

Figure 8.8 compares the temperature history whereas Figure 8.9 compares the transient vertical deflection and the longitudinal residual stresses, all obtained at the mid-span and mid-thickness of the plate. Both figures show that the finite element model provides reasonably accurate results in both temperature distribution and the resulting deformation and residual stress for welding in aluminum plates.

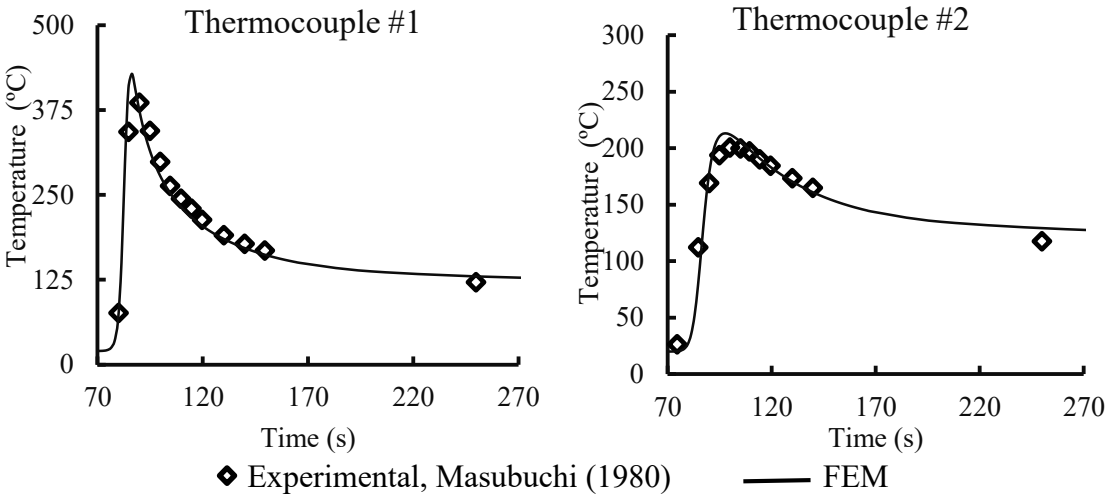

Figure 8.8 Comparison of temperature history at thermocouples

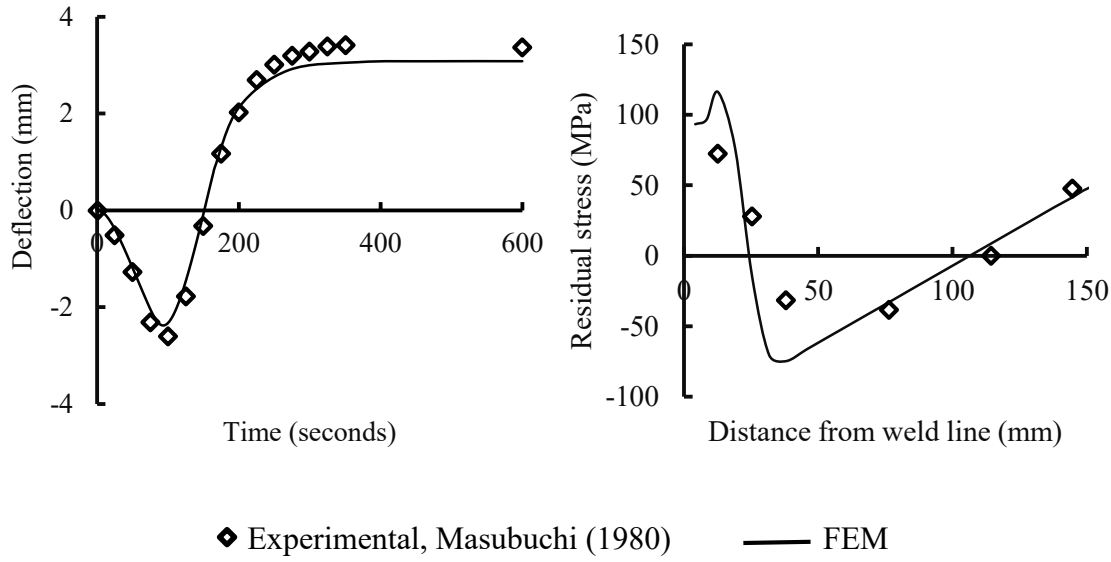

Figure 8.9 Comparison of transient vertical deflection and longitudinal residual stress at the mid-thickness of the plate

8.4.3 Finite element simulation of FSW

The finite element meshing of the FSW model is shown in Figure 8.10 and the FSW process is shown in Figure 8.11. The weld zone in the friction stir welding was defined as the interface of the workpiece and the welding tool. The total heat generated in watts (W) by FSW was considered to consist of three components including heat generated at the interface of the tool shoulder and workpiece, $Q_{shoulder}$; the heat generated from the side surface of the pin, $Q_{pin,side}$, and on the tip of the pin, $Q_{pin,tip}$. The expressions for each term was given by Schmidt et al. (2004) as:

$$Q_{shoulder} = \int_0^{2\pi} \int_{R_{pin}}^{R_{shoulder}} \omega \tau_{contact} r^2 dr d\theta \tag{8.4}$$

$$Q_{pin,side} = \int_0^{2\pi} \int_0^{h_{pin}} \omega \tau_{contact} {R_{pin}}^2 dz d\theta \tag{8.5}$$

$$Q_{pin,tip} = \int_0^{2\pi} \int_0^{r_{pin}} \omega \tau_{contact} r^2 dr d\theta \tag{8.6}$$

where $\tau_{contact}$ is the shear stress in the surface, r is the radius of shoulder as shown in Figure 8.11 and ω is the angular velocity. The heat input distribution was assumed to be linearly proportional to the distance from the tool centerline to the edge of the shoulder. The generated heat were applied to the materials under the tool with a distribution given by Chao et al. (2003):

$$q(r) = \frac{3Q_f r}{2\pi R_{shoulder}^3} \tag{8.7}$$

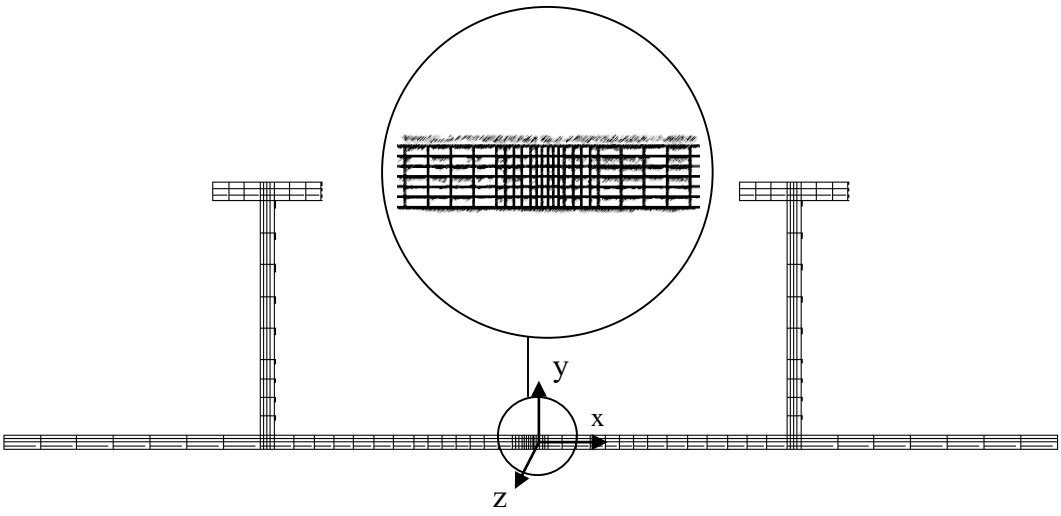

Figure 8.10 Finite element meshing of the model FSW

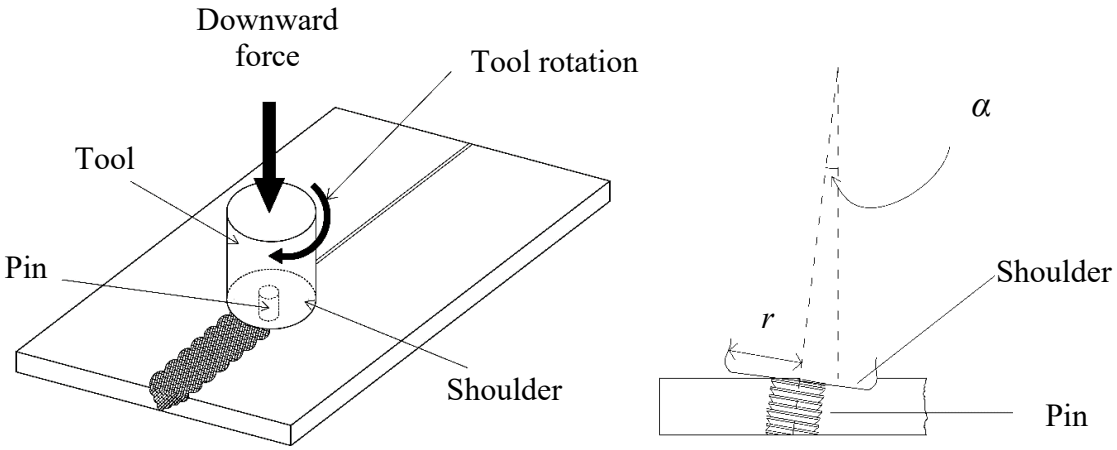

Figure 8.11 FSW process

where $R_{shoulder}$ is the outside radius of the shoulder of the tool and Q_f is the total heat input. The heat loss due to convection and radiation was accounted for by applying a temperature dependent heat transfer coefficient (Figure 8.4) on the free surfaces of the work piece. For

the bottom surface of the plate which was in direct contact with the backing plate the conduction condition was evaluated as:

$$Q_b = \beta_b (T - T_0) \tag{8.8}$$

where β_b is the convection coefficient between the workpiece surface and the backing plate and it is assumed to be $350 W/m^2 K$ based on the work of Chao et al. (2003).

In the mechanical analysis of the FSW, two types of loading were applied. These were the temperature field history calculated in the thermal analysis and the plunging force applied from the welding tool to the workpiece. The plunging force was applied to the model as a uniform pressure moving forward with the speed of the welding. The release of clamps was considered in the model to allow the redistribution of stresses and strains.

The FSW model was verified using experimental test results of Zhu and Chao (2004) on steel plates joined together by FSW as well as results of Guo et al. (2014) on aluminum plates joined together by FSW. The experimental setup of Zhu and Chao (2004) involved two 304L stainless steel plates measuring 304.8 mm long, 101.6 mm wide and 3.18 mm thick each, being joined by FSW along the length of the plates. The setup of Guo et al. (2014) consisted of a plate of aluminum alloy 6061 being welded to a plate of aluminum alloy 7075, measuring 300 mm long, 50 mm wide and 6.4 mm thick each. Figure 8.12 and Figure 8.13 compare the finite element and experimental results by Zhu and Chao (2004) for the temperature distribution and residual stress distribution along the transverse direction of the workpiece, respectively. Also included are the numerical results obtained by Zhu and Chao (2004) before and after the clamps release. As Figure 8.13

shows, the residual stress decreases significantly after the release of the clamps. Figure 8.14 shows the comparison of the finite element and the experimental thermal results of Guo et al. (2014). No experimental residual stress results were reported. In both cases, good agreement between the finite element and experimental results was obtained, indicating that the model developed is capable of simulating FSW and its effect on aluminum alloy.

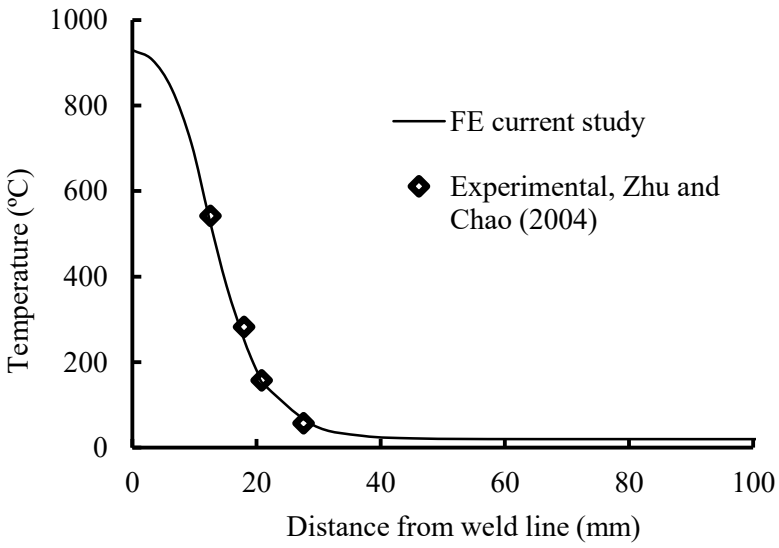

Figure 8.12 Comparison of temperature distribution along the transverse direction

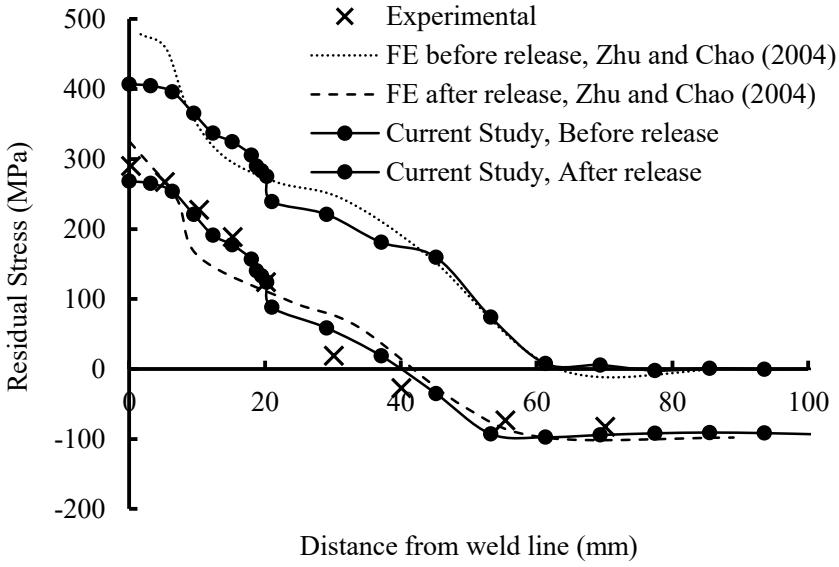

Figure 8.13 Longitudinal residual stress along the cross-section

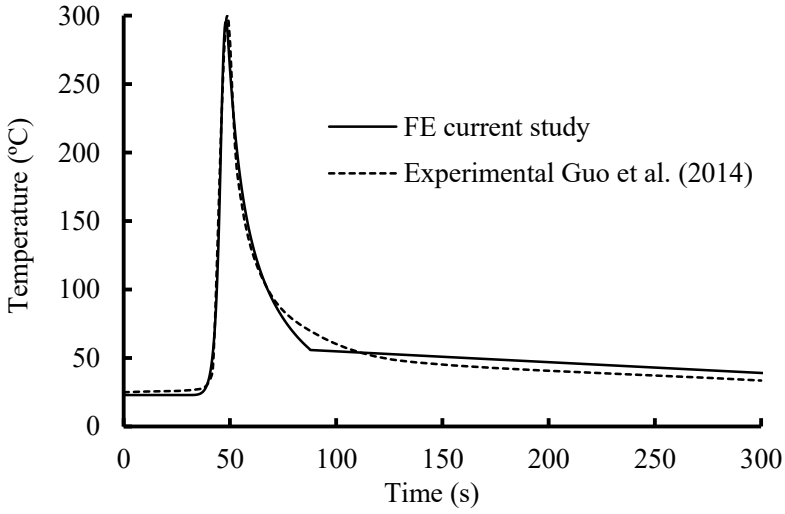

Figure 8.14 Comparison of temperature history profile at 10 mm away from the weld line

8.5 Welding induced Residual stresses, HAZ and distortions

In this study, the residual stresses of MIG models were reported after the model was cooled down to the room temperature and those of FSW model were reported after the release of the clamps. Welding induced longitudinal residual stresses obtained at the mid-thickness in the mid-length of the models are shown in Figure 8.15 for the plating. For all models the tensile residual stresses were developed around the weld line and they were balanced by the compressive residual stresses away from the weld line. The FSW resulted in significantly lower tensile and compressive residual stresses in comparison with the MIG welding. The maximum tensile residual stress in FSW model was 66 MPa, located 7.5 mm away from the weld center-line where the tensile residual stress was 42 MPa. The compressive residual stress of the FSW model was 4 MPa. In comparison, the maximum tensile residual stress of the MIG butt welding was 229 MPa, which was the highest among all three models, and was located 24 mm away from the weld line where the tensile residual stress was 178 MPa. The compressive residual stress in the MIG butt welding model was about 33 MPa. In the MIG fillet welding model the tensile residual stress formed in the location of the stiffeners with the maximum value of 167 MPa. The maximum compressive residual stress was the highest among all three models with a value of 78 MPa and located in the plating between the two stiffeners. The results also revealed that the width of the HAZ around the weld line was 18, 30 and 40 mm for FSW, MIG butt and MIG fillet welding models, respectively. Note that while in FSW and MIG butt welding a single HAZ was formed, in MIG fillet model the HAZ was formed in two stiffener areas.

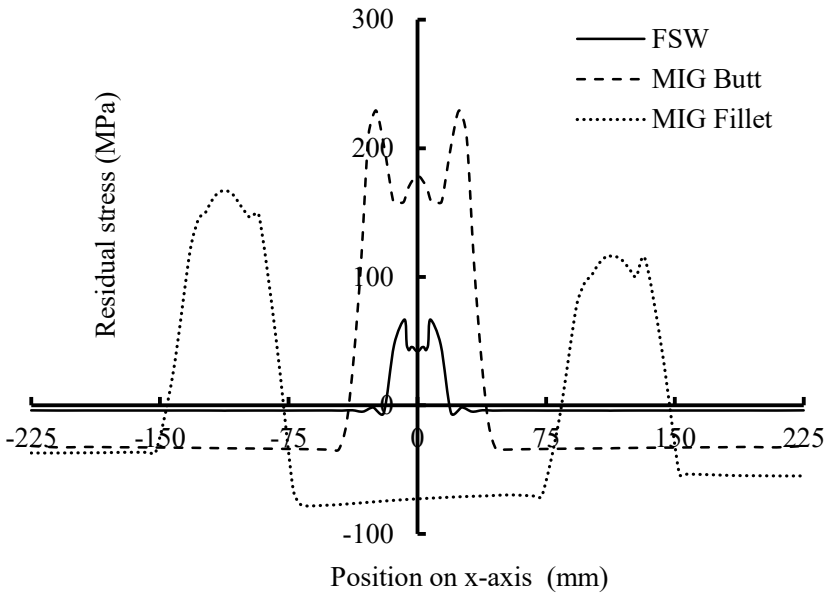

Figure 8.15 Longitudinal residual stress at the mid-thickness of the plate

The vertical deflections of the plates along the x axis as well as the z axis obtained at the mid-length of models are shown in Figure 8.16. The vertical deflection induced by FSW was almost negligible with a maximum value about 0.25 mm. The low level of the FSW induced deflections is attributed to the low level of the temperature gradient and also the clamping of the model during the welding process. The vertical deflection caused by MIG butt welding in the mid-length of the model along the x axis was almost uniform at about 1 mm. The maximum vertical deflection in the mid-length along x axis occurred in MIG fillet models and was 1.63 mm at the center between two stiffeners. In the case of the vertical deflection along the z direction obtained at the mid-width of models, the MIG fillet welding caused an almost uniform deflection with an average magnitude of 1.68 mm, while the average value of the MIG butt model was about 1.10 mm.

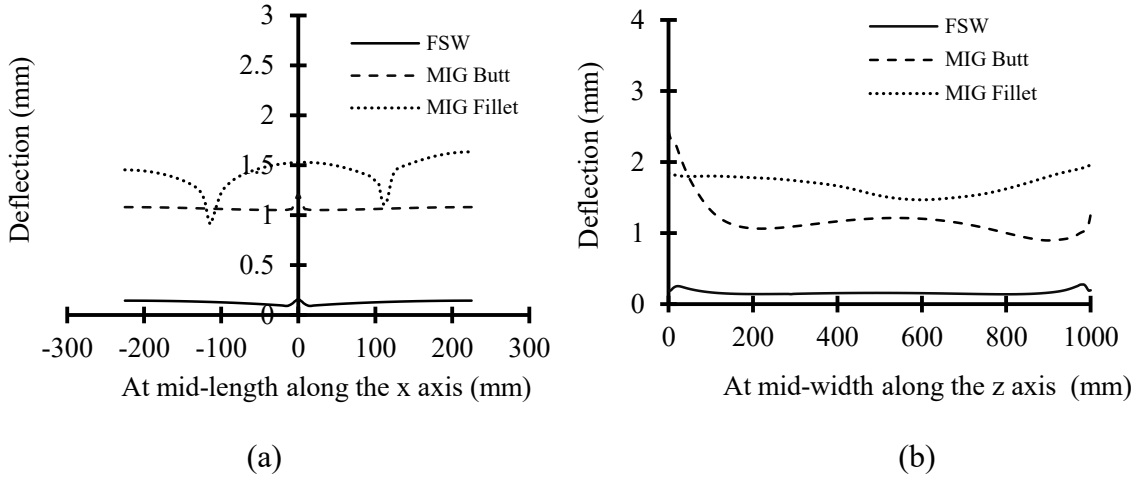

Figure 8.16 Vertical deflection of plate (a) along the x axis at model mid-length (b) along the z axis at model mid-width

8.6 Behaviour of stiffened plates under compressive loading

Following the simulation of the welding process, the load-shortening behaviour of each model under compressive loading was obtained. To obtain the post-buckling behaviour of the model, a displacement controlled analysis was performed where a displacement was applied to the centroids of each stiffened plate on one end of each model and the reaction force was calculated at the centroid on the other end. To ensure that the compressive loading was uniformly distributed over the entire cross-section and the cross-sections would remain plane during the ultimate strength analysis, beam elements with high bending and low axial stiffness were used to connect all nodes at each end cross-section of the stiffened plates at each end to the centroidal node of the each end cross-section. These elements were made inactive during the welding simulation and then

activated for the ultimate strength analysis using the ANSYS element birth and death feature.

Figure 8.17 plots the load-shortening curves of all three models. It shows that the FSW model of extruded elements attained the highest ultimate strength with a value of 810 kN. The MIG fillet model where the stiffeners were welded to the plate had the lowest ultimate strength with a value of 640 kN while the MIG butt model of extruded elements attained ultimate strength somewhere in between with a value of 741 kN. This suggests that using extruded elements and FSW welding resulted in an increase in ultimate strength by as much as 26% when compared with non-extruded elements fabricated using MIG welding. The high ultimate strength in the FSW model is attributed to low level of residual stress, small HAZ width and distortions resulting from FSW comparing with MIG welding. The fact that there are two welding regions in MIG fillet model caused this model to have even lower strength than MIG butt model. Figure 8.17 also shows that welding method or using extruded or non-extruded elements does not affect the pre-buckling stiffness and all three models had almost identical pre-buckling slope. The FSW model experienced a sharp and sudden drop in the load carrying capacity after buckling, while the drop for MIG models was more gradual beyond the buckling point. This is consistent with the results of Gannon et al. (2012) and Gordo and Guedes Soares (1993) where it was shown that the presence of residual stresses and distortions in plates suppressed the sudden drop in load carrying capacity after the ultimate load was reached in nearly perfect plates. Where the post-buckling behaviour is concerned, the FSW and MIG butt models with extruded elements had almost identical post-buckling behaviour whereas MIG fillet model showed a similar trend in the post-buckling region but at a markedly lower strength.

A comparison of the buckling modes revealed that all three models collapsed by the plate buckling mode, indicating that using either welding methods or using extruded or non-extruded elements did not affect the buckling mode. The buckled shape of the MIG fillet model is shown in Figure 8.18.

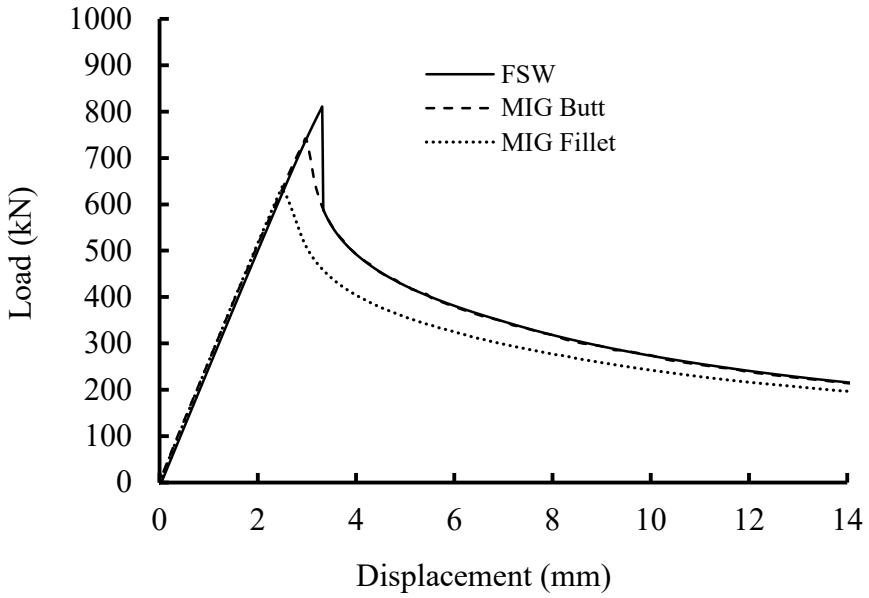

Figure 8.17 Load-shortening curves of the models fabricated by different methods

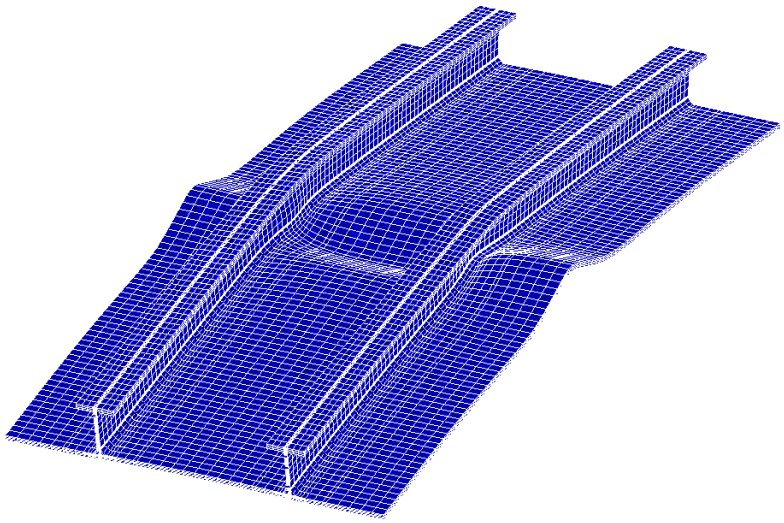

Figure 8.18 Post-ultimate deformed shape of MIG fillet model

To investigate the effect of welding induced residual stresses and HAZ on the load-shortening behaviour of the models joined by MIG welding, the MIG butt and MIG fillet models were analyzed for the second time by including the residual stress and distortion fields but without the HAZ and the third time by including the HAZ and distortion fields but without the residual stresses. The results are shown in Figure 8.19. For the MIG fillet model the presence of residual stresses and HAZ reduced the buckling load of stiffened plates by 6% and 0.3% respectively. However, the HAZ showed a more significant reduction on the post-buckling strength. On the other hand, the extruded model welded by MIG butt welding showed less sensitivity to the residual stresses and HAZ where the buckling load was reduced by 2.7% and 0.3% due to the presence of the residual stress and HAZ respectively. However, pre-buckling and post-buckling behaviour of the MIG butt welding models remained almost the same.

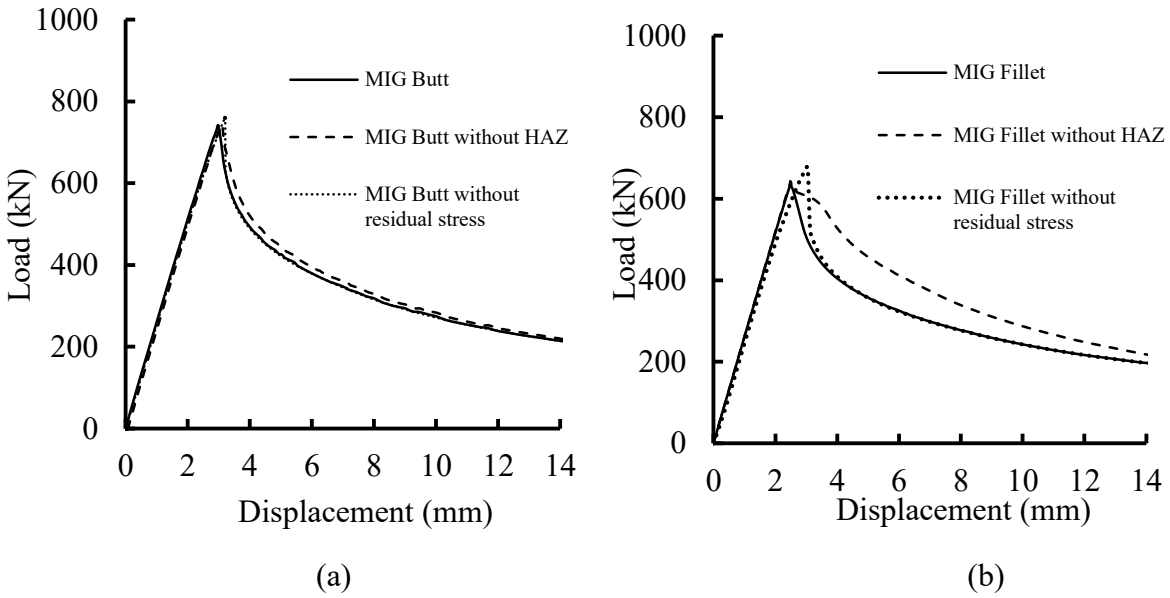

Figure 8.19 Effect of welding induced HAZ and residual stress on the load shortening of the models joined by (a) MIG butt welding (b) MIG fillet welding

8.7 Hull girder ultimate strength

8.7.1 Description of method

In this study, the Smith's method was used to obtain the moment vs. curvature relationship and thus the ultimate moment capacity of the hull girder. In this method, the cross-section of the hull girder is divided into individual beam-column components; each consisting of a stiffener and an associated width of attached plating. For an increment of curvature applied to the hull girder the average strain of each beam-column element is calculated based on its location relative to the neutral axis. Entering these values in the predefined load-shortening curves of each element, the associated stress state and the load carrying capacity of each element is calculated. Then the bending moment resisted by the

cross-section is obtained from the summation of the contributions from the individual elements.

In the first step of the Smith's method, the neutral axis of the cross-section is determined through an elastic analysis. The initial neutral axis crosses the centroid point of the cross-section. The coordinates of this point is:

$$\begin{cases} \bar{x} = \dfrac{\Sigma x_i A_i}{\Sigma A_i} \\ \bar{y} = \dfrac{\Sigma y_i A_i}{\Sigma A_i} \end{cases} \tag{8.9}$$

where A_i is the area of the i^{th} element, and x_i and y_i are the distance of the centroid of the i^{th} element from the base lines. In general cases, the ship is subjected to curvatures in both of the X and Y directions, denoted as C_X and C_Y. The global curvature C is related to these two components:

$$C = \sqrt{C_X{}^2 + C_Y{}^2} \tag{8.10}$$

or:

$$\begin{cases} C_X = C.\cos\theta \\ C_Y = C.\sin\theta \end{cases} \tag{8.11}$$

where θ is the angle between the neutral axis and X axis. The strain ε_i at the centroid of the i^{th} element is ε_i which depends on its position and on the hull curvature, is given by:

$$\varepsilon_i = C.(y_{gi}.\cos\theta - x_{gi}.\sin\theta) \tag{8.12}$$

where x_{gi} and y_{gi} are the coordinates of the centroid element *i* with respect to the centroid point of the cross-section. Once the strain in each of the beam-column elements is determined, the corresponding stress can be obtained from the load-shortening curves. Consequently, for a curvature of *C,* the components of the total bending moment about the principal axis are given by:

$$\begin{cases} M_X = \sum y_{gi}.\Phi(\varepsilon_i).\sigma_0 A_i \\ M_Y = \sum x_{gi}.\Phi(\varepsilon_i).\sigma_0 A_i \end{cases} \tag{8.13}$$

where $\Phi(\varepsilon_i)$ represents the non-dimensional strength of the i^{th} element at a strain of ε_i, the average stress of the beam-column element normalized by the yield stress. The bending moment on the cross-section about the instantaneous center of gravity is then:

$$M = \sqrt{{M_X}^2 + {M_Y}^2} \tag{8.14}$$

One of the complication of this method is that although in the beginning the initial neutral axis is the same as the elastic neutral axis, during the stepwise process as the curvature increases and elements fail through the buckling, or in the case of aluminum as the tensile stress strain relation becomes nonlinear, the location of the neutral axis will shift and an iterative approach is required. The new position of the neutral axis is calculated using the effective area of each element given by:

$$A_{ei} = \varphi.A_i \tag{8.15}$$

where φ is the deviation of the element from perfectly plastic behaviour, given by:

$$\varphi = \frac{\bar{\sigma}}{\bar{\varepsilon}} = \frac{(\frac{\sigma}{\sigma_y})}{(\frac{\varepsilon}{\varepsilon_y})} \tag{8.16}$$

and the position of the neutral axis is then given by:

$$\begin{cases} \bar{x} = \dfrac{\Sigma x_i A_{ei}}{\Sigma A_{ei}} \\ \bar{y} = \dfrac{\Sigma y_i A_{ei}}{\Sigma A_{ei}} \end{cases} \tag{8.17}$$

As A_{ei} is dependent on the position of the centroid point of the cross section, Eqns. (8.9) through (8.17) should be implemented repeatedly to determine the position of the neutral axis until a convergence is reached.

8.7.2 Ultimate strength

Figure 8.20 plots the resulting moment vs. curvature relationships for all three models. It shows that fabrication methods had a marked influence on the ultimate strength of the hull girder. The FSW model attained the highest moment capacity with a value of 52.3 MN-m, which represented a 28% increase from the moment capacity of 40.8 MN-m obtained by the MIG fillet model and a 9% increase from 47.8 MN-m obtained by MIG butt model. This indicates that the combination of extruded plates welded by FSW is the most desirable fabrication method for providing the highest moment capacity. In the case of MIG welding, the MIG butt model with extruded plates attained 17% higher moment

capacity than that of the MIG fillet model with non-extruded plates. Figure 8.20 also shows that there was a sudden change in the slope of the FSW model at a curvature of about 0.0014 which coincided with the buckling of the stiffened plates located at the top of the hull girder. When the top units of the hull girder reached the buckling strain, the neutral axis shifted downward in the cross-section to maintain the force equilibrium and the hull girder experienced a sudden and sharp drop in the moment capacity. On the other hand, the MIG models had a smoother moment vs. curvature curves in the post-buckling region. This behaviour is consistent with the response observed in the load-shortening curves described in the previous section where the curves for FSW model had a more pronounced drop then the other two models. This further confirms that the presence of residual stress and distortion "soften" the sudden capacity drop in the post-buckling region.

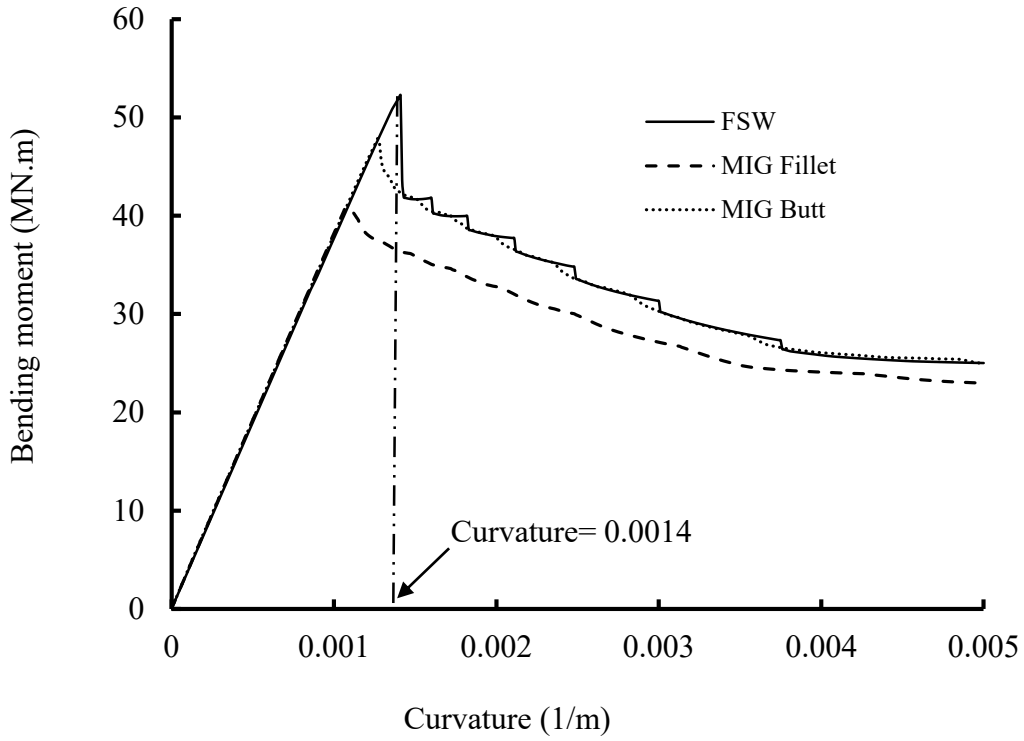

Figure 8.20 Moment vs. curvature curves of the models with different fabrication methods

To further study the effect of the MIG welding induced residual stress and HAZ on the ultimate moment capacity of the hull girder, the moment vs. curvature curves for the hull girder fabricated with MIG fillet and MIG butt plate elements were obtained without effect of either residual stresses or HAZ. In this case, the load-shortening curves for the MIG models without taking into account of either the HAZ or the residual stress as described in the previous sections, were used in the Smith's method. The resulting moment vs. curvature curves are shown in Figure 8.21. As shown, in the hull girder made of MIG fillet model, the presence of HAZ decreased the ultimate moment capacity by 7.5% and caused an offset in the post-ultimate region of the moment vs. curvature curve. The

presence of residual stresses decreased the ultimate moment capacity by 10.5%. However, it showed no significant effect on the post-ultimate behaviour of the model. For the hull girder made of the MIG butt model, the results indicate that the presence of the residual stresses and HAZ had little effect on the ultimate moment capacity and the behaviour of the hull girder. The reductions in the ultimate moment capacity due to residual stresses and HAZ were 3.5% and 0.5% respectively. This suggests that for extruded plates joined by MIG butt welds, the effect of residual stress and HAZ is insignificant in the moment capacity calculation; on the other hand, if conventional the fabrication method is employed where stiffeners are fillet welded to the plates, ignoring either residual stresses or HAZ will result in an unsafe estimate of moment capacity of the hull girder.

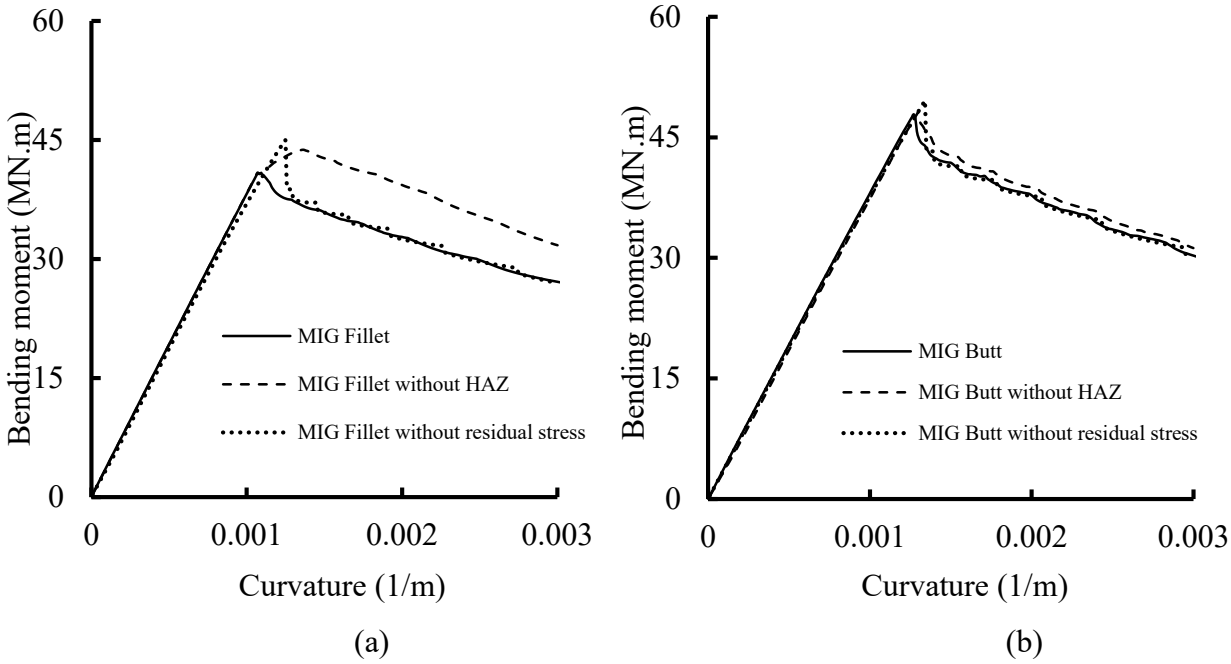

Figure 8.21 Effect of welding induced HAZ and residual stress on the moment vs. curvature of the models (a) MIG fillet (b) MIG butt

8.8 Conclusions

A finite element model was developed to simulate the welding of extruded and non-extruded aluminum tee-bar stiffened plates joined together by friction stir welding, metal inert gas butt welding and metal inert gas fillet welding. The resulting residual stresses, distortions and heat affected zone were discussed for the three fabrication methods. The load-shortening behaviour of the stiffened plates was also obtained, which were used in a subsequent ultimate strength analysis of a hull girder using the Smith's method. The conclusions of this study are summarized in the following.

1. The maximum tensile residual stress induced by MIG butt welding, MIG fillet welding and FSW was 64, 88 and 25% of the yield stress of the aluminum alloy 6082-T6, respectively. In the case of the compressive residual stress the highest magnitude was developed in the MIG fillet model which was 30% of the yield stress of the aluminum alloy 6082-T6. The compressive residual stress induced by the FSW was negligible.
2. For welding induced HAZ, the models with FSW, MIG butt and MIG fillet welding attained a HAZ width of 3, 5 and 6.6 times the plate thickness, respectively. In the case of the welding induced distortions, the non-extruded model fabricate by MIG fillet welding had the highest distortion while it was negligible for extruded elements joined by FSW.
3. In terms of load-shortening behaviour, the extruded stiffened plates welded by FSW attained the highest ultimate strength, which was 9% higher than that for the MIG butt welded model. When the MIG welding is considered, using extruded elements joined by butt welding instead of non-extruded stiffened plates joined by

fillet welding resulted in an increase in the ultimate strength by 16%. The analysis of the models joined by MIG welding showed that the presence of the residual stress and HAZ decreased the ultimate strength by as much as 6% and 0.3% respectively.

4. The hull girder ultimate moment analysis revealed that the model with extruded elements welded by FSW had a 28% higher ultimate moment than that of the model with non-extruded elements welded by MIG welding. Within the models joined by MIG, the girder made of butt welding model had a 17% higher moment capacity than the fillet welding model. Using extruded plates joined by MIG butt welds, the effect of residual stress and HAZ was insignificant in the moment capacity calculation. However, when stiffened plates were constructed by fillet welding stiffeners to the parent plates, ignoring either residual stresses or HAZ overestimated the moment capacity of the hull girder by 10.5% and 7.5% respectively.

Chapter 9 - **Summary and conclusions**

9.1 Summary

A finite element model was developed to simulate the friction stir welding (FSW) and metal inert gas (MIG) welding processes in aluminum plates and stiffened plates. The product of the simulation was welding induced imperfections including residual stress and distortion fields, and heat affected zone. The imperfections as a result of both FSW and MIG welding were studied and compared. In addition, the effect of clamping area and welding speed on the FSW induced residual stress was investigated. Following the verification of the model, the load-shortening curves were obtained to study the effect of using FSW and MIG welding on the behaviour and ultimate buckling load of the aluminum stiffened plates. The obtained load-shortening curves were used in the ultimate strength analysis of an aluminum hull girder using the Smith's method. The effect of different fabrication methods as well as the effect of welding induced residual stress and HAZ associated with these methods on the ultimate strength of the hull girder were obtained and discussed. Conclusions drawn from the results of this research are summarized in the following.

9.2 Welding induced residual stress, distortion and HAZ

- In both of the FSW and MIG welding the maximum tensile residual stress occurred at the edges of the HAZ. While the thickness of the plates did not have a significant

effect on the magnitude of the residual stresses caused by FSW, for MIG welding the residual stresses increased as the plates became thicker.

- The structural results revealed that for all models studied, FSW resulted in up to 40% lower peak tensile and 75% lower peak compressive residual stress in comparison with MIG welding.
- The MIG welding resulted in a wider HAZ than the FSW process. For the models considered, the extent of HAZ as a result of MIG welding was about 1.5 to 2.5 times that caused by FSW process.
- MIG welding resulted in a considerable level of distortion in both transverse and longitudinal directions and this distortion increased as the plate thickness decreased. In comparison, the distortions due to FSW process were almost negligible.

9.3 Effect of MIG welding on the behaviour and strength of aluminum stiffened plates

- Maximum tensile residual stress developed in the plate due to welding ranged between 72 to 77% of the base metal yield stress while the compressive residual stresses ranged between 18 to 36% of the base metal yield stress.
- The total width of the HAZ of the plate in various models ranged between 26 to 56 mm depending on the thickness of the plate, with thinner plates having larger HAZ width.

- For a given plate slenderness, an increase in the column slenderness resulted in an increase in the vertical distortion. For a given column slenderness, the thinner the plates, the larger the distortion. Overall, the maximum value of the vertical distortion of all models at the mid-width was around 2.5 mm.
- The ultimate strength decreased due to the presence of the longitudinal and transverse HAZ by as much as 10%. The ultimate strength reduction due to the presence of the residual stresses was as much as 16.5%.
- The comparison with the existing analytical methods shows that DNV Rules for Classification of High Speed, Light Craft and Naval Surface Craft (2013), on average, underestimated the ultimate strength of aluminum stiffened plates by as much as 48% with a mean of 27%.

9.4 Effect of clamping area and welding speed on the FSW induced residual stresses

- Increasing the clamping area was shown to reduce the magnitude of tensile residual stress. The maximum reduction observed was about 40% when the clamping-to-plate width ratio increased from 0.5 to 0.8.
- Welding speed had more pronounced effect on models with large clamping area than those with small clamping area. For models with large clamping areas, an increase in the welding speed resulted in as much as 60% increase in the tensile residual stress and the tensile residual stress distributed in a narrower region. For models with small clamping area which had a tensile residual stress about the yield

stress of the material in HAZ, an increases in welding speed did not result in significant change in the magnitude of the tensile residual stress.

9.5 Ultimate strength of extruded aluminum stiffened plates joined by either FSW or MIG

- FSW process resulted in a maximum tensile residual stress of about 25% of the material yield stress and a negligible compressive residual stress. MIG welding caused a maximum tensile residual stress of about 88% of the yield stress and a compressive residual stress of about 10% of the yield stress.
- The heat affected zone due to FSW extended 9 mm from the weld center-line in each direction compared to a width of 15 mm for the MIG welding.
- Joining the extruded aluminum stiffened plates using either FSW or MIG welding did not have significant effect on the pre-buckling and post-buckling strength and buckling mode.
- In the models with relatively small plate slenderness, using the FSW increased the ultimate strength by as much as 9% in comparison with models welded by MIG welding.
- For the models with greater plate slenderness, using the MIG welding instead of FSW, increased the ultimate strength by as much as 3%.

9.6 Effect of fabrication methods on the ultimate strength of aluminum hull girders

- Using extruded elements with MIG butt welding instead of non-extruded elements with MIG fillet welding can increase the ultimate strength of aluminum stiffened plates by 16%.
- Using extruded elements with FSW instead of non-extruded elements with MIG fillet welding can increase the ultimate strength of aluminum stiffened plates by 26%.
- Residual stresses and HAZ can reduce the ultimate moment capacity of the simplified hull girder by 10.5% and 7.5%, respectively. Hence, residual stresses should not be ignored in the analysis of aluminum stiffened plates.
- Using extruded elements with FSW instead of non-extruded elements with MIG fillet welding can increase the ultimate moment of the aluminum hull girder by as much as 28%.

9.7 Recommendation for future work

The following suggestions are recommended for further investigations in order to gain a better understanding of the effect of welding and fabrication methods on the structural behaviour of aluminum ships.

- The welding induced imperfections and their effect on the structural performance of aluminum stiffened plates welded by FSW fillet welds.

- The structural performance of flat-bar and angle-bar aluminum stiffened plates with geometry typical to aluminum vessels welded by MIG welding.
- Behaviour and ultimate strength analysis of a hull girder with realistic cross-section configurations.
- The fatigue behaviour and strength of aluminum stiffened plates welded by FSW or MIG welding.

References

Aalberg A, Langseth M, Larsen P K. (2001). Stiffened aluminium panels subjected to axial compression. Thin-Walled Structures. 39: 861-885.

ABS. (2007). Guide for Building and Classing High-Speed Naval Craft. American Bureau of Shipping, January.

Adamchack JC. (1984). An approximate method for estimating the collapse of a ship's hull in preliminary design. SNAME Ship Structure Symposium. (pp. 37-61).

Anderson AF. (2000). Residual stresses and deformations in steel structures. PhD Thesis, Department of naval architecture and offshore engineering, Technical University of Denmark.

AWS, D3.7. (2004). Guide for Aluminum Hull Welding. American Welding Society.

Bai Y, Bendiksen E, Pedersen PT. (1993). Collapse analysis of ship hulls. Marine Structures. 6: 485-507.

Bastier A., Maitournam MH, Roger F, Van KD. (2008). Modelling of the residual state of friction stir welded plates. Journal of Material Processing Technology. 200: 25–37.

Beaulieu D. (2006). Design of aluminum structures. 1th ed. Saguenay: Pral.

Bhatti MA. (2005). Fundamental Finite Element Analysis and Applications. Hoboken, New Jersey: John Wiley & Sons, Inc.

Billingsley DW. (1980). Hull girder response to extreme bending moments. SNAME 5th Star Symposium (pp. 51-63).

British Standard 8118. (1999). Structural use of aluminium, part 1: Code of practice for design, amended 1999.

Buffa G, Fratini L, Pasta S, Shivpuri R. (2008). On the thermo-mechanical loads and the resultant residual stresses in friction stir processing operations. Manufacturing Technology. 57: 287–290.

Caldwell JB. (1965). Ultimate longitudinal strength. Trans. RINA. 107: 411-430.

Caseiro JF, Valente RAF, Andrade-Campos A, Yoon JW. (2013). On the elastoplastic buckling of Integrally Stiffened Panels (ISP) joined by Friction Stir Welding (FSW): Numerical simulation and Optimization algorithms. International Journal of Mechanical Sciences. 76: 49-59.

Chao YJ, Qi X, Tang W. (2003). Heat transfer in friction stir welding—experimental and numerical studies. ASME Journal of Manufacturing Science and Engineering. 125: 138–145.

Chao YJ, Qi X, Tang W. (2003). Heat transfer in friction stir welding—experimental and numerical studies. ASME Journal of Manufacturing Science and Engineering. 125: 138–145.

Chao YJ, Qi X. (1998). Thermal and thermo-mechanical modeling of friction stir welding of aluminum alloy 6061-T6. Journal of Materials Processing & Manufacturing Science. 7: 215–233.

Chao YJ, Qi X. (1999). Heat transfer and thermo-mechanical modeling of friction stir joining of AA6061-T6 plates. In: Proceedings of the First International Symposium on Friction Stir Welding, Thousand Oaks, CA, USA.

Chen CM, Kovacevic R. (2003). Finite element modeling of friction stir welding—thermal and thermomechanical analysis. International Journal of Machine Tools & Manufacture. 43: 1319-1326.

Collette, M.D. (2005). Strength and Reliability of Aluminium Stiffened Panels. PhD Thesis . Australia: University of Newcastle.

Dalle Donne C, Lima E, Wegener J, Pyzalla A, Buslaps T. (2001). Investigations on Residual Stresses in Friction Stir Welds. Proceeding of the 3rd International Symposium on FSW, TWI, Cambridge, Kobe, Japan.

Davis JR. (1993). Aluminum and aluminum alloys, ASM speciality handbook. ASM International.

Deng D, Murakawa H, Wei L. (2007b). Numerical Simulation of Welding Distortion in Large Structures. Computational Methods and Applications in Mechanical Engineering. 196: 4613-4627.

Deng D, Wei L, Murakawa H. (2007a). Determination of Welding Deformation in Fillet-Welded Joint by means of Numerical Simulation and Comparison with Experimental Measurements. Journal of Materials Processing Technology. 183: 219-225.

DNV. (2013). Rules for classification of High Speed, Light Craft and Naval Surface Craft. Det Norske Veritas.

Dow RS, Hugill RC, Clarke JD, Smith CS. (1981). Evaluation of ultimate ship hull strength. SNAME Extreme Loads Response Symposium. Arlington, Virginia. (pp.133-148).

Dow RS. (1991). Testing and analysis of a 1/3 scale welded steel frigate model. Advances in Marine Structures. 2: 749-773.

European Committee for Standardization. (1998). Eurocode 9: Design of aluminium structures Part 1 1:General rules — General rules and rules for buildings. European Committee for Standardization, ENV 1999-1-1.

Faulkner D, Adamchack JC, Snyder JG, Vetter MF. (1973). Synthesis of welded grillages to withstand compression and normal loads. Computers and Structures. 6:221-246.

Faulkner D. (1975). A review of effective plating for use in the analysis of stiffened plating in bending and compression. Journal of Ship Research, 19 (1): 1-17.

Feng Z, Wang XL, David SA, Sklad PS. (2007). Modelling of residual stresses and property distributions in friction stir welds of aluminium alloy 6061-T6. Science and Technology of Welding and Joining. 12: 348–56.

Friedman E. (1975). Thermomechanical analysis of the welding process using the finite element method. ASME Journal of Pressure Vessel Technology. *97* (3): 206-213.

Frigaard O, Grong O, Midling OT. (2001). A process model for friction stir welding of age hardening aluminum alloys. . Metallurgical and Materials Transactions A. 32: 1189–1200.

Gannon L, Liu Y, Pegg N, Smith M. (2010). Effect of welding sequence on residual stress and distortion in flat-bar stiffened plates. Marine Structures. 23:385–404.

Gannon L, Liu Y, Pegg N, Smith M. (2012). Effect of three-dimensional welding-induced residual stress and distortion fields on strength and behaviour of flat-bar stiffened panels. Ships and Offshore Structures. 8(5): 1-14.

Gannon L, Liu Y, Pegg N, Smith M. (2012). Effect of welding-induced residual stress and distortion on ship hull girder ultimate strength. Marine Structures. 28(1):25–49.

Gannon, L. (2011). Effect of welding residual stress and distortion on ship hull structural performance. PhD Thesis. Dalhousie University.

Gesto D, Pintos V, Vazquez J, Rasilla J, Barreras S. (2008). Proc. 7th International Symposium on 'Friction stir welding', Awaji Island, Japan.

Goldak J, Chakravarti A, Bibby M. (1984). A new finite element model for welding heat sources. Metallurgical Transactions B. 15B: 229-305.

Gordo JM, Guedes Soares C. (1993). Approximate load shortening curves for stiffened plates under uniaxial compression. Integrity Offshore Structures. 5: 189–211.

Gould J. (1998). Heat flow model for friction stir welding of aluminum alloys. Journal of Materials Processing & Manufacturing Science. 7: 185-94.

Guo JF, Chen HC, Sun CN, Bi G, Sun Z, Wei J. (2014). Friction stir welding of dissimilar materials between AA6061 and AA7075 Al alloys effects of process parameters. Materials & Design. 56: 185-192.

Hansen AM. (1996). Strength of midship sections. Marine Structures. 9: 471-494.

Hill HN, Clark JW, Brungraber AM. (1960). Design of Welded Aluminum Structures. Journal of the Structural Division, Proceedings of the ASCE. 86: 101- 124.

Hopperstad OS, Langseth M, Tryland T. (1999). Ultimate Strength of Aluminum Alloy Outstands in Compression: Experiments and Simplified Analysis. Thin-Walled Structures. 43: 279-295.

International Association of Classification Societies, IACS (2009). Common structural rules for double hull oil tankers.

JF Lincoln Arc Welding Foundation. (2000). The Procedure Handbook of Arc Welding. Fourteenth edition. 2000

Khandkar MZH, Khan JA, Reynolds AP, Sutton MA. (2006). Predicting residual thermal stresses in friction stir welded metals. Journal of Materials Processing Technology. 174: 195–203.

Kristensen Odd. (2001). Ultimate Capacity of Aluminium Plates under Multiple Loads, Considering HAZ Properties. PhD Thesis. Norwegian University of Science and Technology.

Kristensen OHH, Moan T. (1999). Ultimate strength of aluminium plates under biaxial loading. Proc. Of Fifth Inter. Conf. On Fast Sea Transportation, New York.

Krutz GW, Segerlind LJ. (1978). Finite element analysis of welded structures. Welding Journal. 57 (7): 211-216.

Kumaresan D, Asraff AK, Muthukumar R. (2011). Numerical Investigation on Heat Transfer and Residual Stress in a Butt Welded Plate. Journal of Pressure Vessel Technology. ASME. 133(4): 041206

Lombard H, Hattingh DG, Steuwer A, James MN. (2009). Effect of process parameters on the residual stresses in AA5083-H321 friction stir welds. Materials Science and Engineering: A. 501: 119- 124.

Mahoney MW, Rhodes CG, Flintoff JG, Spurling RA, Bingel WH. (1998). Properties of friction stir welded 7075-T651 aluminum. Metallurgical and Materials Transactions A. 29A:1955–1964.

Masubuchi K. (1980). Analysis of Welded Structures. Oxford, UK: Pergamon Press.

Matsuoka K, Tanaka Y, Fujita Y. (1998). Buckling strength of lightened aluminum hull structure. Proceedings, INALCO'98, International Conference on Aluminum Structural Design, April, Cambridge, UK. (pp.475–480).

Matusiak M, Larsen PK. (1998). Strength and Ductility of Welded Connections in Aluminium Alloys. Joints in Aluminium – INALCO. 299-310. Cambridge.

Matusiak M. (1999). Strength and Ductility of Welded Structures in Aluminium Alloys. PhD Thesis, Norwegian University of Science and Technology.

Mazzolani FM. (1995). Aluminium alloy structures. E & FN Spon.

Michaleris P, Feng Z, Campbell G. (1997). Evaluation of 2D and 3D FEA Models for Predicting Residual Stress and Distortion, Pressure Vessel and Piping Conference, ASME. 347: 91-102.

Midling JS, Kva LE, Dahl O. (2003). Proc. 1st International Symposium on "Friction stir welding". Proc. Thousand Oaks, CA, USA.

Mofflin DS, Dwight JB. (1984). Buckling of aluminum plates in compression. Thin-Walled Structures.399-427.

Mofflin, D.S. (1983). Plate Buckling in Steel and Aluminium. PhD Thesis, Trinity College, University of Cambridge.

Moraitis GA, Labeas GN. (2008). Residual stress and distortion calculation of laser beam welding for aluminum lap joints. Journal of Materials Processing Technology. 198: 260–269.

Muckle W. (1963). The Design of Aluminium Alloy Ships' Structures. London: Hutchinsons & Co.

Murphy A, McCune W, Quinn D, Price M. (2007). The characterisation of friction stir welding process effects on stiffened panel buckling performance. Thin-Walled Structures. 45:339–51.

Myers PS, Uyehara OA, Borman GL. (1967). Fundamentals of Heat Flow in Welding. Welding Research Council Bulletin, New York, NY, no. 123.

Nelson FG, Howell FM. (1952). The Strength and Ductility of Welds in Aluminum Alloy Plate. Welding Journal Research Supplement. September: 397-402.

Ohtsubo H, Sumi Y. (2000). Report of special task committee VI.2 - Ultimate hull girder strength. Procedings of the 14th International Ship and Offshore Structures Congress. Nagasaki: ISSC.

Paik J.K. (1993). Advanced idealized structural elements considering both ductile collapse and excessive tension deformation. Technical Report n. PNUNA-SE-30, Pusan National University, Department of Naval Architecture.

Paik JK, Andrieu C, Cojeen H.P. (2007). Mechanical collapse testing on aluminum stiffened plate structure for marine applications. 10th International Symposium on Practical Design of Ships and Other Floating Structures. Houston, Texas, USA.

Paik JK, Duran A. (2004). Ultimate Strength of Aluminum Plates and Stiffened Panels for Marine Applications. Marine Technology. 41: 108-121.

Paik JK, Thayamballi, A. (2003). Ultimate limit state design of steel-plated structures. London: John Wiley & Sons.

Paley Z, Hibbert PD. (1975). Computation of temperatures in actual weld designs. Welding Journal. 54: 385-392.

Pardo E, Weckman DC. (1989). Prediction of weld pool and reinforcement dimensions of GMA welds using a finite element model. Metallurgical Transactions B. 20B: 937-947.

Paulo RMF, Carlone P, Valente RAF, Teixeira-Dias F, Palazzo GS. (2014). Influence of friction stir welding residual stresses on the compressive strength of aluminium alloy plates. Thin-Walled Structures. 74:184-190.

Pavelic V, Tanbakuchi R, Uyehara OA, Myers PS. (1969). Welding Journal Research Supplement. 48: 295-230.

Playdon DK, Simmonds SH. (1984). Finite element modeling of buried structures. Conference of Research in Structures and Dynamics, Washington, D.C, USA.

Reynolds AP, Duvall F. (1999). Digital image correlation for determination of weld and base metal constitutive behavior. Welding Research Supplement. 78:355–360.

Riahi M, Nazari H. (2011). Analysis of transient temperature and residual thermal stresses in friction stir welding of aluminum alloy 6061-T6 via numerical simulation. The International Journal of Advanced Manufacturing Technology. 55: 143-152.

Rigo P, Sarghiuta R, Estefen S, Lehmann E, Otelea SC, Pasqualino I, Simonsen BC, Wan Z, Yao T. (2003). Sensitivity analysis on ultimate strength of aluminium stiffened panels. Marine Structures. 16: 437-468.

Rosenthal D. (1946). Trans. ASME. 68:849-865

Rutherford SE, Caldwell JB. (1990). Ultimate longitudinal strength of ships: A case study. Transactions, SNAME. 98: 441-471.

Sato Y, Kokawa H, Enomoto M, Jogan S. (1999). Microstructural Evolution of 6063 Aluminum during Friction Stir Welding. Metallurgical and Materials Transactions A. 30: 2429-2437.

Schmidt H, Hattel J, Wert J. (2004). An analytical model for the heat generation in friction stir Welding. Modelling and Simulation in Materials Science and Engineering. 12(1): 143-157.

Smith CS. (1977). Influence of local compressive failure on ultimate longitudinal strength of a ship's hull. Proceedings of the first PRADS, Tokyo. (pp. 73-79).

Song M, Kovacevic R. (2003). Thermal modeling of friction stir welding in a moving coordinate system and its validation. International Journal of Machine Tools and Manufacture. 43:605–615

SSC 460. (2011). Effect of welded properties on aluminum structures. Ship Structure Committee,

Steuwer A, Peel M, Withers PJ. (2006). Dissimilar friction stir welds in AA5083–AA6082: The effect of process parameters on residual stress. Materials Science and Engineering: A. 441: 187– 196.

Stowell EZ. (1948). A Unified Theory of Plastic Buckling of Columns and Plates. NACA Technical Note 1556.

Sutton MA, Reynolds AP, Wang DQ, Hubbard CR. (2002). A Study of Residual Stresses and Microstructure in 2024-T3 Aluminum Friction Stir Butt Welds. Journal of Engineering Materials and Technology. 124: 215–221.

Tang W, Guo X, McClure JC, Murr LE, Nunes A. (1998). Heat input and temperature distribution in friction stir welding. Journal of Materials Processing & Manufacturing Science. 7: 163–172.

Terasaki T, Akiyama T. (2003). Mechanical behaviour of joints in FSW: residual stress, inherent strain and heat input generated by friction stir welding. Welding in World. 47: 24-31.

Thomas WM, Nicholas ED, Needham JC, Murch MG, Temple-Smith P, Dawes CJ. (1991). Friction stir butt welding. International patent application no. PCT/ GB92102203 and Great Britain patent application no. 9125978.8.

Threadgill PL, Leonard AJ, Shercliff HR, Withers PJ. (2009). Friction stir welding of aluminum alloys. International Materials Review. 54:49–92

Tupper EC. (2004). Introduction to naval architecture (4th edition). Elsevier Ltd.

Ueda Y, Rashed MH. (1984). The idealized structural unit method and its application to deep girder structures. Computers & Structures. 18:277-293.

Ueda Y, Yao T. (1982). The plastic node method - a new method of plastic analysis. Computer Methods in Applied Mechanics and Engineering. 34:1089-1104.

Wang XL, Feng Z, David SA, Spooner S, Hubbard CR. (2000). Neutron diffraction study of residual stresses in friction stir welds. Proceeding of the 6th international conference on residual stresses, Oxford, UK. (pp. 1408–1414).

Webster PJ, Oosterkamp LD, Browne PA, Hughes DJ, Kang WP, Withers PJ, Vaughan GBM. (2001). Synchrotron X-ray residual strain scanning of a friction stir weld. Journal of Strain Analysis for Engineering Design. 36(1): 61-70.

Westby O. (1968). Temperature distribution in the workpiece by welding. Department of Metallurgy and Metals Working. Trondheim Norway: The Technical University.

Yao T, Nikolov PI. (1991). Progressive collapse analysis of a ship's hull under longitudinal bending. Journal of Society of Naval Architecture of Japan. 170: 449-461.

Yao T, Nikolov PI. (1992). Progressive collapse analysis of a ship's hull under longitudinal bending (2nd report). Journal of Society of Naval Architecture of Japan. 172: 437-446.

Yoon JW, Bray GH, Valente RAF, Childs TER. (2009). Buckling analysis for an integrally stiffened panel structure with a friction stir weld. Thin-Walled Structures. 47:1608–22.

Zha Y, Moan T. (2001). Ultimate strength of stiffened aluminium panels with predominantly torsional failure modes. Thin-Walled Structures. 39: 631- 648.

Zha Y, Moan T. (2003). Experimental and numerical collapse prediction of flat bar stiffeners in aluminum panels. Journal of Structural Engineering. 129: 160-168.

Zhang Z, Zhang HW. (2007). Material behaviors and mechanical features in friction stir welding process. The International Journal of Advanced Manufacturing Technology. 35:86–100.

Zhang Z, Zhang HW. (2008). A fully coupled thermo-mechanical model of friction stir welding. The International Journal of Advanced Manufacturing Technology. 37: 279–293.

Zhu XK, Chao YJ. (2002). Effects of temperature-dependent material properties on welding simulation. Computers and Structures. 80: 967–976

Zhu XK, Chao YJ. (2004). Numerical simulation of transient temperature and residual stresses in friction stir welding of 304L stainless steel. Journal of Material Processing Technology.146:263–72.

COPYRIGHT PERMISSIONS

A. Copyright permission for Chapter 4

March 23th 2016

Journal of Ships and Offshore Structures

I am preparing my Ph.D. thesis for submission to the Faculty of Graduate Studies at Dalhousie University , Halifax, Nova Scotia, Canada. I am seeking your permission to include a manuscript version of the following paper as a chapter in the thesis:

[Vahid Farajkhah, Yi Liu and Liam Gannon,
"Finite element study of 3D simulated welding effect in aluminium plates", Ships and Offshore Structures. 2016, DOI:10.1080/17445302.2015.1123865.]

Canadian graduate theses are reproduced by the Library and Archives of Canada (formerly National Library of Canada) through a non-exclusive, world-wide license to reproduce, loan, distributor or sell these. I am also seeking your permission for the material described above to be reproduced and distributed by the LAX (NLC). Further details about the LAC (NLC) thesis program are available on the LAC (NLC) website (www.nlc-bnc.ca) Full publication details and a copy of this permission letter will be included in the thesis.

Yours Sincerely,

Vahid Farajkhah

Our Ref: LA/TSOS/P7347

05 May 2016

Dear Vahid Farajkhah,

Material requested: Vahid Farajkhah, Yi Liu & Liam Gannon (2016): Finite element study of 3D simulated welding effect in aluminium plates, Ships and Offshore Structures

Thank you for your correspondence requesting permission to reproduce the above mentioned material from our Journal in your printed thesis entitled 'EFFECT OF 3D SIMULATED WELDING INDUCED HAZ, RESIDUAL STRESS AND DISTORTION FIELDS ON ULTIMATE STRENGTH OF ALUMINUM STIFFENED PLATES' and to be posted in the university's repository - Dalhousie University and also to be hosted online by www.nlc-bnc.ca

We will be pleased to grant permission on the sole condition that you acknowledge the original source of publication and insert a reference to the article on the Journals website: http://www.tandfonline.com

This is the authors accepted manuscript of an article published as the version of record in Ships and Offshore Structures © 25 Jan 2016 http://dx.doi.org/10.1080/17445302.2015.1123865

This permission does not cover any third party copyrighted work which may appear in the material requested.

Please note that this license does not allow you to post our content on any third party websites or repositories.

Thank you for your interest in our Journal.

Yours sincerely

Lee-Ann

Lee-Ann Anderson – Permissions & Licensing Administrator, Journals

Routledge, Taylor & Francis Group

3 Park Square, Milton Park, Abingdon, Oxon, OX14 4RN, UK.

Tel: +44 (0)20 7017 7932

Fax:+44 (0)20 7017 6336

Web: www.tandfonline.com

e-mail: lee-ann.anderson@tandf.co.uk

A. Copyright permission for Chapter 4

B. Copyright permission for Chapter 8

March 23th 2016

Journal of Ocean Engineering

I am preparing my Ph.D. thesis for submission to the Faculty of Graduate Studies at Dalhousie University, Halifax, Nova Scotia, Canada. I am seeking your permission to include a manuscript version of the following paper as a chapter in the thesis:

[Vahid Farajkhah and Yi Liu, “Effect of fabrication methods on the ultimate strength of aluminum hull girders”, Ocean Engineering 114 (2016) 269–279.]

Canadian graduate theses are reproduced by the Library and Archives of Canada (formerly National Library of Canada) through a non-exclusive, world-wide license to reproduce, loan, distributor or sell these. I am also seeking your permission for the material described above to be reproduced and distributed by the LAX (NLC). Further details about the LAC (NLC) thesis program are available on the LAC (NLC) website (www.nlc-bnc.ca) Full publication details and a copy of this permission letter will be included in the thesis.

Yours Sincerely,

Vahid Farajkhah

ELSEVIER LICENSE
TERMS AND CONDITIONS

May 05, 2016

This is a License Agreement between Vahid Farajkhah ("You") and Elsevier ("Elsevier") provided by Copyright Clearance Center ("CCC"). The license consists of your order details, the terms and conditions provided by Elsevier, and the payment terms and conditions.

All payments must be made in full to CCC. For payment instructions, please see information listed at the bottom of this form.

Supplier	Elsevier Limited The Boulevard,Langford Lane Kidlington,Oxford,OX5 1GB,UK
Registered Company Number	1982084
Customer name	Vahid Farajkhah
Customer address	1270 Hollis Street Halifax, NS b3j1t6
License number	3837651180493
License date	Mar 28, 2016
Licensed content publisher	Elsevier
Licensed content publication	Ocean Engineering
Licensed content title	Effect of fabrication methods on the ultimate strength of aluminum hull girders
Licensed content author	Vahid Farajkhah,Yi Liu
Licensed content date	1 March 2016
Licensed content volume number	114
Licensed content issue number	n/a
Number of pages	11
Start Page	269

End Page	279
Type of Use	reuse in a thesis/dissertation
Portion	full article
Format	both print and electronic
Are you the author of this Elsevier article?	Yes
Will you be translating?	No
Title of your thesis/dissertation	EFFECT OF 3D SIMULATED WELDING INDUCED HAZ, RESIDUAL STRESS AND DISTORTION FIELDS ON ULTIMATE STRENGTH OF ALUMINUM STIFFENED PLATES
Expected completion date	Mar 2016
Estimated size (number of pages)	247
Elsevier VAT number	GB 494 6272 12
Permissions price	0.00 USD
VAT/Local Sales Tax	0.00 USD / 0.00 GBP
Total	0.00 USD

Terms and Conditions

INTRODUCTION

1. The publisher for this copyrighted material is Elsevier. By clicking "accept" in connection with completing this licensing transaction, you agree that the following terms and conditions apply to this transaction (along with the Billing and Payment terms and

conditions established by Copyright Clearance Center, Inc. ("CCC"), at the time that you opened your Rightslink account and that are available at any time at http://myaccount.copyright.com).

GENERAL TERMS

2. Elsevier hereby grants you permission to reproduce the aforementioned material subject to the terms and conditions indicated.

3. Acknowledgement: If any part of the material to be used (for example, figures) has appeared in our publication with credit or acknowledgement to another source, permission must also be sought from that source. If such permission is not obtained then that material may not be included in your publication/copies. Suitable acknowledgement to the source must be made, either as a footnote or in a reference list at the end of your publication, as follows:

"Reprinted from Publication title, Vol /edition number, Author(s), Title of article / title of chapter, Pages No., Copyright (Year), with permission from Elsevier [OR APPLICABLE SOCIETY COPYRIGHT OWNER]." Also Lancet special credit - "Reprinted from The Lancet, Vol. number, Author(s), Title of article, Pages No., Copyright (Year), with permission from Elsevier."

4. Reproduction of this material is confined to the purpose and/or media for which permission is hereby given.

5. Altering/Modifying Material: Not Permitted. However figures and illustrations may be altered/adapted minimally to serve your work. Any other abbreviations, additions, deletions and/or any other alterations shall be made only with prior written authorization of Elsevier Ltd. (Please contact Elsevier at permissions@elsevier.com)

6. If the permission fee for the requested use of our material is waived in this instance, please be advised that your future requests for Elsevier materials may attract a fee.

7. Reservation of Rights: Publisher reserves all rights not specifically granted in the combination of (i) the license details provided by you and accepted in the course of this licensing transaction, (ii) these terms and conditions and (iii) CCC's Billing and Payment terms and conditions.

8. License Contingent Upon Payment: While you may exercise the rights licensed immediately upon issuance of the license at the end of the licensing process for the transaction, provided that you have disclosed complete and accurate details of your proposed use, no license is finally effective unless and until full payment is received from you (either by publisher or by CCC) as provided in CCC's Billing and Payment terms and conditions. If full payment is not received on a timely basis, then any license preliminarily granted shall be deemed automatically revoked and shall be void as if never granted. Further, in the event that you breach any of these terms and conditions or any of CCC's Billing and Payment terms and conditions, the license is automatically revoked and shall be void as if never granted. Use of materials as described in a revoked license, as well as any use of the materials beyond the scope of an unrevoked license, may constitute copyright infringement and publisher reserves the right to take any and all action to protect its copyright in the materials.

9. Warranties: Publisher makes no representations or warranties with respect to the licensed material.

10. Indemnity: You hereby indemnify and agree to hold harmless publisher and CCC, and their respective officers, directors, employees and agents, from and against any and all

claims arising out of your use of the licensed material other than as specifically authorized pursuant to this license.
11. No Transfer of License: This license is personal to you and may not be sublicensed, assigned, or transferred by you to any other person without publisher's written permission.
12. No Amendment Except in Writing: This license may not be amended except in a writing signed by both parties (or, in the case of publisher, by CCC on publisher's behalf).
13. Objection to Contrary Terms: Publisher hereby objects to any terms contained in any purchase order, acknowledgment, check endorsement or other writing prepared by you, which terms are inconsistent with these terms and conditions or CCC's Billing and Payment terms and conditions. These terms and conditions, together with CCC's Billing and Payment terms and conditions (which are incorporated herein), comprise the entire agreement between you and publisher (and CCC) concerning this licensing transaction. In the event of any conflict between your obligations established by these terms and conditions and those established by CCC's Billing and Payment terms and conditions, these terms and conditions shall control.
14. Revocation: Elsevier or Copyright Clearance Center may deny the permissions described in this License at their sole discretion, for any reason or no reason, with a full refund payable to you. Notice of such denial will be made using the contact information provided by you. Failure to receive such notice will not alter or invalidate the denial. In no event will Elsevier or Copyright Clearance Center be responsible or liable for any costs, expenses or damage incurred by you as a result of a denial of your permission request, other than a refund of the amount(s) paid by you to Elsevier and/or Copyright Clearance Center for denied permissions.

LIMITED LICENSE

The following terms and conditions apply only to specific license types:
15. **Translation**: This permission is granted for non-exclusive world **English** rights only unless your license was granted for translation rights. If you licensed translation rights you may only translate this content into the languages you requested. A professional translator must perform all translations and reproduce the content word for word preserving the integrity of the article.
16. **Posting licensed content on any Website**: The following terms and conditions apply as follows: Licensing material from an Elsevier journal: All content posted to the web site must maintain the copyright information line on the bottom of each image; A hyper-text must be included to the Homepage of the journal from which you are licensing athttp://www.sciencedirect.com/science/journal/xxxxx or the Elsevier homepage for books athttp://www.elsevier.com; Central Storage: This license does not include permission for a scanned version of the material to be stored in a central repository such as that provided by Heron/XanEdu.
Licensing material from an Elsevier book: A hyper-text link must be included to the Elsevier homepage at http://www.elsevier.com . All content posted to the web site must maintain the copyright information line on the bottom of each image.

Posting licensed content on Electronic reserve: In addition to the above the following clauses are applicable: The web site must be password-protected and made available only to bona fide students registered on a relevant course. This permission is granted for 1 year only. You may obtain a new license for future website posting.

17. **For journal authors:** the following clauses are applicable in addition to the above:
Preprints:
A preprint is an author's own write-up of research results and analysis, it has not been peer-reviewed, nor has it had any other value added to it by a publisher (such as formatting, copyright, technical enhancement etc.).
Authors can share their preprints anywhere at any time. Preprints should not be added to or enhanced in any way in order to appear more like, or to substitute for, the final versions of articles however authors can update their preprints on arXiv or RePEc with their Accepted Author Manuscript (see below).
If accepted for publication, we encourage authors to link from the preprint to their formal publication via its DOI. Millions of researchers have access to the formal publications on ScienceDirect, and so links will help users to find, access, cite and use the best available version. Please note that Cell Press, The Lancet and some society-owned have different preprint policies. Information on these policies is available on the journal homepage.
Accepted Author Manuscripts: An accepted author manuscript is the manuscript of an article that has been accepted for publication and which typically includes author-incorporated changes suggested during submission, peer review and editor-author communications.
Authors can share their accepted author manuscript:

- – immediately
    - via their non-commercial person homepage or blog
    - by updating a preprint in arXiv or RePEc with the accepted manuscript
    - via their research institute or institutional repository for internal institutional uses or as part of an invitation-only research collaboration work-group
    - directly by providing copies to their students or to research collaborators for their personal use
    - for private scholarly sharing as part of an invitation-only work group on commercial sites with which Elsevier has an agreement
- – after the embargo period
    - via non-commercial hosting platforms such as their institutional repository
    - via commercial sites with which Elsevier has an agreement

In all cases accepted manuscripts should:

- – link to the formal publication via its DOI
- – bear a CC-BY-NC-ND license - this is easy to do
- – if aggregated with other manuscripts, for example in a repository or other site, be shared in alignment with our hosting policy not be added to or enhanced in any way to appear more like, or to substitute for, the published journal article.

Published journal article (JPA): A published journal article (PJA) is the definitive final record of published research that appears or will appear in the journal and embodies all value-adding publishing activities including peer review co-ordination, copy-editing, formatting, (if relevant) pagination and online enrichment.

Policies for sharing publishing journal articles differ for subscription and gold open access articles:

Subscription Articles: If you are an author, please share a link to your article rather than the full-text. Millions of researchers have access to the formal publications on ScienceDirect, and so links will help your users to find, access, cite, and use the best available version.

Theses and dissertations which contain embedded PJAs as part of the formal submission can be posted publicly by the awarding institution with DOI links back to the formal publications on ScienceDirect.

If you are affiliated with a library that subscribes to ScienceDirect you have additional private sharing rights for others' research accessed under that agreement. This includes use for classroom teaching and internal training at the institution (including use in course packs and courseware programs), and inclusion of the article for grant funding purposes.

Gold Open Access Articles: May be shared according to the author-selected end-user license and should contain a CrossMark logo, the end user license, and a DOI link to the formal publication on ScienceDirect.

Please refer to Elsevier's posting policy for further information.

18. **For book authors** the following clauses are applicable in addition to the above: Authors are permitted to place a brief summary of their work online only. You are not allowed to download and post the published electronic version of your chapter, nor may you scan the printed edition to create an electronic version. **Posting to a repository:** Authors are permitted to post a summary of their chapter only in their institution's repository.

19. **Thesis/Dissertation**: If your license is for use in a thesis/dissertation your thesis may be submitted to your institution in either print or electronic form. Should your thesis be published commercially, please reapply for permission. These requirements include permission for the Library and Archives of Canada to supply single copies, on demand, of the complete thesis and include permission for Proquest/UMI to supply single copies, on demand, of the complete thesis. Should your thesis be published commercially, please reapply for permission. Theses and dissertations which contain embedded PJAs as part of the formal submission can be posted publicly by the awarding institution with DOI links back to the formal publications on ScienceDirect.

Elsevier Open Access Terms and Conditions

You can publish open access with Elsevier in hundreds of open access journals or in nearly 2000 established subscription journals that support open access publishing. Permitted third party re-use of these open access articles is defined by the author's choice of Creative Commons user license. See our open access license policy for more information.

Terms & Conditions applicable to all Open Access articles published with Elsevier: Any reuse of the article must not represent the author as endorsing the adaptation of the article nor should the article be modified in such a way as to damage the author's honour or reputation. If any changes have been made, such changes must be clearly indicated. The author(s) must be appropriately credited and we ask that you include the end user license and a DOI link to the formal publication on ScienceDirect.

If any part of the material to be used (for example, figures) has appeared in our publication with credit or acknowledgement to another source it is the responsibility of the user to ensure their reuse complies with the terms and conditions determined by the rights holder.

Additional Terms & Conditions applicable to each Creative Commons user license:

CC BY: The CC-BY license allows users to copy, to create extracts, abstracts and new works from the Article, to alter and revise the Article and to make commercial use of the Article (including reuse and/or resale of the Article by commercial entities), provided the user gives appropriate credit (with a link to the formal publication through the relevant DOI), provides a link to the license, indicates if changes were made and the licensor is not represented as endorsing the use made of the work. The full details of the license are available at http://creativecommons.org/licenses/by/4.0.

CC BY NC SA: The CC BY-NC-SA license allows users to copy, to create extracts, abstracts and new works from the Article, to alter and revise the Article, provided this is not done for commercial purposes, and that the user gives appropriate credit (with a link to the formal publication through the relevant DOI), provides a link to the license, indicates if changes were made and the licensor is not represented as endorsing the use made of the work. Further, any new works must be made available on the same conditions. The full details of the license are available at http://creativecommons.org/licenses/by-nc-sa/4.0.

CC BY NC ND: The CC BY-NC-ND license allows users to copy and distribute the Article, provided this is not done for commercial purposes and further does not permit distribution of the Article if it is changed or edited in any way, and provided the user gives appropriate credit (with a link to the formal publication through the relevant DOI), provides a link to the license, and that the licensor is not represented as endorsing the use made of the work. The full details of the license are available at http://creativecommons.org/licenses/by-nc-nd/4.0. Any commercial reuse of Open Access articles published with a CC BY NC SA or CC BY NC ND license requires permission from Elsevier and will be subject to a fee.

Commercial reuse includes:

- – Associating advertising with the full text of the Article
- – Charging fees for document delivery or access
- – Article aggregation
- – Systematic distribution via e-mail lists or share buttons

Posting or linking by commercial companies for use by customers of those companies.

20. **Other Conditions**:

v1.8